Universidad de La Laguna

Escuela de Doctorado y Estudios de Posgrado

TÍTULO DE LA TESIS DOCTORAL

Revealing the outer Galactic disc with Gaia DR2

AUTOR/A

Zofia	Chrobakova	None

DIRECTOR/A

Martín	López	Corredoira

CODIRECTOR/A

DEPARTAMENTO O INSTITUTO UNIVERSITARIO

FECHA DE LECTURA

06/09/21

UNIVERSIDAD Ð LA LAGUNA
Departamento de Astrofísica

Revealing the outer Galactic disc with Gaia DR2

Memoria que presenta
Žofia Chrobáková
para optar al grado de
Doctor en Ciencias Físicas.

INSTITUTO Ð ASTROFISICA Ð CANARIAS
junio de 2021

Examination date: September, 2021
Thesis supervisor: Dr. Martín López-Corredoira

ISBN: xx-xxx-xxxx-x
Depósito legal: TF-xxxx/2021

Venované mojej babke a celej mojej rodine,
ktorí na mňa stále myslia a nikdy sa za mňa neprestali modliť. ('To my
grandmother and all my family,
who thought of me always and kept me in their prayers.')

Acknowledgements

I am most grateful to my supervisor Martín López-Corredoira, whose guidance during the course of this thesis was truly invaluable. I feel blessed to have had the opportunity to learn from your expertise and gain experience by your side. Thank you for your counsel, patience and hospitality at the institute.

I would also like to thank Francesco Sylos Labini and Haifeng Wang for many constructive discussions and advice, which helped to improve this work significantly. Moreover, I am thankful to Francesco for the opportunity to work at the Instituto Dei Sistemi Complessi in Rome and for his mentorship and helpfulness during this visit.

I especially thank Roman Nagy, for his professional advice as well as unequalled friendship. Furthermore, I would like to extend my thanks to my friends in Slovakia and abroad, my boyfriend Eduardo and my family for always standing by me and supporting me. It is a privilege to have you all in my life.

Ďakujem mojim rodičom, bratom, babke a krstnému za podporu počas celého môjho štúdia, bez ktorej by sa to nedalo zvládnuť. Ďakujem za to, že mi pomáhate a myslíte na mňa, aj keď som tak ďaleko od domova. Som rada, že som vám mohla venovať túto prácu. ('I thank my parents, brothers, grandmother and godfather for their support during my studies, without which I could not have succeeded. You all helped me and thought of me even though I was so far from home. It gives me joy to be able to dedicate this work to you.')

Resumen

El disco estelar más externo de la Vía Láctea, a distancias desde su centro superiores a 15 kpc, es una de las regiones más desconocidas de nuestra Galaxia. Como las poblaciones estelares del disco externo tienen densidades bajas y las medidas de su distancia tienen errores elevados, es difícil modelar la distribución de tales.

Esta tesis pretende explorar esa parte externa de la Galaxia en tres temas conectados entre sí. En primer lugar, investigamos la distribución de la densidad del disco externo y exploramos sus características estructurales. A continuación, estudiamos la curva de rotación del disco exterior y las desviaciones del equilibrio. El último objetivo es analizar la precesión del alabeo del disco y su implicación en el origen del mismo.

Con tal fin, desarrollamos un método de deconvolución estadística que nos permite recuperar las cuentas de estrellas hasta una distancia de 20 kpc desde el centro. Además, aplicamos la ecuación de Jeans para derivar la curva de rotación a partir de los datos cinemáticos obtenidos con el mismo método. A lo largo de la tesis, utilizamos los datos de Gaia-DR2, que proporcionan la más completa información astrométrica de la Vía Láctea hasta la fecha.

La distribución de la densidad obtenida revela que el alabeo del disco está deformado asimétricamente, siendo su amplitud en el hemisferio Galáctico norte mayor que la del sur en un 25%. Además la amplitud del alabeo es menor de lo que se pensaba y muestra una fuerte dependencia con la edad de la población estelar estudiada. Cuando comparamos nuestro resultado con el de las Cefeidas, encontramos una amplitud de alabeo 2–3 veces menor.

El análisis de las curvas de rotación del disco exterior revela que tiene poca dependencia del radio y la distancia al plano de la Galaxia. Al contrastar las curvas con modelos que incluyen un halo de materia oscura o una dinámica newtoniana modificada (MOND), encontramos que ambos las reproducen. Al realizar simulaciones de N-cuerpos de sistemas galácticos fuera de equilibrio, en-

contramos que la ecuación de Jeans, utilizada para calcular la curva de rotación, sobrestima la velocidad de rotación a distancias superiores a 20 kpc, por lo que el no-equilibrio no afecta significativamente a nuestras curvas.

El resultado final es el análisis de la precesión del alabeo. Aplicamos el modelo de alabeo que derivamos utilizando el conjunto de las poblaciones estelares observados y encontramos que los datos son compatibles con un modelo de precesión lenta de varios Gyr o incluso sin precesión, al contrario de lo que hallaron otros trabajos, que midieron una precesión significativamente más rápida, con un periodo de 600 Myr, al haber asumido erróneamente que la amplitud del alabeo no depende de la edad de la población estelar.

Estos resultados apoyan la teoría de que el alabeo es un rasgo de larga duración producido por un mecanismo no gravitacional. También concluimos que, debido al desequilibrio, la ecuación de Jeans puede producir resultados poco fiables a altas distancias Galactocéntricas. Esta tesis aporta así ciertos avances en la exploración del disco galáctico exterior y sienta las bases para futuros trabajos que se llevarán a cabo con las próximas liberaciones de datos de Gaia.

Abstract

The outer stellar disc of the Milky Way at Galactocentric distances greater than 15 kpc is one of the Galaxy's most unknown regions. As stellar populations in the external disc have low densities and their measured distances have large errors, it is difficult to constrain their distribution.

This thesis aims to explore the outer part of the Galaxy on three fronts. First, we investigate the density distribution of the outer disc and explore its structural features. Next, we study the outer disc's rotation curve and deviations from equilibrium. Our last goal is to analyse the precession of the warp and its implications for the warp's origin.

To this end, we develop a statistical deconvolution method that enables us to recover star counts up to Galactocentric distance 20 kpc. We also apply the Jeans equation to derive rotation curve from kinematic data obtained with the same method. Throughout the thesis we use the second *Gaia* data release, which provides the most advanced astrometric information of the Milky Way to date.

The obtained density distribution reveals that the disc is asymmetrically warped, the northern Galactic hemisphere amplitude being larger than the southern one by ∼25%. Moreover, the warp amplitude is lower than previously thought and exhibits a strong dependence on the age of the stellar population. When we compare our result with that of the Cepheids, we find a 2–3 times lower warp amplitude.

Analysis of rotation curves of the outer disc reveals that it has little dependence on either Galactic radius and height. Upon fitting the curves with models including either a dark matter halo or Modified Newtonian dynamics (MOND), we find that both approaches provide satisfactory fits. By performing N-body simulations of mock galactic systems in disequilibrium, we discover that the Jeans equation, used to calculate the rotation curve, notably overestimates rotational velocity at distances greater than 20 kpc; non-equilibrium does not,

therefore, significantly affect our curves.

Our final result is an analysis of warp precession. We apply the warp model that we derived using the whole stellar population and find that the data are compatible with a model with slow precession of several Gyr or a non-precessing model as well, contrary to other works that measured a faster precession with a period of ∼600 Myr, not taking into account warp dependence on the age of the population.

These results support the theory that warp is a long-lived feature triggered by a non-gravitational mechanism. We also conclude that owing to disequilibrium, the Jeans equation may produce unreliable results at large Galactocentric distances. This thesis contributes to exploration of the outer Galactic disc and lays a foundation for future work to be carried out with forthcoming *Gaia* data releases.

Contents

1

Introduction

From ancient times to the modern day, astronomy has always played an important role in all cultures and eras. Questions about the nature of the infinite cosmos and our place in it have intrigued great minds for millennia. Exploration of the Milky Way has always been in the spotlight of these endeavours to understand the Universe, as our home Galaxy represents an ideal laboratory to test our hypotheses about astrophysical phenomena.

Our knowledge of the Milky Way has evolved spectacularly over the centuries and is currently relatively extensive. We have a good understanding of various components of our Galaxy, our position in it and in the Local Group. However, there are still many questions that remain unanswered. The full picture of how our Galaxy was formed, how it will evolve and how is it connected to other galaxies is a complicated puzzle, whose pieces are being put together by a great group effort of scientists all around the world.

We now know that the Milky Way is a spiral galaxy consisting of a bulge and/or a bar, a disc with several spiral arms and a stellar halo (see Figure 1.1), extending out to a radius of ∼30 kpc and containing about 100 billion stars. It is also believed that the Milky Way has a dark matter halo with radius of some 290 kpc (Deason et al. 2020). Our position in the Milky Way is ∼8.3 kpc from the Galactic centre (Gillessen et al. 2017).

In this section, we briefly review research on the Milky Way throughout history, which will lead us to open questions and build the motivation for the thesis.

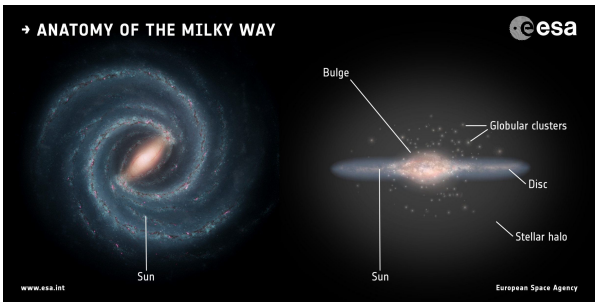

FIGURE 1.1— An artist's impression of the morphology of the Milky Way. Credit: Left: NASA/JPL-Caltech. Right: ESA. Layout: ESA/ATG medialab.

1.1 A history of Milky Way research

Research on the Milky Way dates back to 1610 when Galileo Galilei observed the Galaxy as a group of individual stars for the first time. His pioneering observations with the newly invented telescope laid the foundations for our understanding of the contents of the Galaxy.

One and a half century later in 1750, Thomas Wright proposed that the stars are bound together as a part of a larger body. In his book *An Original Theory or New Hypothesis of the Universe* he described the appearance of the Milky Way as 'an optical effect due to our immersion in what locally approximates to a flat layer of stars.' In the same publication he suggested for the first time that there are other galaxies than our own. Although only 118 copies of his book were printed, his work eventually reached Immanuel Kant, who became persuaded by Wright's arguments and further developed his ideas. In his *Allgemeine Naturgeschichte un Theorie des Himmels* ('Universal Natural History and Theory of the Heavens'), which he published in 1755, he coined the famous term 'island universe' to describe galaxies, including our own, as individual systems embedded in empty space. His ideas influenced generations of astronomers, such as Charles Messier, who compiled a catalogue of 'nebulous objects', some of which we now know are galaxies, for the purpose of making comet observing easier. Another major breakthrough was made by William and Caroline Herschel, who drew the first quantitative chart of the Milky Way based

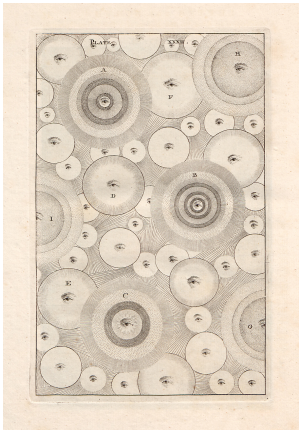

FIGURE 1.2— Illustration from Thomas Wright's *An Original Theory or New Hypothesis of the Universe* (Wright 1750).

on number of stars that they counted. They found that the Galaxy has a flat, symmetrical shape, and that the Sun lies close to its centre. They also created a catalogue of 'spiral nebulae', implying they could resolve the spiral nature of some galaxies. Interestingly, a similar result concerning the structure of the Galaxy was obtained by Jacobus Kapteyn in the early 20th century. He used photographic plates from all over the world and studied the apparent brightness of the stars, as well as their proper motions and spectra. He also found that the Milky Way has a flattened shape and placed Sun close to its centre. The common flaw of both these results is that they did not account for extinction caused by interstellar dust, whose existence was not firmly established until 1930 (Trumpler 1930).

At the beginning of the 20th century, the evidence supporting the 'island universes' theory was piling up; however, it was still a rather speculative notion generating vivid discussion. Discord among the community culminated in the famous 'Great Debate' between Harlow Shapley and Heber Curtis in 1920 (Shapley & Curtis 1921), in which Shapley argued that the Milky Way repre-

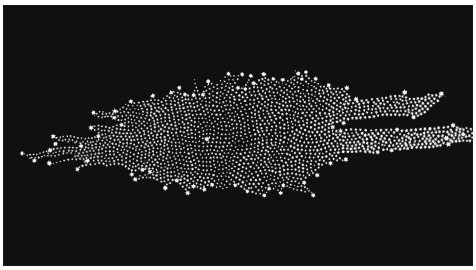

FIGURE 1.3— William Herschel's map of the Milky Way (Herschel 1785).

sents the entire Universe, while Curtis opposed that idea. Now we know that Curtis was the winner of the debate in his defence of the hypothesis that Andromeda and other such nebulae are separate galaxies, although Shapley, in contradiction to Curtis, correctly affirmed and demonstrated that the Sun was not at the centre of the Milky Way.

The main evidence that effectively resolved the debate was provided by Edwin Hubble, who measured the distances of Cepheids in several galaxies and found them to lie well beyond the Milky Way (Hubble 1926). Thus, he confirmed that the Universe comprises a multitude of galaxies and launched a new era of astrophysical research. He then took on the task of classifying the galaxies and found four main types—elliptical (E0–E7), spiral with a central bulge (Sa–Sc), spiral with a central bar (SBa–SBc) and lenticular (S0). This classification formed the basis of the tuning fork diagram (see Figure 1.4), which was originally proposed by James Jeans (Jeans 1928; Way 2013). Hubble also contributed to cosmology with the Hubble-Lemaître law (Lemaître had published it two years earlier).

When it became clear that the Milky Way is an individual galaxy, efforts were made to understand its kinematics and dynamics. For instance, Bertil Lindblad successfully explained star streaming—the motion of stars in only two directions in space, a phenomenon first noticed by Kapteyn. Lindblad correctly deduced that Galaxy is rotating and calculated the circular rotation velocity of the Solar neighbourhood to be 200–300 km/s (Lindblad 1925). That was soon confirmed by Jan Oort (Oort 1927), who characterized Galactic rotation with a set of constants named after him.

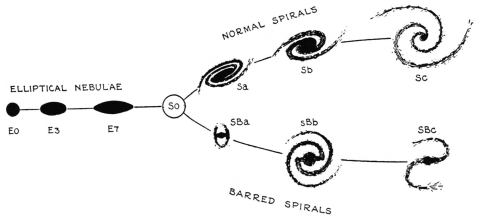

FIGURE 1.4— Hubble's classification of galaxies (Hubble (1936), figure taken from Dick (2020)).

The twentieth century also marked the beginning of radio astronomy. Radio emission from the Milky Way was discovered accidentally by Karl Jansky while he was studying sources that might interfere with telephonic communication (Jansky 1933). As Jansky was not a professional astronomer, his discoveries were overlooked for some time and developed mostly by amateur astronomers. The first professional to realize the importance of radio astronomy was Jan Oort. He launched a project with his collaborators and detected 21-cm hydrogen radio waves, which led to a number of discoveries. As the hydrogen emission line is unaffected by extinction, it is useful for mapping the Milky Way at vast distances. For instance, Oort and coworkers confirmed the spiral structure of the Milky Way, measured Galaxy's rotation period, and were the first to investigate the Galactic centre (e.g., Oort 1955). Radio astronomy remains an important branch of astrophysics and is used to study a variety of topics.

Efforts to characterize the morphology of the Milky Way also led to the discovery of spiral arms. In 1951, William Morgan showed that the Milky Way has a spiral pattern and discovered the Orion and Perseus arms (Morgan et al. 1952). Shortly after, the Sagittarius arm was also discovered by Bok et al. (1953). To explain the mechanism that creates spiral arms, Lin & Shu (1964) proposed a density wave theory, suggesting that a standing wave pattern rotates around the Galactic centre, triggering the formation of long-lived spiral arms. Another major theory was put forward by Toomre (1981), who proposed the hypothesis that spiral arms are a superposition of many unstable waves occurring via swing amplification, and are thus transient and recurrent. These and other theories are still being explored as the origin of the spiral arms is still not understood.

Furthermore, technological advances made it possible to extend observations

to the near-infrared spectral range. The Two-Micron Sky Survey (Neugebauer & Leighton 1969, TMASS) was a pioneering project, that detected ∼5700 sources dominated by red, cool stars. At the time, it provided a unique opportunity to study such stars in great detail, since in optical spectrum the sample was limited and biased owing to extinction. It also discovered new types of stars, such as infrared carbon stars. Another important contribution to near-infrared surveys developed during the twentieth century was the Two Micron Galactic Survey (Garzón et al. 1993, TMGS), developed in Tenerife, that explored only the Galactic plane in the K-band, making significant finds concerning the morphology of the Galaxy. In the southern hemisphere, the near-infrared sky was surveyed by the Deep Near Infrared Survey of the Southern Sky (Epchtein et al. 1994, DENIS), which contributed significantly to Milky Way research by discovering the distribution of red giants in the inner disc, detecting new dwarf stars, mapping extinction (Habing & Epchtein 1998). Infrared astronomy is now a well-developed field of astrophysics, producing important observations in the Milky Way and beyond.

Improved observational opportunities also led to the revitalization of star counts. Machines constructed for the automated measurement of photographic plates (e.g. GALAXY at the Royal Observatory, Edinburgh) made it much easier and faster to extract information from Schmidt plates, thus facilitating star count analysis. Among the surveys aimed at Galactic structure analysis were Reid & Gilmore (1982); Weistrop (1972); Infante (1986), and many others. Bahcall & Soneira (1980) on the other hand developed a model of the Galaxy, from which they estimated density distributions, which they compared with data. This approach became very popular and is still being used with various Galactic models.

Today, we rely mostly on large surveys that gather vast amounts of data that help unravel mysteries about the Galaxy.

1.2 Milky Way surveys

One natural constraint on astrophysics is that we cannot make direct experiments; therefore, the only way to collect information is via observations. Hence, our knowledge of the Universe is entirely dependent on our ability to construct telescopes and carry out surveys to gather as much information as possible. In this section, we review some of the most important surveys to explore the Milky Way.

1.2.1 Hipparcos

The ESA mission *Hipparcos* operated from 1989 to 1993 and was a landmark in Milky Way research. Ground-based astrometry measurement had reached its accuracy limit owing to effects of the Earth's atmosphere (refraction, extinction, and turbulence) and instrumental flexure, and *Hipparcos* was the first space-based instrument dedicated to astrometry. *Hipparcos* observations are compiled in an extensive online catalogue (ESA 1997), containing over 10^5 stars with an astrometric precision of 0.001 arcseconds, which represented a major advance over catalogues of ground-based observations and parallaxes. Apart from the main catalogue, an additional catalogue (*Tycho*) was created using satellite's auxiliary star mapper. This catalogue contains $\sim 10^6$ stars, although with reduced accuracy compared to the main catalogue. The final catalogue *Tycho-2* (Høg et al. 2000) contains data for ∼2.5 million stars and is 99% complete down to magnitude 11, thanks to more advanced reduction techniques.

The importance of this mission is borne out by the scientific harvest of thousands of papers published using *Hipparcos* data. For instance, *Hipparcos* data provides an accurate reference frame, which was used for a re-reduction of historical measurements (Reid 1990), as well as a common reference system for present-day surveys, such as the Sloan Digital Sky Survey, the Two Micron All-Sky Survey, and others. The significant improvement in the accuracy of measurements of parallax led to improved constraints on fundamental stellar parameters, which deepened our understanding of stellar evolution and the internal structure of virtually all types of stars (e.g., Hog & Petersen 1997; Söderhjelm 1999). Accurate distances, combined with improved measurements of proper motions, also led to a better understanding of the kinematics and dynamics of the solar neighbourhood (e.g., Smart et al. 1998; Dehnen & Binney 1998). *Hipparcos* data have even been used for exoplanet studies (e.g., Zucker & Mazeh 2001; Snellen & Brown 2018), an entirely unforeseen benefit at the time of mission launch, which occurred six years before the first exoplanet was discovered. For an extensive review of the *Hipparcos*' discoveries, see Perryman (2011).

1.2.2 Gaia

Launched on 19 December 2013, ESA's *Gaia* mission (Gaia Collaboration et al. 2016) is a successor to *Hipparcos*. *Gaia*'s ambitious mission is to survey more than 1 billion stars, which amounts to one per cent of the Galaxy's population. Radial velocities are measured for the brightest 150 million objects. Therefore, *Gaia* is expected to paint the most accurate picture to date of Galactic structure, composition, and formation history. However, *Gaia*'s field of interest

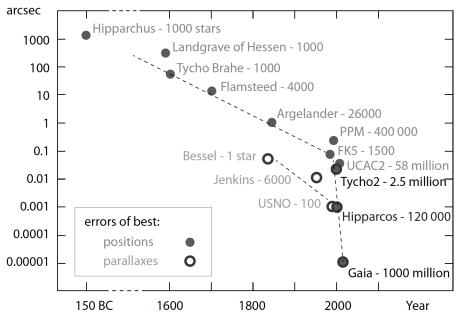

FIGURE 1.5— Improvement in astrometric accuracy over the centuries (Perryman 2011).

is not limited only to Galactic research, but will also include the detection of exoplanets, brown dwarfs, asteroids, and supernovae, etc.

The nominal mission ended after five years of operation and the mission is now in an extended phase that has been approved until 2022, with indications of a further approval until 2025. The most recent data release at the time of writing this thesis is the Gaia Early Data Release 3 (EDR3), which contains a full astrometric solution for $1.468 \cdot 10^9$ sources with limiting magnitude in the G band (330–1050 nm) $G \approx 21$ and radial velocities for 7 million stars, taken from the previous data release.

Although the mission is still in progress, a number of scientific discoveries has already been made thanks to *Gaia*. The vast range of topics that *Gaia* helped explore include Galactic kinematics and dynamics (e.g., Gaia Collaboration et al. 2018b; Antoja et al. 2018; López-Corredoira & Sylos Labini 2019), star clusters (e.g., Cantat-Gaudin et al. 2018; Soubiran et al. 2018; Meingast et al. 2021) hypervelocity stars (e.g., Marchetti et al. 2019; Li et al. 2020; Marchetti 2021), and the solar system (e.g., Gaia Collaboration et al. 2018c; Ďurech & Hanuš 2018; Cellino et al. 2019).

The equipment that enables *Gaia* to gather this impressive dataset consists of three main modules: the payload module, which contains all the instruments and electronics necessary for obtaining and processing the data, the mechanical service module, and electrical service module both of which support the func-

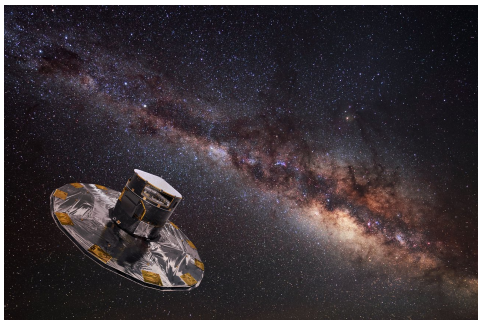

FIGURE 1.6— Artist's impression of the *Gaia* satellite in space. Credit: ESA/ATG medialab, ESO/S. Brunier.

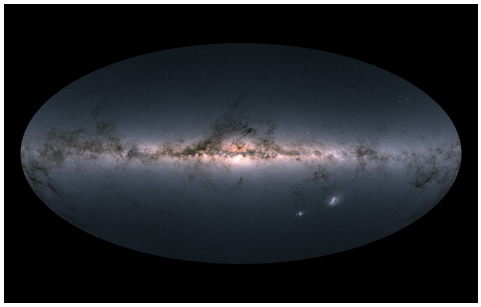

FIGURE 1.7— *Gaia*'s map of the Milky Way, based on observations between 2014 and 2016. Credit: ESA/Gaia/DPAC.

tionality of the spacecraft and its communication with Earth. The scientific equipment of the payload module comprises two identical telescopes, separated by 106.5° that focus the light on a common focal plane and three scientific instruments that analyse the observed light. The astrometric instrument, which works on the same principle as that of *Hipparcos*, but with significantly increased precision, provides the five astrometric parameters (position, proper motion, and parallax). The photometric instrument takes two low-resolution spectra, one G_{BP} in the blue range (330–680 nm) and the other G_{RP} in the red range (640–1050 nm). The third instrument is the radial velocity spectrometer (RVS) which takes high-resolution spectra in a narrow band 845–872 nm down to about 17th magnitude. By measuring Doppler shifts in the detected absorption lines, it reveals the radial velocity of the object under observation.

In this thesis we made use of the second *Gaia* data release, which we describe in greater detail below.

Gaia DR2

The second Gaia data release (Gaia Collaboration et al. 2018a, DR2), released on 25 April 2018 covers observations collected between 25 July 2014 (10:30 UTC) and 23 May 2016 (11:35 UTC). It therefore contains eight additional months' observations compared to the first data release. Gaia DR2 consists of

- 5-parameter astrometric solution for more than $1.3 \cdot 10^9$ stars from magnitude $G \approx 3$ to $G = 21$,
- 7.2 million sources with measured radial velocity with magnitudes between 4 and 13,
- 2-parameter solution (positions on the sky) for an additional 361 million sources, with positional uncertainty at $G = 20$ of about 2 mas,
- Magnitude in the G-band for around $1.69 \cdot 10^9$ sources,
- $G_{\rm BP}$ and $G_{\rm RP}$ photometry for $1.38 \cdot 10^9$ sources,
- Effective temperatures T_{eff} in the range 3000 to 10 000 K for more than 161 million sources, with line-of-sight extinction and reddening given for a subset of about 87 million sources,
- More than 550 000 variable sources,
- Epoch astrometry for over 14 000 solar system objects.

A detailed summary of the contents is given in Figure 1.8. In addition, Gaia DR2 has been crossmatched with many other datasets, including Hipparcos-2, Tycho-2, 2MASS Point Source Catalog, SDSS DR9 and others. However, Gaia DR2 has a number of limitations, including:

- The survey is complete between $G = 12$ mag and $G = 17$ mag (although as mentioned in Chapter 2, at $G = 19$ mag the completeness is 90%), at the bright end ($G \lesssim 7$) the survey is significantly incomplete,
- There is a scan-law pattern due to scan law coverage and data filtering,
- The dataset of high proper motion stars (> 0.6 arcsec/yr) is incomplete,
- There is a parallax zero-point with an average value about -0.03 mas,
- Radial velocities are given only for sources with temperatures in the range 3550–6900 K,
- Astrophysical parameters were estimated only from the three broad-band photometry and parallax on a star-by-star basis. Due to strong degeneracy between T_{eff} and extinction/reddening, estimation of their values has to rely on significant assumptions. Extinction and reddening were estimated using a machine learning algorithm, with a synthetic training dataset and their uncertainties make their use for individual stars unreliable. The training dataset for estimation of T_{eff} is limited to range 3000–10 000 K and shows several strong peaks, that cause artefacts in T_{eff} estimation.

There were also other limitations that are expected to be improved in future releases. Other issues discovered after the data release include inconsistent classification of some sources between the 2- and 5-parameter solutions, small systematic errors in magnitude, and potential contamination of radial velocity values in crowded regions.

1.2.3 Ground-based surveys

In the previous sections we reviewed the amazing leap in our understanding of the Milky Way thanks to space satellites; however, as we shall see in this section, ground-based surveys are still of vital importance for Galactic research.

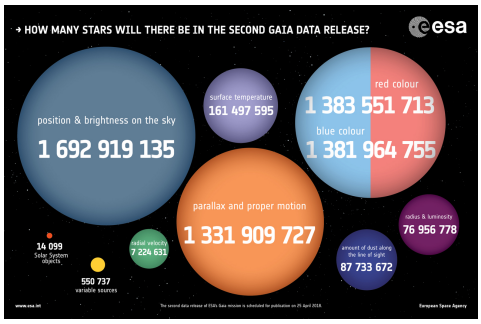

FIGURE 1.8— Gaia DR2 contents. Credit: ESA.

Past and on-going surveys

2MASS

The Two Micron All Sky Survey (Skrutskie et al. 2006, 2MASS) was a near-infrared photometric survey in three filters (J, H, K_s), using two 1.3 m telescopes, located at Mount Hopkins, Arizona (USA), and Cerro Tololo Inter-American Observatory (CTIO), in Chile. The resulting data, which were released in 2003, contain about 472 million sources covering over 99.5% of the sky down to magnitude 15 in the H band. At 2MASS wavelengths, interstellar extinction is greatly reduced, which made 2MASS successful in discovering previously unknown features of the Galaxy, such as the Sagittarius stream (Majewski et al. 2003) and the Monoceros feature (Rocha-Pinto et al. 2003). The Canis Major Dwarf Galaxy, which was the closest known galaxy at the time, was also discovered using 2MASS data (Martin et al. 2004), although this result was later refuted and attributed instead to the effect of the Galactic disc warp (López-Corredoira et al. 2007). 2MASS also contributed to stellar astrophysics, as it discovered many new brown dwarfs and extensively studied low-mass stars.

UKIDSS

The UKIRT Infrared Deep Sky Survey (Lawrence et al. 2007, UKIDSS) is large-scale near infrared survey, conducted on the 3.8 m UK Infrared Telescope

(UKIRT) in Hawaii, with the Wide Field Camera (WFCAM). It is divided into five surveys covering approximately 7500 square degrees in various combinations of filters $ZYJHK$ and H_2. Two surveys are devoted to Galactic research (Galactic Plane Survey and Galactic Clusters Survey), three to extra-Galactic targets, with numerous goals such as finding the nearest and faintest substellar objects, determining the epoch of re-ionization or studying highest-redshift quasars, at z=7. The Galactic Plane Survey is designed to map half of the Milky Way up to latitude $|b| < 5$ degrees and it identified plenty new open clusters and a new category of high-amplitude variables (Lawrence 2013). The main target of the Galactic Clusters Survey is measuring substellar initial mass function, by surveying ten large open star clusters and star formation associations.

In the southern hemisphere, UKIDSS is complemented by the VISTA survey, which we describe below.

VISTA

The Visible and Infrared Survey Telescope for Astronomy (Sutherland et al. 2015, VISTA) is ESO's 4.1 m telescope, located at Cerro Paranal, Chile, equipped with VISTA InfraRed CAMera (VIRCAM). This telescope is dedicated to six public surveys with science goals ranging from exploring small bodies of the Solar System to investigating dark matter and dark energy. The surveys devoted to exploration of the Milky Way are VISTA Variables in the Via Lactea (Minniti et al. 2010, VVV) and VISTA Hemisphere Survey (McMahon et al. 2013, VHS).

VVV is scanning the Galactic bulge and the inner Galactic plane and is designed to detect large number of variable stars. VVV covers area of ~ 520 square degrees, containing $\sim 10^9$ point sources, as well as over 355 open and 33 globular clusters in multiple wavelengths ($ZYJHK_S$)

VHS has several aims, including examination of low mass and nearby stars by imaging the whole southern hemisphere to a depth 30 times fainter than the 2MASS and DENIS surveys, in at least two near-infrared bands (J and K).

Some of the science highlights achieved with VISTA are finding the earliest giant galaxies (Caputi et al. 2015), cataloguing over 84 million stars in the centre of the Milky Way (Saito et al. 2012) or finding ancient globular cluster in the centre of the Galaxy (Minniti et al. 2016).

SDSS

The Sloan Digital Sky Survey (York et al. 2000, SDSS) is a multispectral survey using 2.5-m telescope at the Apache Point Observatory (APO) in New Mexico, USA, using both imaging and spectroscopy. It has five photometric bands

(*ugriz*) with limiting magnitudes 22.0, 22.2, 22.2, 21.3, and 20.5 mag respectively. The original SDSS, now referred to as SDSS Legacy Survey was operating from 2000 to 2008 and its observations resulted in deep imaging of more than 8000 square degrees of the sky, and spectra from over 800 000 galaxies and 100 000 quasars. Since then, SDSS evolved through several stages, currently collecting data for its fifth stage SDSS-V (Kollmeier et al. 2017). The data release is foreseen for 2022 and its three main goals are to obtain spectra of more than 4 million Milky Way stars, explore the local volume, and study black holes using quasars as tracers.

The SDSS comprises several surveys dedicated to cosmology, galaxies, and the Milky Way. The spectrographic surveys studying the Milky Way are:

- **SEGUE**

  A spectroscopic survey, Sloan Extension for Galactic Understanding and Exploration (Yanny et al. 2009, SEGUE) is a part of SDSS, designed to study substructure in the plane and stellar halo of the Milky Way. In its first phase, SEGUE-1, it obtained spectra of ∼240 000 fainter stars ($14.0 \text{ mag} < g < 20.3 \text{ mag}$) of various spectral types. Because of its success, it was developed in a second phase, SEGUE-2, which observed around 120 000 stars, focusing on distant halo stars. Combined data from SEGUE-1 and -2 revealed kinematic and chemical substructure in the halo, which is important for understanding the evolution of the Milky Way and helped constrain existing halo formation models.

- **APOGEE**

  The Apache Point Observatory Galactic Evolution Experiment (Allende Prieto et al. 2008, APOGEE) is a spectroscopic survey of SDSS devoted to the structure and chemistry of the Milky Way. It observes in the *H* band ($1.51\ \mu\text{m} < \lambda < 1.70\ \mu\text{m}$), which makes it more effective in penetrating Galactic dust. The first phase, APOGEE-1, measured chemical abundances, radial velocities, and other stellar parameters for ∼100 000 red giants, distributed in the Galactic bulge, disc, and halo. The second phase, APOGEE-2, was extended to the southern hemisphere from Las Campanas Observatory in Chile and increased the sample size by ∼430 000 stars. APOGEE observations are particularly useful for charting the chemical composition of the Milky Way—necessary information for reconstructing the history and evolution of the Milky Way.

  In this thesis, we made use of data of APOGEE-2 in Chapter 4.

GCS

The Geneva–Copenhagen Survey (Nordström et al. 2004, GCS) is a spectroscopic survey motivated by the *Hipparcos* survey, which measured parallaxes and proper motions accurately, but did not carry out the radial velocity measurements necessary to complete the 6-dimensional phase-space information. GCS therefore focused on measuring radial velocities and metallicity, which it delivered for about 13 500 F and G dwarfs observed with the Danish 1.5-m telescope at ESO in La Silla (Chile) and the Swiss 1-m telescope at Observatoire de Haute-Provence, France. From this sample, metallicity behaviour in the Solar neighbourhood was investigated.

RAVE

The Radial Velocity Experiment (Steinmetz 2003, RAVE) is a spectroscopic survey carried out on the 1.2-m UK Schmidt Telescope at the Australian Astronomical Observatory (AAO). RAVE covered an area of 20 000 deg^2 operating in the wavelength 840–880 nm in the magnitude range 9 mag $< I <$ 12 mag. The final data release, DR6 (Steinmetz et al. 2020), contains nearly half a million stars randomly selected in the southern hemisphere. RAVE data were used for searching for stellar streams (Seabroke et al. 2008), investigating radial migration (Kordopatis et al. 2015), and studying different components of the Milky Way (e.g., Pasetto et al. 2012; Robin et al. 2017).

LAMOST

The Large sky Area Multi-Object fibre Spectroscopic Telescope (Zhao et al. 2012, LAMOST) is a research facility of National Astronomical Observatories of the Chinese Academy of Sciences (NAOC). LAMOST can take 4000 low-resolution spectra in the optical region (365–900 nm) down to magnitude 19 in a single exposure, making it efficient in surveying vast spaces for stars and galaxies. This survey has two main components, one dedicated to galaxies—the LAMOST ExtraGAlactic Survey (LEGAS)—and one focused on the Milky Way—LAMOST Experiment for Galactic Understanding and Exploration (LEGUE). LEGUE (Deng et al. 2012) is divided into three parts: the disc, anticentre, and spheroid, and has a number of scientific goals, including the structure, origin, and evolution of Galactic discs, the search for hypervelocity stars and extremely metal-poor stars, studying open clusters, and many more areas.

GALAH

GALactic Archaeology with HERMES (De Silva et al. 2015, GALAH) is a spectroscopic survey using the High Efficiency and Resolution Multi-Element Spectrograph (HERMES) on the Anglo–Australian Telescope. The mission of GALAH is chemical tagging—it will identify common groups of stars based on their chemical abundances, thus uncovering the formation history of the Galaxy. To do so, it will collect spectra in four optical bands and measure absorption lines from 29 elements for a million relatively bright (12 mag $< V <$ 14 mag) stars. The current data release, DR3 (Buder et al. 2020), contains stellar parameters and elemental abundances for almost 600 000 stars. The GALAH sample will also be useful for other applications, such as thin/thick disc separation, evolution of stellar abundances, identifying streams and others.

GES

The Gaia-ESO (European South Observatory) Survey (Gilmore et al. 2012, GES) uses the Fiber Large Array Multi-Element Spectrograph (FLAMES) of the Very Large Telescope (VLT). GES will survey $\sim 10^5$ stars down to magnitude 19, taken from all the major components of the Milky Way. It will therefore be useful for exploring a range of astrophysical problems, from the Galactic bulge, to the structure of halo. GES will also be crucial in complementing the *Gaia* mission, by measuring radial velocities of fainter stars ($V < 19$ mag), and providing chemical information and astrophysical parameters.

Future surveys

4MOST

The 4-m Multi-Object Spectrograph Telescope (4MOST) is a wide-field optical spectrograph under development for the VISTA telescope, with science operations expected to start in 2023. 4MOST has a $\sim$4 square degree field of view and can take up to 2400 spectra simultaneously, covering most of the optical wavelength range. During the expected 5 years of operation, it will take spectra of more than 20 million objects in the southern sky. The main scientific goal for which 4MOST was designed is to complement space-based surveys such as *Gaia*, eROSITA, Euclid, and Plato, and ground-based wide-area surveys such as the Vera C. Rubin Observatory and the Square Kilometre Array (SKA).

MOONS

The Multi-Object Optical and Near-infrared Spectrograph (Cirasuolo et al. 2012, MOONS) will be a spectrograph for ESO's Very Large Telescope (VLT) in Chile. MOONS is designed to study the evolution of galaxies, including the Milky Way, and provide follow up to *Gaia* and ground-based surveys. MOONS will observe up to 1000 targets across a 25 arcmin field of view and will have both a medium-resolution mode in which the entire wavelength range (0.65–1.8 μm) is observed simultaneously and a high-resolution mode designed for accurate determination of stellar abundances and radial velocities. Thus MOONS will be a multi-purpose instrument promising to deliver data crucial to tackling a range of Galactic, extragalactic, and cosmological problems.

WEAVE

The William Herschel Telescope (WHT) Enhanced Area Velocity Explorer (Dalton et al. 2014, WEAVE) is a new multi-object survey spectrograph for the 4.2-m WHT, located at Roque de los Muchachos Observatory on La Palma in the Canary Islands. WEAVE will significantly increase the observing efficiency of the WHT, since it will take spectra of up to 1000 objects over a two-degree field of view in a single exposure. The vast number of WEAVE's science objectives includes measuring the velocities of objects detected by *Gaia*, surveying galaxy clusters, tracing the evolution of the properties of galactic stellar population, to name just a few.

Vera C. Rubin Observatory

The Vera C. Rubin Observatory, previously known as the Large Synoptic Survey Telescope (LSST Science Collaboration et al. 2009, LSST), is an 8.4-m telescope facility under development at Cerro Pachón, Chile. The Rubin Observatory has a 9.6 square degree field of view and will operate in six bands (*ugrizy*) within the wavelength range 320–1 050 nm. In the covered area of 30 000 deg^2 it is expected to measure 10 billion stars down to magnitude 27.7 and detect an equal number of galaxies. With such state-of-the-art equipment, it will produce the deepest, widest image of the Universe to date, generating about 15 TB of data every night. Ninety per cent of this observing time will be dedicated to the main survey, whose goals are to:

- Study dark energy and dark matter
- Catalogue small objects of the Solar System
- Explore transient astrophysical events

– Map the Milky Way

The remaining 10% of observing will be used for specific projects covering the entire range of astrophysical topics, where the observations will be carried out with deeper coverage and a given field will be observed for an hour every night.

1.3 Motivation for this thesis

As we have reviewed in the previous sections, our knowledge of the Milky Way has evolved significantly. Even though now, in the era of deep space surveys, we know a lot about our Galaxy, there is much left to be understood. The stellar disc at distances greater than 15 kpc from the centre is now one of the most underexplored regions of the Galaxy. Due to their distances and low densities, stellar populations in those regions are difficult to constrain. However, the outer Galactic disc has many interesting features, such as the warp and flare that are still not well explained. Learning which processes predominate this part of our Galaxy is vital for constructing models of galactic evolution and envisaging our Galaxy's future. It is therefore necessary that we find ways to study these distant regions of the Milky Way. In this section, we summarize current knowledge of the outer Galactic disc's features.

1.3.1 Warp

The warp is a deviation of galactic disc from its flat shape (see Figure 1.9). It was first detected in the gaseous component of the Milky Way (Kerr 1957; Oort et al. 1958) and later in the stellar component as well (e.g., Djorgovski & Sosin 1989; Carney & Seitzer 1993). The amplitude and shape of warp in the Milky Way is currently only roughly constrained and is still being debated within the community.

Warps are observed in most spiral galaxies (Sánchez-Saavedra et al. 2003), so they must either be long-lived or triggered very often. There is no consensus on the formation of warps. Several theories have been proposed that are not necessarily mutually exclusive. However, we currently lack sufficient kinematic information to constrain the warp formation mechanism. We review here some of the most discussed theories of warp formation.

Warps as an intrinsic property of galaxies

The first proposed explanation for warps was that they are due to internal mechanisms within the galaxy and are independent of external influences. These theories describe the warp as free normal modes of oscillation in the disc. Kahn

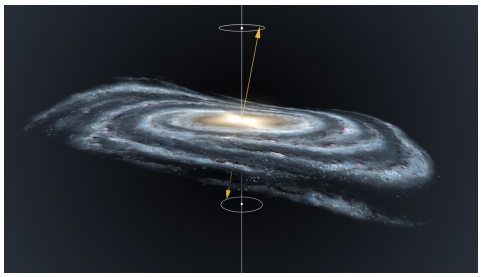

FIGURE 1.9— An artist's impression of the Milky Way warp. Credit: Gabriel Pérez Díaz, SMM (IAC).

& Woltjer (1959) explored the spontaneous generation of warps but concluded that, regardless of the disc's self-gravity, the warp would not be stable and differential precession would shear it. On the other hand, Lynden-Bell (1965) argued that misalignment between the direction of the Galaxy's symmetry axis and that of its angular momentum would generate a long-lived warp. Hunter & Toomre (1969) further analysed this idea and found that the stability of bending modes depends on the density distribution of the disc. More specifically, they conclude that a stable warp would exist in a disc with a sharp edge, where the density falls abruptly, making this a non-favourable mechanism of warp formation in spiral galaxies. Later, several authors explored the influence of the halo on the bending modes (Sparke 1984; Sparke & Casertano 1988; Nelson & Tremaine 1995; Dubinski & Kuijken 1995), but they show that a warp generated by dark matter halo would be quickly dampened. Recent development of this topic has focused on the generation of warps due to bending waves and instabilities arising spontaneously in the galactic disc (Griv et al. 2002; Revaz & Pfenniger 2004; Sánchez-Martín et al. 2016; Chequers & Widrow 2017); however, such warps have very low amplitudes and are incompatible with observations.

The most prevalent modelling of the disc is as a series of concentric, tilted rings (Rogstad et al. 1974), where a warp is brought about by an external torque, which produces rotation of the rings. The external torque may have various sources, some of which we summarise below.

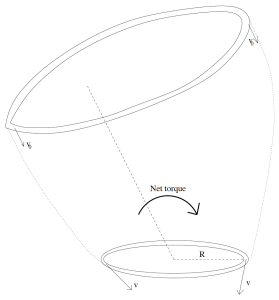

FIGURE 1.10— Schematic representation of the infall of intergalactic flow which produces a net torque on a circular ring in the galactic disc, thus leading to warp formation (López-Corredoira et al. 2002a).

Misaligned infall

One of the most popular explanations for the warp is infall of the intergalactic medium into the halo. Several authors have shown that accretion by the halo of material with misaligned angular momentum can cause the halo to be misaligned with respect to the disc and generates a warp in the disc that is compatible with observations (Ostriker & Binney 1989; Jiang & Binney 1999). Shen & Sellwood (2006) also confirmed the generation of a warp when the disc was modelled with an N-body simulation, the warp following the Brigg's rule (Briggs 1990) and persisting even after removal of the external influence. However, it is not clear how the very low density halo can capture intergalactic matter.

Another theory suggests the accretion of intergalactic matter directly by the disc (López-Corredoira et al. 2002a). They show that infall of matter with a velocity of $\sim$100 km/s and an intergalactic baryon density of $\sim 10^{-25}$ kg/m^3 causes the accretion of $\sim$1 $M_\odot$ per year, which is compatible with observations. This theory also explains the high frequency of warps and the higher warp amplitude of gas compared with the stellar warp.

Tidal gravitational interaction with satellites

The gravitational influence of the Magellanic Clouds (MC) or the Sagittarius dwarf galaxy has been proposed as a source of the Milky Way's warp. Hunter &

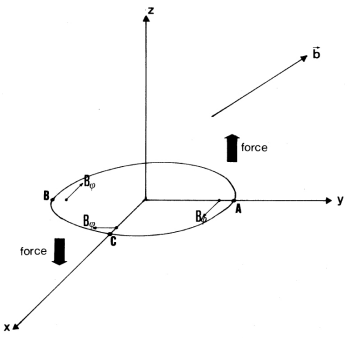

FIGURE 1.11— Schematic representation of warp formation due to intergalactic magnetic force (Battaner et al. 1990).

Toomre (1969) and García-Ruiz et al. (2002) show that gravitational interaction with the Large Magellanic Cloud could produce a warp, but its parameters do not coincide with the warp that we observe. However, Weinberg & Blitz (2006) argue that direct interaction with the MC combined with effect of distortions in the dark matter halo could explain the warp in the HI layer. Bailin (2003) ruled out direct gravitational torque by the Sagittarius galaxy as a cause for the warp, however they do not exclude its interaction via the Milky Way halo as a possible mechanism.

Magnetic fields

Battaner et al. (1990) show that an intergalactic magnetic field of strength 10^{-6}–10^{-8} G could produce a warp in the gaseous disc, assuming that its direction is neither perpendicular nor parallel to the Galactic plane. Battaner & Jiménez-Vicente (1998) further developed this theory and successfully reproduced warp curves for several galaxies with their model, however they were unable to verify the distribution of the magnetic field at high galactocentric radii. Although this is an intriguing idea, it is quite understudied compared to the other theories proposed and there is a lack of observational support for it.

1.3.2 Galactic scale height features and lopsidedness

Most of the matter in the Galaxy is concentrated in a flat disc shape, whose density decreases exponentially in both the radial and vertical directions. Thus the density of the Milky Way is usually modelled as:

$$\rho = \rho_0 e^{-R/h_R} e^{-z/h_Z} \ , \tag{1.1}$$

where h_R is the scale length and h_Z is the scale height. Hundreds of papers have been published with various values of h_R and h_Z but always with the same order of magnitude. Commonly used values are $h_R = 2.5$ kpc and $h_Z = 0.3$ kpc (Jurić et al. 2008).

The scale height has been observed to depend on radius ('flare') and azimuth. These features are relatively mysterious as not enough theoretical work has been done on them.

A non-axisymmetrical density distribution, called lopsidedness, has been observed in ∼30% of galaxies (Jog & Combes 2009). In the Milky Way, lopsidedness was detected in the HI disc at distances $R \gtrapprox 15$ kpc, with more gas in the south (Kalberla & Dedes 2008). As a possible mechanism generating lopsidedness, tidal interactions (e.g., Beale & Davies 1969; Rix & Zaritsky 1995), gas accretion (e.g., Phookun et al. 1993; Bournaud et al. 2005), or internal instability (e.g., Junqueira & Combes 1996; Chan & Junqueira 2003) have been proposed.

A flare is an increase in galactic scale-height with galactocentric radius. A flare has been detected in both the gaseous (Grabelsky et al. 1987; May et al. 1997) and stellar components (Alard 2000; López-Corredoira et al. 2002b; Momany et al. 2006), and have been studied by several authors. Sánchez-Salcedo et al. (2008) analysed the flare using Modified Newtonian Dynamics (MOND), while Narayan & Jog (2002) treated HI, H_2 and stars as gravitationally coupled components of the disc and calculated scale-heights for all three components, with predictions for the flare matching observations very well. More recently, the flare has been studied with SEGUE data (López-Corredoira & Molgó 2014), Cepheids (Feast et al. 2014), and LAMOST (Wang et al. 2018).

To explain the flare's dependence on azimuth, Kalberla et al. (2007) proposed a model with a ring of dark matter embedded in the disc, the radius depending on the azimuth. Saha et al. (2009) modelled it with a lopsided dark matter halo and López-Corredoira & Betancort-Rijo (2009) suggest the accretion of intergalactic matter onto the disc as a possible mechanism to explain both the flare and its dependence on azimuth.

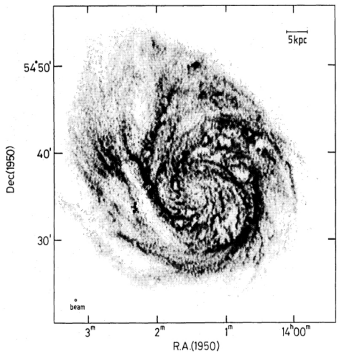

FIGURE 1.12— Example of asymmetry in the HI distribution, called lopsidedness, in M101 (Braun (1995), figure taken from Jog & Combes (2009)).

1.3.3 Kinematic features

The kinematics of the Galaxy has been explored for over a century (e.g., Eggen 1958, 1996; Dehnen 1998; Famaey et al. 2005), however, major strides forward are now being made in the *Gaia* era. An extensive kinematic study surpassing previous work was done by Gaia Collaboration et al. (2018b), who have analysed the region within 5 kpc of the Sun, using only data with parallax error lower than 20% from the Gaia DR2 sample. In this restricted area, there is already a lot of interesting patterns and streaming in all velocity components and their dispersions. López-Corredoira & Sylos Labini (2019) have been able to extend the range of the kinematic maps up to Galactocentric distance 20 kpc, using a deconvolution technique for parallax errors and have found many interesting features. In particular, gradients for all velocity components, departures from circularity in the mean orbits, asymmetries between the northern and the southern Galactic hemispheres, and other attributes, all of which suggest that our Galaxy is far from being in a simple axisymmetric state of equilibrium. Other works have also suggested that Milky Way is in disequilibrium and propose that the Galactic disc has been recently perturbed, probably as the result of the close passage of a massive body (Antoja et al. 2018; Binney & Schönrich 2018). Anal-

ysis of velocities dispersion has also led to a discussion about the lack (Moni Bidin et al. 2012, 2015) or presence (Bovy & Tremaine 2012; Sánchez-Salcedo et al. 2016; Hagen & Helmi 2018) of dark matter in the solar neighbourhood, which is currently still under debate.

1.4 Methodology

In this section we discuss the numerical methods developed during the thesis, along with the software and supercomputing facilities used.

1.4.1 Lucy's method

A common problem in astronomy is that we cannot measure many quantities, such as space velocity or absolute brightness directly, only their apparent values, that are distance-dependent. Thus, a quantity z, is not accessible to the observations via its distribution $h(z)$, but by a function $g(y)$. Following the Bayes' theorem of conditional probabilities, this can be written as

$$g(y) = \int P(y|z)h(z)\mathrm{d}z \ , \tag{1.2}$$

where $P(y|z)\mathrm{d}y$ is the probability that the measured value of observed quantity will fall into the interval $(y, y + \mathrm{d}y)$ (Lucy 1974). Equation (1.2) is an integral equation of the first kind, where the conditional probability density $P(y|z)$ is the kernel, that transforms the unknown function $h(z)$ into $g(y)$, which is considered known. The task is therefore to invert Equation (1.2) to obtain the function $h(z)$.

If the kernel depends only on on the difference of the arguments, Equation (1.2) becomes a convolution (Turchin et al. 1971)

$$g(y) = \int P(y - z)h(z)\mathrm{d}z \ . \tag{1.3}$$

This type of dependence is for instance given in the basic equation of stellar statistics, with g(y) the star counts and h(z) the density along the line of sight. Another classical example of application is the deconvolution of errors, when the observational errors of the function $g(y)$ follow a Gaussian distribution, with variance σ^2. Then the kernel takes form

$$P(y|z) = \frac{1}{\sqrt{2\pi}\sigma} exp\left(-\frac{(y-z)^2}{2\sigma^2}\right) \ . \tag{1.4}$$

Inverting Equation (1.2) is a difficult task, that was explored extensively and several methods were developed to tackle this problem. In this thesis, we used the Lucy's algorithm (Lucy 1974), that finds the solution iteratively. The technique works in the following way. The probability that the quantity z' comes from the interval $(z, z + dz)$ is $Q(z|y)dz$, when it is known that the measured quantity $y' = y$. Then, the probability $y' \in (y, y + \mathrm{d}y)$ and $z' \in (z, z + \mathrm{d}z)$ can be written as $g(y)\mathrm{d}y \times Q(z|y)\mathrm{d}z$. This is identical to the probability that $z' \in (z, z+\mathrm{d}z)$ and $y' \in (y, y+\mathrm{d}y)$, which can be expressed as $h(z)\mathrm{d}z \times P(y|z)\mathrm{d}y$. When we equate these two expressions and substitute Equation (1.2) for $g(y)$ we obtain

$$Q(z|y) = \frac{h(z)P(y|z)}{\int h(z)P(y|z)\mathrm{d}z} \ , \tag{1.5}$$

Bayes' theorem of conditional probabilities and the normalization of the probability $P(y|z)\mathrm{d}z$ yields

$$h(z) = \int g(y)Q(z|y)\mathrm{d}y \ . \tag{1.6}$$

Although it appears that this equation is the inverse of Equation (1.2) with the kernel being $Q(z|y)$, it cannot be used to obtain $h(z)$, because $Q(z|y)$ depends on h. However, Equation (1.5) can be used to generate estimates of h in an iterative procedure. If the function $P(y|z)$ is known, one can calculate an estimate of $Q(z|y)$ by guessing h. Plugging this estimate in Equation (1.6) then leads to an improved estimate of h. This procedure can then be repeated as long as necessary. Thus if h^n is the n-th estimate, the $(n + 1)$-th estimate of h is

$$h(z)^{n+1} = \int g(y)Q^n(z|y)\mathrm{d}y \ , \tag{1.7}$$

where

$$Q^n(z|y) = \frac{h^n(z)P(y|z)}{\int h^n(z)P(y|z)\mathrm{d}z} \ . \tag{1.8}$$

Lucy (1974) proves, that the function $h(z)$ conserves the constraints of probability density

$$\int h(z)\mathrm{d}z = 1 \qquad \text{and} \qquad h(z) \geqslant 0 \tag{1.9}$$

and that it monotonically increases the likelihood and converges to the maximum likelihood after a few iterations.

Lucy's method has been applied to a number of problems in various areas of astrophysics, such as cosmology (e.g., Keeley et al. 2020), galactics (e.g., Raj et al. 2020), solar physics (e.g., Heinzel et al. 2020) but has use even in acoustics (e.g., Xie et al. 2020), geophysics (e.g., Ward et al. 2020), and other fields of science. We apply Lucy's method in Chapter 2, where we describe its application in the case of recovering the distribution of star counts.

There are several other approaches to invert Equation (1.2). A formal solution can be obtained analytically, by applying Fourier transformation. However, an analytical solution is not feasible, because the equation is ill-conditioned—the result is sensitive to noise. As our initial parameters, the observed star counts have inevitable noise, we could not apply typical analytical methods to solve this equation. In cases such as this, statistical algorithms are more robust.

Other notable approaches of inverting Equation (1.2) include Eddington's solution, which expands the kernel in a Taylor series and looks for a solution in form of a series $\Sigma_0^\infty \gamma_k g^{(k)}(y)$ (Eddington 1913; Balázs 1995). Another technique is Malmquist's solution (Malmquist 1924; Balázs 1995), which consists of developing the momenta of $P(y|z)$ in Gram-Charlier series (Kendall & Stuart 1973), without knowing $P(y|z)$ itself. These approaches that approximate the integral with a finite sum do not require significant computational time, however, one has to remember that the parameters estimated this way are not parameters of the unknown $h(z)$, but its integral over Δz, which affects the accuracy of the parameters (Balázs 1995). Another popular method is Expectation-Maximization (EM) algorithm (Dempster et al. 1977; Balázs 1995), which is an iterative method that consists of two steps—E : replacing part of unobserved data with the expected values, based on their conditional probabilities and M : Getting maximum likelihood from the data obtained in the E step. This procedure monotonically converges to the solution. Lucy's method is a special case of an EM algorithm, which is more general and can be used with incomplete data (Balázs 1995).

There are other Bayesian methods for inferring distance from parallax that have been applied to Gaia DR2 (e.g., Astraatmadja & Bailer-Jones 2016; Bailer-Jones et al. 2018; Queiroz et al. 2018), but the indisputable advantage of Lucy's method is that it is model independent.

1.4.2 GADGET-3

In Chapter 3 we use N-body simulations of mock galactic systems, which we compare with our Galaxy. This analysis was performed using the GADGET-3 (GAlaxies with Dark matter and Gas intEracT) cosmological simulation code, which computes the hydrodynamical evolution of a gas by means of smoothed

particle hydrodynamics (SPH). `GADGET-3` is an up-to-date version of the publicly available `GADGET-2` code (Springel 2005), developed by Volker Springel at the Max Planck Institute for Astrophysics and can be applied to a wide range of astrophysical problems.

1.4.3 Supercomputing

In the course of this thesis, we made use of distributed computing via HTCondor, which is is a High Throughput Computing (HTC) system installed at the Instituto de Astrofísica de Canarias (IAC). HTCondor is able to execute a program with different sets of data at multiple machines simultaneously while they are idle. At the IAC, HTCondor has currently around 900 slots available, with memory ranging from 2 to 8 GB and CPU of mostly 2 ,4, or 8 cores, although the most powerful machines have 32 cores. Thus, by running our programs on HTCondor, we were able to reduce the computing time from almost two months to only one day. More information about HTCondor can be found at `https://research.iac.es/sieinvens/siepedia/pmwiki.php?n=HOWTOs.Condor`

1.5 Thesis outline

In this thesis, we aim to shed some light on the outer part of the Galactic disc and study the open questions (mainly the warp) presented in the previous sections. The thesis is structured as follows:

- In Chapter 2, we present a statistical deconvolution method used to calculate distance from parallax. Subsequently, we calculate the density distribution in the outer Galactic disc and analyse its features, mainly the warp.
- In Chapter 3, we continue work of López-Corredoira & Sylos Labini (2019), who derived extended kinematic maps using Gaia DR2. We analyse these maps and study the rotation curves and density distribution, applying both a dark matter model and MOND. We also study the deviations of the Jeans equation from equilibrium and axisymmetry.
- In Chapter 4, we further explore the Galactic warp. We base our work on the first measurement of warp precession by Poggio et al. (2020), which did not take into account the dependence of the warp on the stellar population studied. We present our own calculation, where we show that there is no need for a high warp precession.

- In Chapter 5, we summarize our main conclusions and outline prospects for future work.

Bibliography

Alard, C. 2000, arXiv e-prints, astro-ph/0007013

Allende Prieto, C., Majewski, S. R., Schiavon, R., et al. 2008, Astronomische Nachrichten, 329, 1018

Antoja, T., Helmi, A., Romero-Gómez, M., et al. 2018, Nature, 561, 360

Astraatmadja, T. L. & Bailer-Jones, C. A. L. 2016, ApJ, 832, 137

Bahcall, J. N. & Soneira, R. M. 1980, ApJS, 44, 73

Bailer-Jones, C. A. L., Rybizki, J., Fouesneau, M., Mantelet, G., & Andrae, R. 2018, AJ, 156, 58

Bailin, J. 2003, ApJL, 583, L79

Balázs, L. G. 1995, Inverse Problems, 11, 731

Battaner, E., Florido, E., & Sanchez-Saavedra, M. L. 1990, A&A, 236, 1

Battaner, E. & Jiménez-Vicente, J. 1998, A&A, 332, 809

Beale, J. S. & Davies, R. D. 1969, Nature, 221, 531

Binney, J. & Schönrich, R. 2018, MNRAS, 481, 1501

Bok, B. J., Bester, M. J., & Wade, C. M. 1953, AJ, 58, 36

Bournaud, F., Combes, F., Jog, C. J., & Puerari, I. 2005, A&A, 438, 507

Bovy, J. & Tremaine, S. 2012, ApJ, 756, 89

Braun, R. 1995, A&AS, 114, 409

Briggs, F. H. 1990, ApJ, 352, 15

Buder, S., Sharma, S., Kos, J., et al. 2020, arXiv e-prints, arXiv:2011.02505

Cantat-Gaudin, T., Jordi, C., Vallenari, A., et al. 2018, A&A, 618, A93

Caputi, K. I., Ilbert, O., Laigle, C., et al. 2015, ApJ, 810, 73

Carney, B. W. & Seitzer, P. 1993, AJ, 105, 2127

Cellino, A., Hestroffer, D., Lu, X. P., Muinonen, K., & Tanga, P. 2019, A&A, 631, A67

Chan, R. & Junqueira, S. 2003, ApJ, 586, 780

Chequers, M. H. & Widrow, L. M. 2017, MNRAS, 472, 2751

Cirasuolo, M., Afonso, J., Bender, R., et al. 2012, in Society of Photo-Optical Instrumentation Engineers (SPIE) Conference Series, Vol. 8446, Ground-based and Airborne Instrumentation for Astronomy IV, ed. I. S. McLean, S. K. Ramsay, & H. Takami, 84460S

Dalton, G., Trager, S., Abrams, D. C., et al. 2014, in Society of Photo-Optical Instrumentation Engineers (SPIE) Conference Series, Vol. 9147, Ground-based and Airborne Instrumentation for Astronomy V, ed. S. K. Ramsay, I. S. McLean, & H. Takami, 91470L

De Silva, G. M., Freeman, K. C., Bland-Hawthorn, J., et al. 2015, MNRAS, 449, 2604

Deason, A. J., Fattahi, A., Frenk, C. S., et al. 2020, MNRAS, 496, 3929

Dehnen, W. 1998, AJ, 115, 2384

Dehnen, W. & Binney, J. J. 1998, MNRAS, 298, 387

Dempster, A. P., Laird, N. M., & Rubin, D. B. 1977, J. R. Stat. Soc. B, 39, 1

Deng, L.-C., Newberg, H. J., Liu, C., et al. 2012, Research in Astronomy and Astrophysics, 12, 735

Dick, S. J. 2020, Discovering a New Realm of the Universe: Hubble, Galaxies, and Classification (Cham: Springer International Publishing), 611–625

Djorgovski, S. & Sosin, C. 1989, ApJL, 341, L13

Dubinski, J. & Kuijken, K. 1995, ApJ, 442, 492

Ďurech, J. & Hanuš, J. 2018, A&A, 620, A91

Eddington, A. S. 1913, MNRAS, 73, 359

Eggen, O. J. 1958, MNRAS, 118, 65

Eggen, O. J. 1996, AJ, 112, 1595

Epchtein, N., de Batz, B., Copet, E., et al. 1994, Astrophysics and Space Science, 217, 3

ESA. 1997, ESA SP-1200

Famaey, B., Jorissen, A., Luri, X., et al. 2005, A&A, 430, 165

Feast, M. W., Menzies, J. W., Matsunaga, N., & Whitelock, P. A. 2014, Nature, 509, 342

Gaia Collaboration, Brown, A. G. A., Vallenari, A., et al. 2018a, A&A, 616, A1

Gaia Collaboration, Katz, D., Antoja, T., et al. 2018b, A&A, 616, A11

Gaia Collaboration, Prusti, T., de Bruijne, J. H. J., et al. 2016, A&A, 595, A1

Gaia Collaboration, Spoto, F., Tanga, P., et al. 2018c, A&A, 616, A13

García-Ruiz, I., Kuijken, K., & Dubinski, J. 2002, MNRAS, 337, 459

Garzón, F., Hammersley, P. L., Mahoney, T., et al. 1993, MNRAS, 264, 773

Gillessen, S., Plewa, P. M., Eisenhauer, F., et al. 2017, ApJ, 837, 30

Gilmore, G., Randich, S., Asplund, M., et al. 2012, The Messenger, 147, 25

Grabelsky, D. A., Cohen, R. S., Bronfman, L., Thaddeus, P., & May, J. 1987, ApJ, 315, 122

Griv, E., Gedalin, M., & Yuan, C. 2002, ApJL, 580, L27

Habing, H. & Epchtein, N. 1998, `http://cdsweb.u-strasbg.fr/DENIS/denis-0598.htx` [Accessed: 2021-05-05]

Hagen, J. H. J. & Helmi, A. 2018, A&A, 615, A99

Heinzel, P., Schwartz, P., Lörinčík, J., et al. 2020, ApJL, 896, L35

Herschel, W. 1785, Philosophical Transactions of the Royal Society of London Series I, 75, 213

Høg, E., Fabricius, C., Makarov, V. V., et al. 2000, A&A, 355, L27

Hog, E. & Petersen, J. O. 1997, A&A, 323, 827

Hubble, E. P. 1926, ApJ, 63, 236

Hubble, E. P. 1936, Realm of the Nebulae

Hunter, C. & Toomre, A. 1969, ApJ, 155, 747

Infante, L. 1986, Astronomical Society of the Pacific, 98, 360

Jansky, K. G. 1933, Nature, 132, 66

Jeans, J. H. 1928, Astronomy and cosmogony

Jiang, I.-G. & Binney, J. 1999, MNRAS, 303, L7

Jog, C. J. & Combes, F. 2009, Physics Reports, 471, 75

Junqueira, S. & Combes, F. 1996, A&A, 312, 703

Jurić, M., Ivezić, Ž., Brooks, A., et al. 2008, ApJ, 673, 864

Kahn, F. D. & Woltjer, L. 1959, ApJ, 130, 705

Kalberla, P. M. W. & Dedes, L. 2008, A&A, 487, 951

Kalberla, P. M. W., Dedes, L., Kerp, J., & Haud, U. 2007, A&A, 469, 511

Keeley, R. E., Shafieloo, A., Hazra, D. K., & Souradeep, T. 2020, Journal of Cosmology and Astroparticle Physics, 2020, 055

Kendall, M. G. & Stuart, A. 1973, The advanced theory of statistics vol I (London : Charles Griffin)

Kerr, F. J. 1957, AJ, 62, 93

Kollmeier, J. A., Zasowski, G., Rix, H.-W., et al. 2017, arXiv e-prints, arXiv:1711.03234

Kordopatis, G., Binney, J., Gilmore, G., et al. 2015, MNRAS, 447, 3526

Lawrence, A. 2013, in Thirty Years of Astronomical Discovery with UKIRT, Vol. 37, 271

Lawrence, A., Warren, S. J., Almaini, O., et al. 2007, MNRAS, 379, 1599

Li, J., Jia, S., Gao, Y., et al. 2020, Research in Astronomy and Astrophysics, 20, 042

Lin, C. C. & Shu, F. H. 1964, ApJ, 140, 646

Lindblad, B. 1925, Arkiv for Matematik, Astronomi och Fysik, 21, 1

López-Corredoira, M. & Betancort-Rijo, J. 2009, A&A, 493, L9

López-Corredoira, M., Betancort-Rijo, J., & Beckman, J. E. 2002a, A&A, 386, 169

López-Corredoira, M., Cabrera-Lavers, A., Garzón, F., & Hammersley, P. L. 2002b, A&A, 394, 883

López-Corredoira, M. & Molgó, J. 2014, A&A, 567, A106

López-Corredoira, M., Momany, Y., Zaggia, S., & Cabrera-Lavers, A. 2007, A&A, 472, L47

López-Corredoira, M. & Sylos Labini, F. 2019, A&A, 621, A48

LSST Science Collaboration, Abell, P. A., Allison, J., et al. 2009, arXiv e-prints, arXiv:0912.0201

Lucy, L. B. 1974, AJ, 79, 745

Lynden-Bell, D. 1965, MNRAS, 129, 299

Majewski, S. R., Skrutskie, M. F., Weinberg, M. D., & Ostheimer, J. C. 2003, ApJ, 599, 1082

Malmquist, K. G. 1924, Meddelanden fran Lunds Astronomiska Observatorium Serie II, 32, 3

Marchetti, T. 2021, MNRAS, 503, 1374

Marchetti, T., Rossi, E. M., & Brown, A. G. A. 2019, MNRAS, 490, 157

Martin, N. F., Ibata, R. A., Bellazzini, M., et al. 2004, MNRAS, 348, 12

May, J., Alvarez, H., & Bronfman, L. 1997, A&A, 327, 325

McMahon, R. G., Banerji, M., Gonzalez, E., et al. 2013, The Messenger, 154, 35

Meingast, S., Alves, J., & Rottensteiner, A. 2021, A&A, 645, A84

Minniti, D., Contreras Ramos, R., Zoccali, M., et al. 2016, ApJL, 830, L14

Minniti, D., Lucas, P. W., Emerson, J. P., et al. 2010, New Astronomy, 15, 433

Momany, Y., Zaggia, S., Gilmore, G., et al. 2006, A&A, 451, 515

Moni Bidin, C., Carraro, G., Méndez, R. A., & Smith, R. 2012, ApJ, 751, 30

Moni Bidin, C., Smith, R., Carraro, G., Méndez, R. A., & Moyano, M. 2015, A&A, 573, A91

Morgan, W. W., Sharpless, S., & Osterbrock, D. 1952, AJ, 57, 3

Narayan, C. A. & Jog, C. J. 2002, A&A, 394, 89

Nelson, R. W. & Tremaine, S. 1995, MNRAS, 275, 897

Neugebauer, G. & Leighton, R. B. 1969, Two-micron sky survey. A preliminary catalogue

Nordström, B., Mayor, M., Andersen, J., et al. 2004, A&A, 418, 989

Oort, J. H. 1927, Bulletin of the Astronomical Institutes of the Netherlands, 3, 275

Oort, J. H. 1955, Vistas in Astronomy, 1, 607

Oort, J. H., Kerr, F. J., & Westerhout, G. 1958, MNRAS, 118, 379

Ostriker, E. C. & Binney, J. J. 1989, MNRAS, 237, 785

Pasetto, S., Grebel, E. K., Zwitter, T., et al. 2012, A&A, 547, A71

Perryman, M. 2011, A&A Rev., 19, 45

Phookun, B., Vogel, S. N., & Mundy, L. G. 1993, ApJ, 418, 113

Poggio, E., Drimmel, R., Andrae, R., et al. 2020, Nature Astronomy, 4, 590

Queiroz, A. B. A., Anders, F., Santiago, B. X., et al. 2018, MNRAS, 476, 2556

Raj, M. A., Iodice, E., Napolitano, N. R., et al. 2020, A&A, 640, A137

Reid, N. 1990, MNRAS, 247, 70

Reid, N. & Gilmore, G. 1982, MNRAS, 201, 73

Revaz, Y. & Pfenniger, D. 2004, A&A, 425, 67

Rix, H.-W. & Zaritsky, D. 1995, ApJ, 447, 82

Robin, A. C., Bienaymé, O., Fernández-Trincado, J. G., & Reylé, C. 2017, A&A, 605, A1

Rocha-Pinto, H. J., Majewski, S. R., Skrutskie, M. F., & Crane, J. D. 2003, ApJL, 594, L115

Rogstad, D. H., Lockhart, I. A., & Wright, M. C. H. 1974, ApJ, 193, 309

Saha, K., Levine, E. S., Jog, C. J., & Blitz, L. 2009, ApJ, 697, 2015

Saito, R. K., Minniti, D., Dias, B., et al. 2012, A&A, 544, A147

Sánchez-Martín, P., Romero-Gómez, M., & Masdemont, J. J. 2016, A&A, 588, A76

Sánchez-Saavedra, M. L., Battaner, E., Guijarro, A., López-Corredoira, M., & Castro-Rodríguez, N. 2003, A&A, 399, 457

Sánchez-Salcedo, F. J., Flynn, C., & de Diego, J. A. 2016, ApJ, 817, 13

Sánchez-Salcedo, F. J., Saha, K., & Narayan, C. A. 2008, MNRAS, 385, 1585

Seabroke, G. M., Gilmore, G., Siebert, A., et al. 2008, MNRAS, 384, 11

Shapley, H. & Curtis, H. D. 1921, Bulletin of the National Research Council, 2, 171

Shen, J. & Sellwood, J. A. 2006, MNRAS, 370, 2

Skrutskie, M. F., Cutri, R. M., Stiening, R., et al. 2006, The Astronomical Journal, 131, 1163

Smart, R. L., Drimmel, R., Lattanzi, M. G., & Binney, J. J. 1998, Nature, 392, 471

Snellen, I. A. G. & Brown, A. G. A. 2018, Nature Astronomy, 2, 883

Söderhjelm, S. 1999, A&A, 341, 121

Soubiran, C., Cantat-Gaudin, T., Romero-Gómez, M., et al. 2018, A&A, 619, A155

Sparke, L. S. 1984, ApJ, 280, 117

Sparke, L. S. & Casertano, S. 1988, MNRAS, 234, 873

Springel, V. 2005, MNRAS, 364, 1105

Steinmetz, M. 2003, in Astronomical Society of the Pacific Conference Series, Vol. 298, GAIA Spectroscopy: Science and Technology, ed. U. Munari, 381

Steinmetz, M., Matijevič, G., Enke, H., et al. 2020, AJ, 160, 82

Sutherland, W., Emerson, J., Dalton, G., et al. 2015, A&A, 575, A25

Toomre, A. 1981, in Structure and Evolution of Normal Galaxies, ed. S. M. Fall & D. Lynden-Bell, 111–136

Trumpler, R. J. 1930, Lick Observatory Bulletin, 420, 154

Turchin, V. F., Kozlov, V. P., & Malkevich, M. S. 1971, Soviet Physics Uspekhi, 13, 681

Wang, H. F., Liu, C., Xu, Y., Wan, J.-C., & Deng, L. 2018, MNRAS, 478, 3367

Ward, J., Nowacki, A., & Rost, S. 2020, Geochemistry, Geophysics, Geosystems, 21, e09025

Way, M. J. 2013, in Astronomical Society of the Pacific Conference Series, Vol. 471, Origins of the Expanding Universe: 1912-1932, ed. M. J. Way & D. Hunter, 97

Weinberg, M. D. & Blitz, L. 2006, ApJL, 641, L33

Weistrop, D. 1972, AJ, 77, 366

Wright, T. 1750, An original theory or new hypothesis of the universe : founded upon the laws of nature, and solving by mathematical principles the general phænomena of the visible creation; and particularly the Via Lactea.

Xie, L., Sun, C., & Tian, J. 2020, Acoustical Society of America Journal, 148, EL440

Yanny, B., Rockosi, C., Newberg, H. J., et al. 2009, AJ, 137, 4377

York, D. G., Adelman, J., Anderson, John E., J., et al. 2000, AJ, 120, 1579

Zhao, G., Zhao, Y.-H., Chu, Y.-Q., Jing, Y.-P., & Deng, L.-C. 2012, Research in Astronomy and Astrophysics, 12, 723

Zucker, S. & Mazeh, T. 2001, ApJ, 562, 549

2

Structure of the outer Galactic disc with Gaia DR2

As we discussed in the previous chapter, studying the outer Galactic disc is a complicated task, since we cannot measure large distances directly from parallax with sufficient precision. The *Gaia* survey brought data of the highest quality and accuracy to date, but even for the most recent *Gaia* data release (DR2) the measurement of parallax is accurate for galactocentric distances up to only ∼13 kpc. Therefore, in order to infer distances from parallax in the outer disc, we had to apply a statistical method to get the deconvolution of parallax errors. We use Lucy's method to recover the star density as a function of distance, reaching galactocentric distances of about 20 kpc. Then we analysed the density distribution and study its properties.

Several interesting features making the disc distorted from a simple flat shape can be directly seen from the maps. We confirm that there is no cut-off in the Milky Way at least until $R \sim 20$ kpc, and that the density distribution in the plane can be fitted with a single exponential function in the radial direction with a scale-height that has a small dependence on azimuth.

The most prominent feature that we analysed is the Galactic warp. We fit the density maps with various warp models. When we apply a model combining two sinusoids, we find that the warp is asymmetric, the northern warp being larger than the southern one by ∼25%. The warp amplitude is lower than measured previously, reaching a maximum height of only ∼0.5 kpc at a distance of 20 kpc. The only other studies capable of calculating warp parameters at such

high distances have used Cepheids (e.g., Chen et al. 2020, Skowron at al. 2020), as the distances of these variables can be measured accurately, even in the outer disc. When we compare our result with those derived from Cepheids, we find an interesting relationship between the age of the studied population and its warp amplitude. It is clear that a young stellar population of Cepheids has a significantly higher warp than the stellar population as a whole, which is old on average. To confirm this, we also analysed very luminous stars ($M_G < -2$ mag) separately. These stars represent a younger population on average. The warp for this population has a 20–30% greater amplitude, thus confirming the finding that the warp amplitude grows for younger population. However, it is still 2–3 times lower than the amplitude measured with Cepheids, which are very young stars (a hundred Myr old at most). This is also in good agreement with observations of the warp in gas, which has a significantly higher amplitude than the stellar warp (Reylé et al. 2009), and the young stars are tracing the gas. Our result therefore favours the accretion model of warp formation, as gravitational mechanisms should influence all components of the disc in the same way.

This work was published in the following article:
Astronomy and Astrophysics (2020), 'Structure of the outer Galactic disc with *Gaia* DR2', **637**, A96.
The article is attached in the following pages.

A&A 637, A96 (2020)
https://doi.org/10.1051/0004-6361/201937289

Astronomy & Astrophysics

Structure of the outer Galactic disc with *Gaia* DR2

Ž. Chrobáková[1,2], R. Nagy[3], and M. López-Corredoira[1,2]

[1] Instituto de Astrofísica de Canarias, 38205 La Laguna, Tenerife, Spain
e-mail: zofiachrobakova@gmail.com
[2] Departamento de Astrofísica, Universidad de La Laguna, 38206 La Laguna, Tenerife, Spain
[3] Faculty of Mathematics, Physics, and Informatics, Comenius University, Mlynská dolina, 842 48 Bratislava, Slovakia

Received 9 December 2019 / Accepted 31 March 2020

ABSTRACT

Context. The structure of outer disc of our Galaxy is still not well described, and many features need to be better understood. The second *Gaia* data release (DR2) provides data in unprecedented quality that can be analysed to shed some light on the outermost parts of the Milky Way.
Aims. We calculate the stellar density using star counts obtained from *Gaia* DR2 up to a Galactocentric distance $R = 20$ kpc with a deconvolution technique for the parallax errors. Then we analyse the density in order to study the structure of the outer Galactic disc, mainly the warp.
Methods. In order to carry out the deconvolution, we used the Lucy inversion technique for recovering the corrected star counts. We also used the *Gaia* luminosity function of stars with $M_G < 10$ to extract the stellar density from the star counts.
Results. The stellar density maps can be fitted by an exponential disc in the radial direction $h_r = 2.07 \pm 0.07$ kpc, with a weak dependence on the azimuth, extended up to 20 kpc without any cut-off. The flare and warp are clearly visible. The best fit of a symmetrical S-shaped warp gives $z_w \approx z_\odot + (37 \pm 4.2(\text{stat.}) - 0.91(\text{syst.}))\text{pc} \cdot (R/R_\odot)^{2.42\pm0.76(\text{stat.})\pm0.129(\text{syst.})} \sin(\phi + 9.3^\circ \pm 7.37^\circ(\text{stat.}) + 4.48^\circ(\text{syst.}))$ for the whole population. When we analyse the northern and southern warps separately, we obtain an asymmetry of an ~25% larger amplitude in the north. This result may be influenced by extinction because the *Gaia G* band is quite prone to extinction biases. However, we tested the accuracy of the extinction map we used, which shows that the extinction is determined very well in the outer disc. Nevertheless, we recall that we do not know the full extinction error, and neither do we know the systematic error of the map, which may influence the final result. The analysis was also carried out for very luminous stars alone ($M_G < -2$), which on average represents a younger population. We obtain similar scale-length values, while the maximum amplitude of the warp is 20–30% larger than with the whole population. The north-south asymmetry is maintained.

Key words. Galaxy: disk – Galaxy: structure

1. Introduction

Studying the Galactic structure is crucial for our understanding of the Milky Way. Star counts are widely used for this purpose (Paul 1993), and the importance of this tool has increased in the past decades with the appearance of wide-area surveys (Bahcall 1986; Majewski 1993), which made it possible to obtain reliable measurements of the Galactic thin- and thick-disc and halo (Chen et al. 2001; Jurić et al. 2008; Bovy et al. 2012; Robin et al. 2012). It is common to simplify the Galactic disc as an exponential or hyperbolic secant form, but there are many asymmetries such as the flare and warp that need to be taken into account. These structures can be seen from 3D distribution of stars, as shown by Liu et al. (2017), who mapped the Milky Way using the LAMOST (The Large Sky Area Multi-Object Fibre Spectroscopic Telescope) RGB (red-giant branch) stars; Skowron et al. (2019a), who constructed a map of the Milky Way from classical Cepheids; or Anders et al. (2019), who used the second *Gaia* data release (DR2).

The warp was first detected in the Galactic gaseous disc in 21 cm HI observations (Kerr 1957; Oort et al. 1958). Since then, the warp has also been discovered in the stellar disc (Carney & Seitzer 1993; López-Corredoira et al. 2002a; Reylé et al. 2009; Amôres et al. 2017; Chen et al. 2019), and the kinematics of the warp has been studied as well (Dehnen 1998; Drimmel et al. 2003; López-Corredoira et al. 2014; Schönrich & Dehnen 2018).

Vertical kinematics in particular can reveal much about the mechanism behind the formation of warp. Poggio et al. (2018) found a gradient of 5–6 km s^{-1} in the vertical velocities of upper main-sequence stars and giants located from 8 to 14 kpc in Galactic radius using *Gaia* DR2 data, revealing the kinematic signature of the warp. Their findings suggest that the warp is principally a gravitational phenomenon. Skowron et al. (2019b) also found a strong gradient in vertical velocities using classical Cepheids supplemented by the OGLE (Optical Gravitational Lensing Experiment) survey. López-Corredoira et al. (2020) investigated the dynamical effects produced by different mechanisms that can explain the radial and vertical components of extended kinematic maps of López-Corredoira & Sylos-Labini (2019), who used Lucy's deconvolution method (see Sect. 4.1) to produce kinematical maps up to a Galactocentric radius of 20 kpc. López-Corredoira et al. (2020) found that vertical motions might be dominated by external perturbations or mergers, although with a minor component due to a warp whose amplitude is evolving with time. However, the kinematic signature of the warp is not enough to explain the observed velocities.

To date, the shape of the warp has been constrained only roughly, and the kinematical information is not satisfying

A&A 637, A96 (2020)

enough to reach consensus about the mechanism causing the warp. Theories include accretion of intergalactic matter onto the disc (López-Corredoira et al. 2002b), interaction with other satellites (Kim et al. 2014), the intergalactic magnetic field (Battaner et al. 1990), a misaligned rotating halo (Debattista & Sellwood 1999), and others.

We now have a new opportunity to improve our knowledge about the Milky Way significantly through the *Gaia* mission of the European Space Agency (Gaia Collaboration et al. 2016). *Gaia* data provide unprecedented positional and radial velocity measurements and an accurate distance determination, although the error of the parallax measurement increases with distance from us. It brings us the most accurate data about the Galaxy so far, ideal to advance in all branches of Galactic astrophysics and study our Galaxy in greater detail than ever before. *Gaia* DR2 has been used by Anders et al. (2019), who provided photo-astrometric distances, extinctions, and astrophysical parameters up to magnitude $G = 18$, making use of the Bayesian parameter estimation code `StarHorse`. After introducing the observational data and a number of priors, their code finds the Bayesian stellar parameters, distances, and extinctions. The authors also present density maps, which we compare with our results in Sect. 4.3. *Gaia* data have also been used to study the structure of outer Galactic disc, especially the warp and the flare. The first *Gaia* data release brought some evidence of the warp (Schönrich & Dehnen 2018), but the more extensive second data release provides a better opportunity to study the warp attributes. Poggio et al. (2018) combined *Gaia* DR2 astrometry with 2MASS (Two Micron All-Sky Survey) photometry and revealed the kinematic signature of the warp up to 7 kpc from the Sun. Li et al. (2019) found the flare and the warp in the Milky Way, using only OB stars of the *Gaia* DR2. In this work, we make use of *Gaia* DR2 data as described in Sect. 2 and use star counts to obtain the stellar density by applying Lucy's inversion technique. Then we analyse the density maps to determine the warp.

The paper is structured as follows: in Sect. 2 we describe the *Gaia* data and extinction maps that we used, in Sect. 3 we present the luminosity function used in our calculations, in Sect. 4 we explain the methods for obtaining our density maps, and in Sect. 5 we discuss the results. In Sect. 5.4 we present the exponential fits of the density, in Sect. 5.5 we study the warp, and in Sect. 5.6 we repeat the previous analysis of the young population.

2. Data selection

We used data of the second *Gaia* data release (Gaia Collaboration et al. 2018) here, which were collected during first 22 months of observation. We are interested in stars with known five-parameter astrometric solution: more than 1.3 billion sources. G magnitudes, collected by astrometric instrument in the white-light G-band of *Gaia* (330–1050 nm) are known for all sources, with precisions varying from around 1 millimag at the bright ($G < 13$) end to around 20 millimag at $G = 20$. For the details on the astrometric data processing and validation of these results, see Lindegren et al. (2018). We chose stars with apparent magnitude up to $G = 19$, where the catalogue is complete up to 90% (Arenou et al. 2018). We chose data with a parallax in the interval Anders et al. (2019) mas.

In our analysis, we did not consider any zero-point bias in the parallaxes of *Gaia* DR2, as found by some authors (Lindegren et al. 2018; Arenou et al. 2018; Stassun & Torres 2018; Zinn et al. 2019), except in Sect. 4.3, where we repeat our main calculation including a non-zero value of the zero-point to prove that this effect is negligible in our results.

We used two different extinction maps. For the luminosity function (Sect. 3), we used the extinction map of Green et al. (2018) through its Python package *dustmaps*, choosing the *Bayestar17* version. This map covers 75% of the sky (declinations of $\delta \gtrsim -30°$) and provides reddening in similar units as Schlegel et al. (1998, SFD).

To calculate the density (Sect. 4), we need to cover the whole sky, therefore we used the three-dimensional less accurate but full-sky extinction map of Bovy et al. (2016) through its Python package *mwdust*. This map combines the results of Marshall et al. (2006), Green et al. (2015), and Drimmel et al. (2003) and provides reddening as defined in Schlegel et al. (1998).

In order to convert the interstellar reddening of these maps into $E(B-V)$, we used coefficients (Hendy 2018; Rybizki et al. 2018)

$$A_G/A_v = 0.859,$$
$$R_V = A_v/E(B-V) = 3.1. \quad (1)$$

3. Luminosity function

To construct the luminosity function, we chose all stars with heliocentric distance $d < 0.5$ kpc (distances determined as $1/\pi$, where π is the parallax). We did not find many bright stars ($M_G < -5$) in this area, therefore we also chose a specific region with Galactic height $|z| < 1$ kpc and Galactocentric distance $R < 5$ kpc, in which we only selected stars with absolute magnitude $M_G < -5$. We normalised the counts of stars with high magnitude and then joined these two parts to create the luminosity function.

In the range of distance that we used for the luminosity function, the star counts are complete for the absolute magnitude that we are calculating, except perhaps for the possible loss of the brightest stars through saturation at $M_G < -5$. Moreover, the error in the parallax for these stars is negligible, so that the calculation of the absolute magnitude from the apparent magnitude is quite accurate. We did not take into account the variations of the luminosity function throughout the Galactic disc. We assumed that it does not change.

The luminosity function we obtained is shown in Fig. 1. We interpolated the luminosity function with a spline $N = \mathrm{spl}(M)$ of the first degree. The result is shown in Fig. 2. For the interpolation, we used values between magnitudes $M = [-5, 10]$ because the values outside this interval are unreliable, and we used the extrapolation of the spline function to lower magnitudes. The values of the luminosity function are listed in Table 1.

4. Density maps

4.1. Deconvolution of star counts

To calculate the stellar density, we need to measure star counts as a function of distance. However, the error of parallax increases with distance from us, which means that our analysis would be correct only within roughly 5 kpc from the Sun. To be able to reach higher distances, we corrected for this effect using the method developed by López-Corredoira & Sylos-Labini (2019), who used Lucy's deconvolution method (Lucy 1974; see Appendix A) to obtain an accurate distance measurement up to $R = 20$ kpc. They expressed the observed number of stars per parallax $\bar{N}(\pi)$ as a convolution of the real number $N(\pi)$ of stars

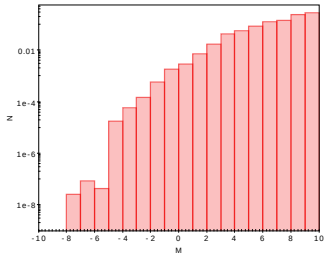

Fig. 1. Luminosity function.

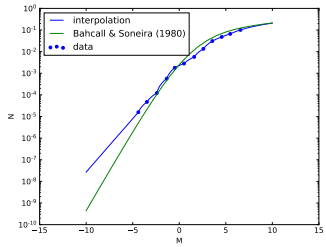

Fig. 2. Interpolation of the luminosity function with a spline compared with the luminosity function of Bahcall & Soneira (1980). These two functions are not directly comparable because Bahcall & Soneira (1980) used a slightly different filter in the visible, but it shows that our luminosity function is reasonable.

with a Gaussian function

$$\overline{N}(\pi) = \int_0^\infty \mathrm{d}\pi' N(\pi') G_{\pi'}(\pi - \pi'), \tag{2}$$

where

$$G_\pi(x) = \frac{1}{\sqrt{2\pi}\sigma_\pi} \mathrm{e}^{-\frac{x^2}{2\sigma_\pi^2}}. \tag{3}$$

For the error σ_π we averaged errors of every bin, which we calculated from values given by *Gaia* DR2.

We only used the parallax between Anders et al. (2019) mas. For the upper limit the relative error of parallax is very small and does not produce any bias. For the lower limit, the truncation avoiding the negative parallaxes affects the distribution of parallaxes and statistical properties (average, median, etc.) (Luri et al. 2018, Sect. 3.3). However, in our method we do not calculate the average distance from the average parallax. We used Lucy's method, which iterates the counts of the stars with positive parallaxes until we obtained the final solution. This does not

Table 1. Values of the luminosity function.

M_G	N
−10	2.704×10^{-8}
−9	8.424×10^{-8}
−8	2.625×10^{-7}
−7	8.177×10^{-7}
−6	2.547×10^{-6}
−5	7.936×10^{-6}
−4	2.927×10^{-5}
−3	8.028×10^{-5}
−2	2.936×10^{-4}
−1	1.066×10^{-3}
0	2.299×10^{-3}
1	4.117×10^{-3}
2	8.805×10^{-3}
3	2.081×10^{-2}
4	3.838×10^{-2}
5	5.667×10^{-2}
6	8.273×10^{-2}
7	0.122
8	0.171
9	0.221
10	0.27

mean that we truncated the star counts with negative parallaxes. We used only the stars with positive parallaxes as is required by our method, explained in the Appendix A. $N(\pi)$ for negative values of π can also be calculated and fitted, but they are not used in our calculation. In other words, we did not assume that the number of the stars with negative parallaxes is zero, we simply did not use this information because it is not necessary. The fact that this method does not produce any bias is tested in Sect. 4.3.

4.2. Monte Carlo simulation to test the Lucy inversion method

In order to test the reliability of the inversion method, we performed Monte Carlo simulations to determine whether we can recover the original function after deconvolution. We created datasets with randomly distributed particles. Then we convolved this distribution with a Gaussian. We applied Lucy's deconvolution method to the dataset to determine whether we can recreate the original distribution. The results are shown in Fig. 3. We conclude that regardless of the original distribution, we can accurately recover the original data up to 50 kpc or more, which is satisfying to study the Milky Way. We also studied the dependence of the method on the parallax error. We used various values of the average parallax error in Eq. (3) from the interval [0.05, 0.4] mas, which are the most common values for the average parallax error in our data. In Fig. 4 we plot the result, which shows that even though the precision of the method depends on the parallax error, we obtain a satisfying result up to 20 kpc even in the worst case with the highest parallax error.

4.3. Application to full-sky Gaia-DR2 data

We divided the data into bins of Galactic longitude ℓ, Galactic latitude b, and apparent magnitude m. For the values of b we made bins of length 2° and corresponding ℓ in bins of $5^\circ / \cos(b)$.

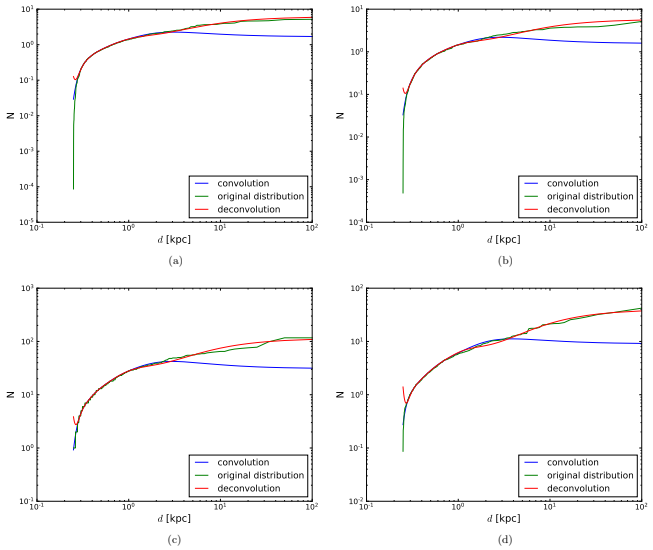

Fig. 3. Monte Carlo simulation of deconvolution. We recover random distributions, convolved with a Gaussian. (*a*) Gamma distribution; (*b*) exponential distribution; (*c*) geometric distribution; (*d*) logarithmic distribution.

We divided each of the lines of sight in magnitude, binned with size $\Delta m = 1.0$ between $G = 12$ and $G = 19$. We obtained 29 206 different areas in which we calculated the density independently.

We made use of the fundamental equation of stellar statistics, where the number of stars $N(m)$ of apparent magnitude m is expressed per unit solid angle and per unit magnitude interval (Chandresekhar & Münch 1951),

$$N(m) = \int_0^\infty \rho(r)\Phi(M)r^2 \mathrm{d}r, \quad (4)$$

where we substitute

$$r(m) = (1/\pi) = 10^{(m-M+5-A_G(1/\pi))/5}, \quad (5)$$

which yields for the density

$$\rho(1/\pi) = \frac{N(\pi)\pi^4}{\Delta\pi\omega \int_{M_{G,\mathrm{low\ lim}}}^{M_{G,\mathrm{low\ lim}}+1} \mathrm{d}M_G \Phi(M_G)}, \quad (6)$$

$$M_{G,\mathrm{low\ lim}} = m_{G,\mathrm{low\ lim}} - 5\log_{10}(1/\pi) - 10 - A_G(1/\pi), \quad (7)$$

where ω is the covered angular surface (10 degrees^2 in our case), $\Delta\pi$ is the parallax interval (0.01 mas in our case), which must be added in the equation because we did not use the unit parallax, $\Phi(M_G)$ is the luminosity function in the G filter, $m_{G,\mathrm{low\ lim}}$ is the limiting maximum apparent magnitude, and $A_G(r)$ is the extinction, as a function of distance.

After this, we calculated the weighted mean density for all seven ranges of magnitude in each line of sight. Then we transformed this into cylindrical coordinates and made bins of Galactocentric radius R of length 0.5 kpc, in Galactic height z of 0.1 kpc and in azimuth of 30°. We define the azimuthal angle ϕ to be measured from the centre-Sun-anticentre direction towards the Galactic rotation, going from 0° to 360°. We interpolated the missing bins with *NearestNDInterpolator* from the python *SciPy* package, which uses nearest-neighbour interpolation in N dimensions. We plot the resulting density maps in Figs. 5 and 6. In Fig. 5 we plot the density in cylindrical coordinates as a function of Galactic radius R for different azimuths. We do not plot the results for azimuths $90° < \phi < 270°$ because in this area the extinction is significant and we observe stars farther than the Galactic centre for which the errors are too large, therefore we

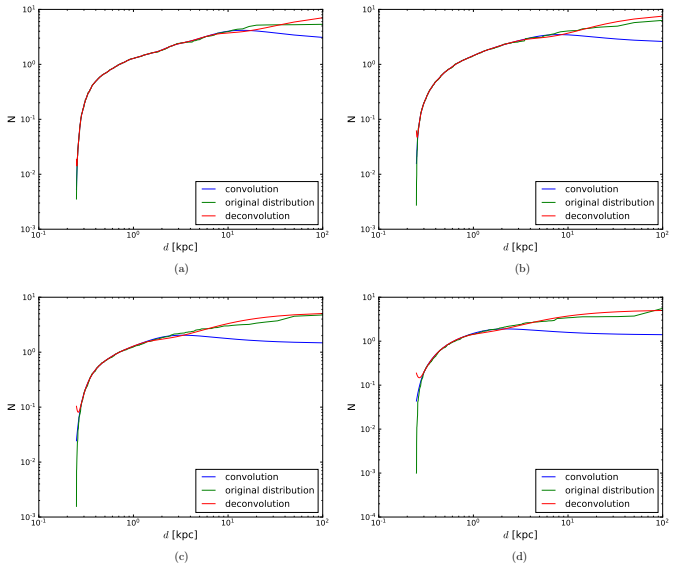

Fig. 4. Monte Carlo simulation of deconvolution. In all cases we recover a gamma distribution convolved with a Gaussian, varying the average error of parallax. (*a*) $\sigma_\pi = 0.05$ mas; (*b*) $\sigma_\pi = 0.1$ mas; (*c*) $\sigma_\pi = 0.25$ mas; (*d*) $\sigma_\pi = 0.4$ mas.

cannot see any structure in density. However, we can see even by eye that a northern warp is present in the azimuths $60° < \phi < 90°$ and a southern warp in the azimuths $270° < \phi < 300°$. Another structure that can be seen from the plots is the flaring of the disc. We analyse these structures below. In Figs. 6a–c we plot the density map in Cartesian coordinates, and in Fig. 6d we plot the density in cylindrical coordinates, integrated through all ranges of azimuths, except for the areas that were excluded from the analysis. The Cartesian coordinates are defined such that $X_\odot = 8.4$ kpc. In these plots we note a flat disc with some fluctuations in density, but no apparent features. However, some slights overdensities both above and below the Galactic plane are visible. The features above the plane are present only in Figs. 6b–c, but not in Fig. 6d, which suggests that it might be a contamination. The feature below the Galactic plane is present in all the three plots. As the direction of these overdensities is towards the Magellanic Clouds, it might be an effect of the Milky Way pulling stars out of Magellanic Clouds, as suggested by Anders et al. (2019). Another possible explanation for these overdensities is the finger of God artefact, which is caused by the foreground dust clouds and causes elongated overdensities that point to the Sun. This artefact has previously been seen in *Gaia* data, as shown in the *Gaia* DR2 documentation[1].

4.4. Zero-point correction in parallaxes

So far, we did not consider any zero-point bias in parallaxes. Lindegren et al. (2018) found a global mean offset of −0.029 mas, meaning that *Gaia* DR2 parallaxes are lower than the true value. We repeated our calculations with this correction and present the results in Fig. 7, where we chose some of the lines of sight to show the comparison. We find that these results are very similar to our original results, and this correction brings a negligible effect. We also tried a value of −0.046 mas, found by Riess et al. (2018). In Fig. 7 we show that the difference between the different zero-point values is very small, therefore we only use the value of −0.029 mas in the further calculations.

[1] https://gea.esac.esa.int/archive/documentation/GDR2/Data_analysis/chap_cu8par/sec_cu8par_validation/ssec_cu8par_validation_additional-validation.html

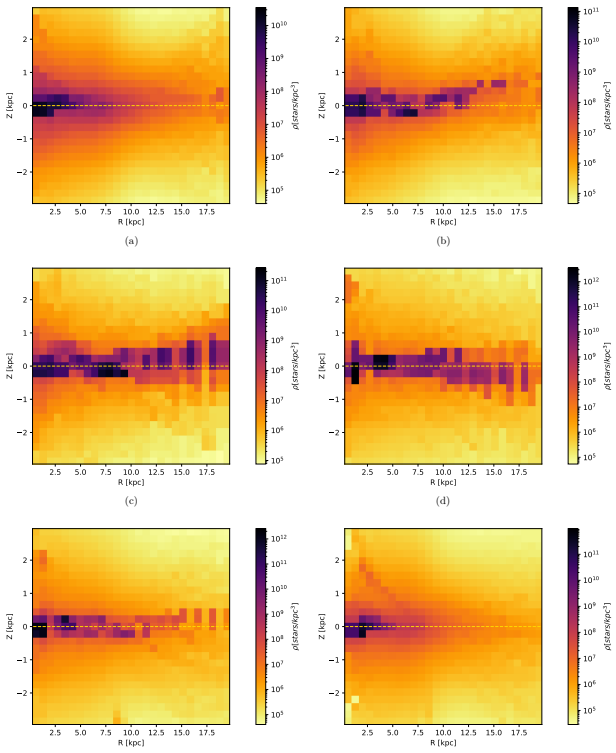

Fig. 5. Density maps for various azimuths between 0° and 360°. (*a*) $0° < \phi < 30°$; (*b*) $30° < \phi < 60°$; (*c*) $60° < \phi < 90°$; (*d*) $270° < \phi < 300°$; (*e*) $300° < \phi < 330°$; (*f*) $330° < \phi < 360°$.

For the analysis of the warp in Sects. 5.5 and 5.6, we repeated the analysis of Sect. 4 with the value of parallax corrected for the zero-point. We find that this brings a small correction to the warp parameters, which we state as the systematic error in the results.

4.5. Error of the extinction

To test how accurate the extinction map is, we analysed the map of Green et al. (2015) using the function `query`, which returns the standard deviation σ_G for a given line of sight. We calculate

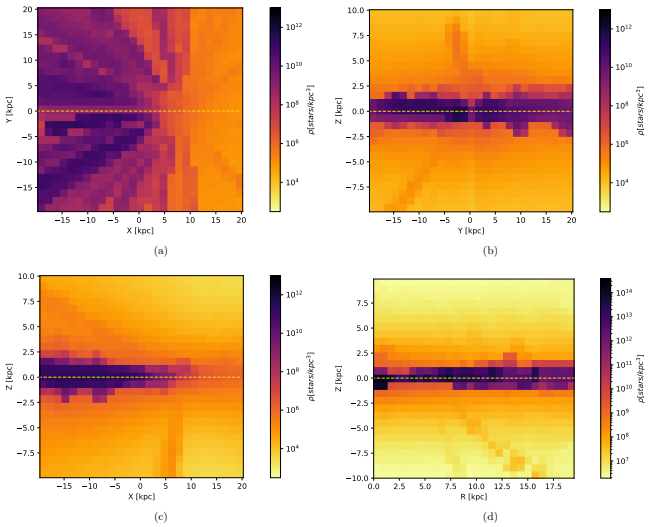

Fig. 6. Density maps.

a new extinction as

$$A_G^*(r) = A_G(r) + f * \sigma_G(r), \quad (8)$$

where A_G is the extinction given by the map, r is the distance, and f is a factor chosen randomly from a Gaussian distribution with $\mu = 0$ and $\sigma = 1$.

In Fig. 8 we show the relative error of the density $\delta = (\rho(A_G) - \rho(A_G^*))/\rho(A_G)$. For all lines of sight that we tested, the difference is negligible, except for the area in the centre of the Galaxy, which we know is problematic. However, in the outer disc, where we carried out our analysis, the extinction is determined quite accurately. We must of course take into account that we used the map of Bovy et al. (2016), which combines different maps and is less accurate and therefore can give different results than Green et al. (2015) in some areas. Moreover, we estimated only the statistical error of the extinction, but we recall that we do not have information about the systematic error of the extinction map. However, for our purposes, the extinction map gives satisfying results in the area we analysed. The stellar warp has been studied using star counts by many other authors (López-Corredoira et al. 2002a; Reylé et al. 2009; Amôres et al. 2017, and others), therefore this method is most likely not especially flawed.

4.6. Thick-disc areas

In the previous analysis we considered only the thin-disc population because the luminosity function presented in Sect. 3 is calculated in thin-disc regions. However, we can also analyse high Galactic heights, where the influence of the thick disc is significant. To test the importance of the change in luminosity function, we tested the density calculations with a tentative thick-disc luminosity function that reduces the number of bright stars. We used the source table of Wainscoat et al. (1992), who give the ratio of all the components of the Galaxy for all stellar classes. Based on this comparison, we altered our luminosity function to construct a theoretical thick-disc luminosity function, as depicted in Fig. 9. Then we repeated our calculation with this new luminosity function. In Fig. 10 we show the result for some lines of sight. In the area where we carried out the analysis, the difference between the two approaches is clearly visible starting at ~20 kpc. Our density analysis is made in the area below 20 kpc, where the difference between the two densities is negligible. We note that this difference changes with line of sight, which is caused by the extinction. In the areas where the extinction is significant, the difference between densities derived from thin- and thick-disc luminosity functions is more important, but

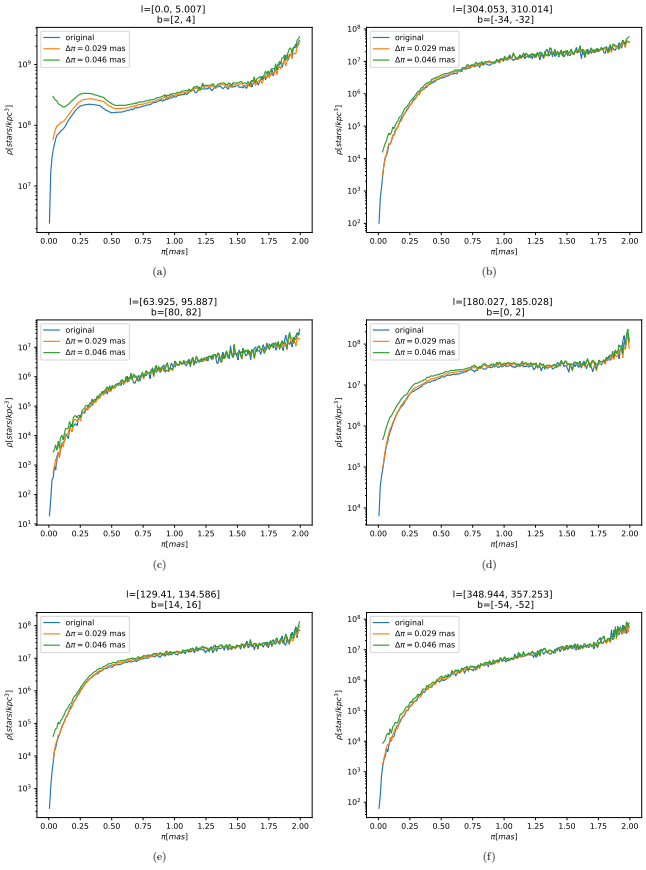

Fig. 7. Comparison of densities for various lines of sight. Orange and green curves represent the density including the zero-point correction of the parallax, and the blue curve shows the density without this correction.

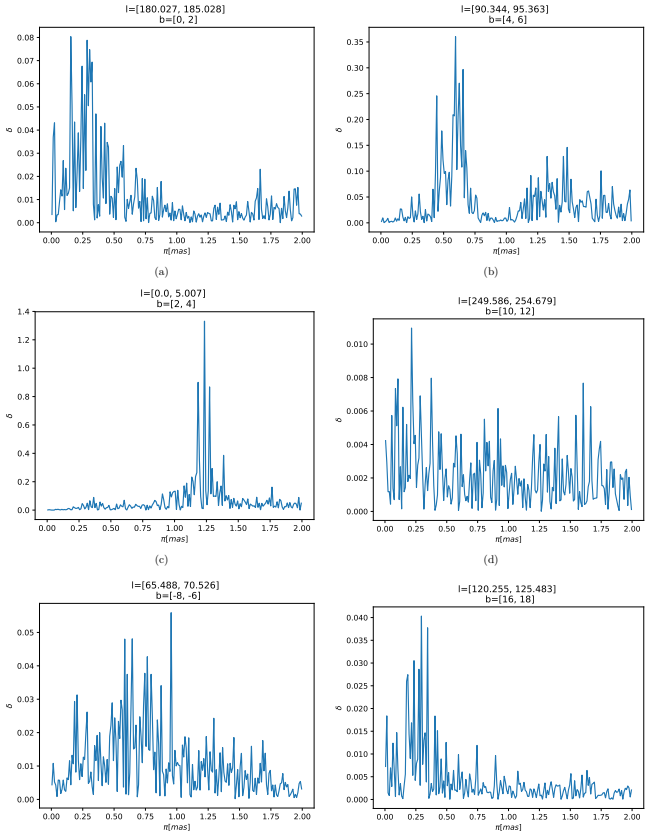

Fig. 8. Relative error $\delta = (\rho(A_G) - \rho(A_G^*))/\rho(A_G)$ of the density calculated including the standard deviation of the extinction.

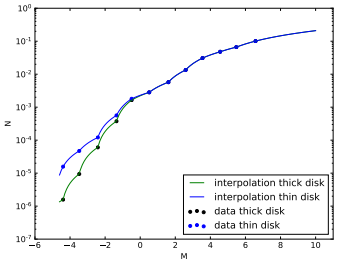

Fig. 9. Comparison of luminosity functions for the thin and thick disc.

these areas are removed from our analysis. Therefore our maps are also valid for thick-disc areas.

5. Analysis of the density maps

5.1. Comparison with the maps of Anders et al. (2019)

Recently, similar maps were created by Anders et al. (2019). In their analysis, they used the code `StarHorse`, originally developed to determine stellar parameters and distances for spectroscopic surveys (Queiroz et al. 2018). This code compares observed quantities to a number of stellar evolutionary models. It finds the posterior probability over a grid of stellar models, distances, and extinctions. To do this, it needs many priors, including stellar initial mass function, density laws for main Milky Way components, and the broad metallicity and age of those components. Afterwards, the authors applied various criteria on their sample to choose only accurate results.

When we compare our results, we can observe similar structures, except in the area of the Galactic bulge, where our data are not reliable and the data of Anders et al. (2019) are much more accurate. However, because data with high errors in parallax were removed, Anders et al. (2019) were unable to reach such high distances, which are necessary to study features of the outer disc such as the flare or the warp. Another advantage of our method is that we did not assume any priors about the Milky Way. Furthermore, our density maps are a representation of the complete number of stars per unit volume up to some given absolute magnitude, taking into account the luminosity function, whereas Anders et al. (2019) gave the stars observed by *Gaia*, a much larger number in the solar neighbourhood, thus not useful to quantify absolute trends in the density distribution. Nevertheless, we consider the results of Anders et al. (2019) very useful because they improve the accuracy of the data significantly and can be used to study parts of Milky Way where our data fail.

5.2. Cut-off in the Milky Way

There has been some discussion about the cut-off in the Milky Way. Some authors have reported to find a cut-off starting at about 14 kpc from the Galactic centre (Robin et al. 1992, 2003; Minniti et al. 2011). However, Carraro et al. (2014) argued that these finding are erroneous either because the dataset is biased or because the warp and flare is confused with the cut-off. The absence of the cut-off has been confirmed by several studies (López-Corredoira & Molgó 2014; Sale et al. 2010; Brand & Wouterloot 2007). Our results show that there is no cut-off in the Galactic disc, at least up to 20 kpc.

5.3. Stellar density in the solar neighbourhood

We define the solar neighbourhood as the area where $7.5\,\mathrm{kpc} < R < 8.5\,\mathrm{kpc}$ and $|z| < 0.05\,\mathrm{kpc}$ and calculate the average density in this area. We find $\rho_\odot = 0.064\,\mathrm{stars\,pc^{-3}}$, which is close to other values in the literature, for example $0.03\,\mathrm{stars\,pc^{-3}}$ obtained by Chang et al. (2011), who used a three-component model to fit data from 2MASS. Eaton et al. (1984) found $\rho_\odot = 0.056\,\mathrm{stars\,pc^{-3}}$, which is lower than our result, but this value is influenced by the range of the luminosity function, which is where the difference between the values stems from. In our case, we measured stars with $M_G < 10$.

5.4. Exponential fits of the density

To describe the radial volume mass density distribution in the Galactic equatorial plane, we used a modified exponential disc with a deficit of stars in the inner in-plane region adopted from López-Corredoira et al. (2004) in the following form:

$$\rho(R) = \rho_0 \times \exp\left(\frac{R_\odot}{h_r} + \frac{h_{r,\mathrm{hole}}}{R_\odot}\right) \times \exp\left(-\frac{R}{h_r} - \frac{h_{r,\mathrm{hole}}}{R}\right), \quad (9)$$

where h_r is the scale length, $h_{r,\mathrm{hole}} = 3.74\,\mathrm{kpc}$ is the scale of the hole, $R_\odot$ is the Galactocentric distance of the Sun, and R is the Galactocentric distance. We neglected the contribution of the thick disc and analysed only the thin disc. We divided the Galactic equatorial plane into three regions according to the Galactic azimuth $[-45°, -15°], [-15°, 15°], [15°, 45°]$. We focused on the Galactic equatorial plane, therefore we considered stars in the close vicinity of the plane with a vertical distance $|z| < 0.2\,\mathrm{kpc}$ and $R > 6\,\mathrm{kpc}$. We fitted the density for various azimuths with the corresponding exponential fits based on Eq. (9). The scale length slightly depends on the Galactic azimuth; it reaches the highest value for the Sun-anticentre direction and $\phi = +30°$, $h_r = 2.78 \pm 0.13\,\mathrm{kpc}$, and $h_r = 2.29 \pm 0.21\,\mathrm{kpc}$. On the other hand, the lowest value of the scale length is $h_r = 1.88 \pm 0.12\,\mathrm{kpc}$ for $\phi = -30°$. This results in an average of $h_r = 2.29 \pm 0.08\,\mathrm{kpc}$, with small dependence on the azimuth. We can compare the results with published papers. López-Corredoira & Molgó (2014) used SDSS-SEGUE (Sloan Digital Sky Survey – Sloan Extension for Galactic Understanding and Exploration) data to investigate the density distribution in the Galactic disc. They obtained the scale length for the thick and for the thin disc, $h_{r,\mathrm{thin}} = 2.1\,\mathrm{kpc}$ and $h_{r,\mathrm{thick}} = 2.5\,\mathrm{kpc}$ for the azimuth $\phi \leq 30°$, which is consistent with our results. Li et al. (2019) studied OB stars using *Gaia* DR2 data and the derived scale length of the Galactic disc, and found $h_r = 2.10 \pm 0.1\,\mathrm{kpc}$, which is in accordance with our results.

We also plot the dependence of the density in the Galactic equatorial plane on azimuth for various values of Galactocentric distance in Fig. 11. The density is slightly dependent on the Galactic azimuth for all radii, but this dependence is very small. An analysis of the scale height and its corresponding flare will be given in a forthcoming paper (Nagy et al., in prep.).

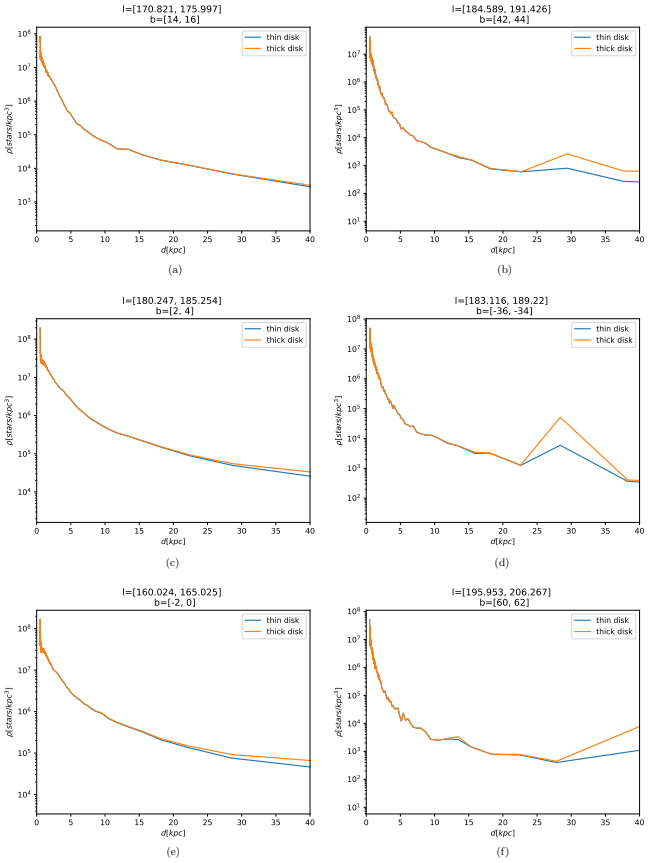

Fig. 10. Densities for different lines of sight. Blue curves are densities calculated with the thin-disc luminosity function. Orange curves are densities calculated with the thick-disc luminosity function.

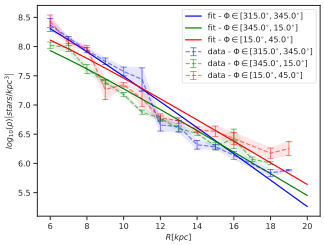

Fig. 11. Dependence of the density on azimuth near the centre-Sun-anticentre direction for various values of Galactocentric distance. The data points are obtained as weighted mean in bins of size 1 kpc in R and 0.4 kpc in $|z|$. Only bins with a number of points $N \geq 50$ points are plotted.

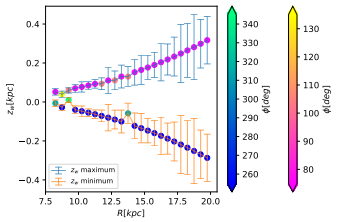

Fig. 12. Minimum and maximum average elevation of the plane as a function of radius. The warp fit is based on Eq. (11), and the error bars represent the uncertainty in the distance in the Lucy method.

5.5. Warp

The density maps (Fig. 5) directly show a northern warp in azimuth 90° and southern warp in azimuth 270°. Here, we analyse these structures in greater detail. We removed the azimuths $150° < \phi < 240°$ and radii $R < 6$ kpc from our analysis because these data have low quality and influence the results negatively.

We calculated the average elevation above the plane z_w as

$$z_w = \frac{\int_{z_{\min}}^{z_{\max}} \rho z \mathrm{d}z}{\int_{z_{\min}}^{z_{\max}} \rho \mathrm{d}z} \tag{10}$$

and fit this quantity with models of the warp. In our first approach, we used the model by López-Corredoira et al. (2002a, Eq. (20)),

$$z_w = [C_w R(\mathrm{pc})^{\epsilon_w} \sin(\phi - \phi_w) + 17]\,\mathrm{pc}. \tag{11}$$

The 17 pc term compensates for the elevation of the Sun above the plane (Karim & Mamajek 2017). C_w, ϵ_w , and ϕ_w are free parameters of the model, which were fitted to our data. An asymmetry is observed between the northern and southern warp for the gas (Voskes & Butler Burton 2006) and for the young population (Amôres et al. 2017), therefore we also explore the northern and southern warp separately here. The fit of our data yields maximum amplitudes $z_w = 0.317$ kpc for the northern and $z_w = -0.287$ kpc for the southern warp, both at a distance $R = [19.5, 20]$ kpc, revealing a small asymmetry between the north and south. For the fit, we used the function *curve fit* from the python *SciPy* package, which uses non-linear least squares to fit a function to data. The parameters of the best fit for this model for the whole dataset are

$$\begin{aligned} C_w &= 1.17 \times 10^{-8}\,\mathrm{pc} \pm 1.34 \times 10^{-9}\,\mathrm{pc(stat.)} \\ &\quad - 2.9 \times 10^{-10}\,\mathrm{pc(syst.)}, \\ \epsilon_w &= 2.42 \pm 0.76(\mathrm{stat.}) + 0.129(\mathrm{syst.}), \\ \phi_w &= -9.31° \pm 7.37°(\mathrm{stat.}) + 4.48°(\mathrm{syst.}). \end{aligned} \tag{12}$$

Here, the error of c_w stands for the error of the amplitude alone, without the variations of ϵ_w and ϕ_w. The plot of the results is shown in Fig. 12, where we show the comparison of minimum and maximum value of $z_w(R)$. The average elevation of the plane is highest for azimuths [60°, 90°] and [90°, 120°] in most of the cases, whereas the minimum is reached for azimuths [240°, 270°] in most of the cases. A slight asymmetry between the northern and southern warp is also clearly visible.

Another approach that we used is based on the work of Levine et al. (2006), who studied the vertical structure of the outer disc of the Milky Way by tracing neutral hydrogen gas. They analysed the Galactic warp using a Lomb periodogram analysis. They concluded that the first two Fourier modes are the strongest modes. We use the expression derived by Levine et al. (2006) in the following form:

$$z_w = z_0 + z_1 \cdot \sin(\phi - \phi_1) + z_2 \cdot \sin(2\phi - \phi_2), \tag{13}$$

where z_w is the average elevation above the plane, z_i for $i \in (0, 1, 2)$ are the amplitudes of the warp, ϕ_i for $i \in (1, 2)$ are the phases. The dependence of the amplitudes of the warp on the Galactocentric distances is

$$z_i = k_0 + k_1 \cdot (R - R_k) + k_2 \cdot (R - R_k)^2 \text{ for } i = 0, 1, 2, \tag{14}$$

where k_i and R_k are free parameters of the fit. We fitted our data with Eqs. (13) and (14) for various values of Galactocentric distances $R < 20$ kpc. We plot the data and the fits for $R \in (13.25, 16.25, 19.25)$ kpc in Fig. 13. Figure 14 shows the azimuth of the maximum and minimum of the Galactic warp as a function of the Galactocentric distance. In our analysis, we excluded data for the Galactic azimuths $\phi \in (120°, 240°)$ because of the high error values in our data. We used a 10° binning in azimuth. Figure 13 shows that the data for $250° < \phi < 270°$ are somewhat noisy, which can be caused by problems with extinction or with the Lucy method in a particular line of sight. Therefore we tested a fit without these points, which turned out to produce an insignificant difference. For instance, the minimum amplitude obtained without these points changed by 10% in the worse case, and the maximum amplitude changed by 2%.

Figures 13 and 14 clearly show that the warp is present in our analysis. The azimuth of the maximum of the warp (the northern warp) is an increasing function of the Galactocentric distance ($52° < \phi < 56°$). On the other hand, the azimuth of the minimum of the warp is in $312° < \phi < 324°$ and corresponds to the southern warp. The strongest deviation of the average elevation of the Galactic plane from the Galactic equatorial plane

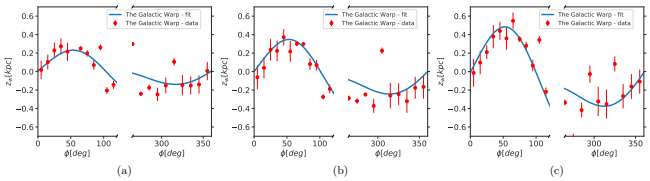

Fig. 13. Average elevation of the plane as a function of the Galactic azimuth for various values of the Galactocentric distance. Red markers represent values of binned data, and the blue line represents a fit to the data. (*a*) R = 13.25 kpc; (*b*) R = 16.25 kpc; (*c*) R = 19.25 kpc.

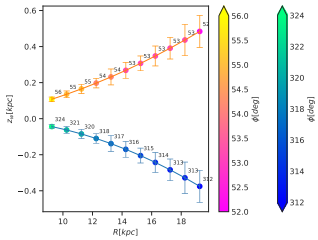

Fig. 14. Minimum and maximum of the average elevation of the plane as a function of Galactocentric distance. The warp fit is based on Eq. (13). The colours code the azimuth of the minimum and maximum of the warp fit, and the error bars represent the uncertainty on the distance in the Lucy method.

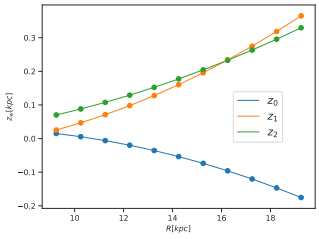

Fig. 15. Changes of the amplitudes of the Galactic warp fit according to Eqs. (13) and (14).

rises with Galactocentric distance. The highest amplitude of the northern and southern warp is z_w = 0.48 kpc and z_w = −0.38 kpc, respectively. An asymmetrical warp is clearly present.

The value of the line of nodes from the fit is $\phi_0 = -1.18°$. We plot the changes in amplitude of the Galactic warp fit [Eq. (14)] with Galactocentric distance in Fig. 15.

Similar results were obtained by Li et al. (2019), who used OB stars of *Gaia* DR2 to measure the warp. They fit their data with a sinusoidal function similar to ours and obtained a warp with a mean magnitude up to z = 0.5 kpc. However, they did not account for the asymmetry of the warp, therefore they found the same result for the north and south. Chen et al. (2019) used Cepheids from the WISE (Wide-field Infrared Survey Explorer) catalogue and traced the warp up to R = 20 kpc. Their results show a warp extended up to $|z|$ = 1.5 kpc, which we cannot confirm using the whole population. Poggio et al. (2018) studied the kinematics of the Milky Way using *Gaia* DR2 and found the warp up to 7 kpc from the Sun. This agrees with our results, but we show that the warp extends to a higher radius, at least up to 20 kpc. In Fig. 16, we compare the maximum amplitudes of our model with other works. We obtain a very low amplitude, especially in comparison with Cepheids. On the other hand, the closest result is that of Chen et al. (2019), who used OB stars from *Gaia* DR2. This significant difference between the amplitude of various populations is in favour of the formation of the warp through accretion onto the disc (López-Corredoira et al. 2002b), which causes the gas and young stars to warp more strongly than the remaining population.

Momany et al. (2006) studied the stellar warp using 2MASS red clump and red giant stars, selected at fixed heliocentric distances of 3, 7, and 17 kpc. They found a rather symmetric warp and argued that a symmetric warp can be observed as asymmetric for two reasons. First, the Sun is not located at the line of nodes, and second, the northern warp is located behind the Norma-Cygnus arm, which can cause variation in extinction that can produce an apparent asymmetric warp. As for the first point, the position of Sun on the line of nodes is a problem when we observe the warp at a fixed distance. However, we have a 3D distribution, which ensures that the position from which we look does not influence how we perceive the warp. As for the second remark, as we showed in Sect. 2 that the extinction is determined quite accurately by the extinction map of Green et al. (2015). However, some variations might influence the final shape of the warp and may not have been taken into account, therefore we need to keep that in mind when we interpret our results.

5.6. Young population

In this section, we apply the previous analysis to the young population. To do so, we only chose stars brighter than an absolute magnitude $M_G = -2$ (see the luminosity function in Fig. 17)

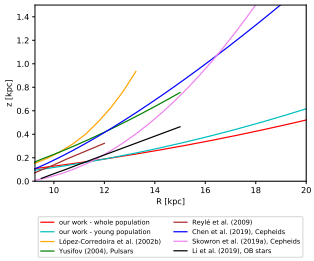

Fig. 16. Comparison of maximum amplitudes of our model (based on Eq. (13)) with other works.

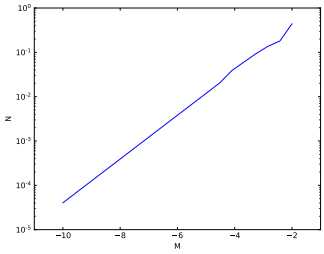

Fig. 17. Luminosity function used in the Eq. (6) for the analysis of the young population.

and repeated all the steps as described in Sect. 4.3. Then we produced density maps and analysed the scale length and the warp of this population using methods from Sects. 5.4 and 5.5.

The exponential fits of the density for the young population yield $h_r = 2.5 \pm 0.22$ kpc for $\phi = 30°$, $h_r = 1.92 \pm 0.15$ kpc for $\phi = 0°$, and $h_r = 2.04 \pm 0.15$ kpc for $\phi = 30°$, which is similar to the whole population. This results in $h_r = 2.09 \pm 0.09$ kpc on average. The variation with azimuth is still insignificant, as in the case of the entire population. Figure 18 shows that the variation of density with azimuth is also negligible in the case of the young population.

For the warp, as previously, we removed the azimuths $150° < \phi < 240°$ from the analysis. The fit of Eq. (11) to the young population yields

$$\begin{aligned} C_w &= 4.85 \times 10^{-14}\ \text{pc} \pm 6.33 \times 10^{-15}\ \text{pc(stat.)} \\ &\quad + 5.4 \times 10^{-15}\ \text{pc(syst.)}, \\ \epsilon_w &= 3.69 \pm 1.19\text{(stat.)} - 0.373\text{(syst.)}, \\ \phi_w &= -1.64° \pm 8.85°\text{(stat.)} - 2.803°\text{(syst.)}. \end{aligned} \tag{15}$$

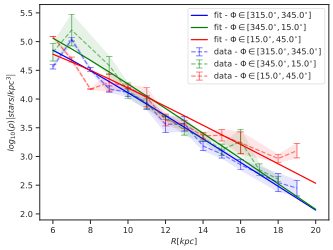

Fig. 18. Same as Fig. 11, but the young population alone is considered.

We also repeated the analysis with the approach using Eq. (13). Figure 19 presents the Galactic warp of the young stellar population for various Galactocentric distances, and Fig. 20 shows the amplitudes of the fits of the Galactic warp and the azimuth of the maximum and minimum. In this case, the warp of the young stellar population is stronger than the case considering all stars in our dataset. The azimuth of the maximum of the northern warp is an increasing function of the Galactocentric distance ($50° < \phi < 54°$), and the azimuth of the minimum of the warp is in $265° < \phi < 315°$. The highest amplitude of the northern and the southern warp is $z_w = 0.57$ kpc and $z_w = -0.5$ kpc, respectively. For the line of nodes, we find $\phi_0 = -6.56°$, which agrees with the whole population.

Chen et al. (2019) used Cepheids from the WISE survey and a number of optical surveys to measure the warp, and Skowron et al. (2019a) used Cepheids from the OGLE catalogue supplemented by other surveys. Chen et al. (2019) obtained a rather symmetric warp with an amplitude of about 1.5 kpc in $R = 20$ kpc. Skowron et al. (2019a) obtained a similar result with an amplitude 0.74 kpc in $R = 15$ kpc. These values are much higher than our findings, which is probably due to differences in the population: our young population is older than the Cepheids. In Fig. 21 we plot the variation of the line of nodes with radius for the whole and the young population, compared with other works. We use two different methods to plot the line of nodes for our work. First, we plot the angle ϕ_w for Eq. (12). Another method is to use the Eq. (11) to find the value of the angle ϕ when $z_w = 0$. We would expect that our young population lies between the total population and the young Cepheids. This is true only for $R > 12$ kpc. At shorter distances, the warp is not very strong and is more difficult to detect, therefore the error bars are larger in this area. Moreover, the error bars of the young populations are very large because of the lower number of stars in the sample combined with possible problems in determining extinction. For these reasons, the value of the line of nodes for $R < 12$ kpc is rather unreliable.

6. Conclusions

We produced density maps from *Gaia* DR2 data and analysed them to study the Galactic warp. The density maps directly show a northern warp in the azimuths $60° < \phi < 90°$ and a southern warp in the azimuths $270° < \phi < 300°$. Our maps reach a Galactocentric

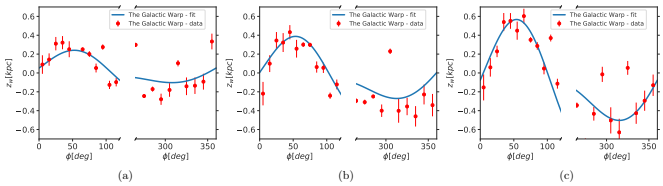

Fig. 19. Dataset containing a young population of stars. The average elevation of the plane as a function of the Galactic azimuth for various values of the Galactocentric distance. Red markers represent values of binned data, and the blue line represents a fit to the data. (*a*) $R = 13.25$ kpc; (*b*) $R = 16.25$ kpc; (*c*) $R = 19.25$ kpc.

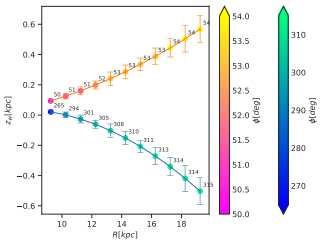

Fig. 20. Minimum and maximum of the average elevation of the plane as a function of the Galactocentric distance. The warp fit is based on Eq. (13). The colours code the azimuth of the minimum and the maximum of the warp fit. The dataset containing a young population of stars is considered, and the error bars represent the uncertainty on the distance in the Lucy method.

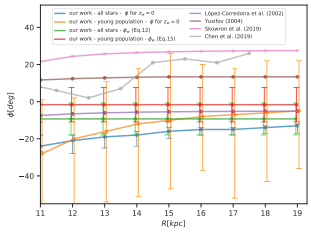

Fig. 21. Comparison of line of nodes for our model (based on Eq. (11)) with other works. We use two different methods to plot the line of nodes for our work. First, we plot the angle ϕ_p for Eq. (12). Another method is to use the Eq. (11) to find the value of the angle ϕ when $z_w = 0$.

radius of 20 kpc, and we note that up to this distance, the density decreases exponentially and we do not observe a cut-off. Another feature in the density maps is a Galactic flare, that is, an increase in scale height towards the outer Galaxy. The analysis of the flare will be given in a forthcoming paper (Nagy et al., in prep.). We used the maps to calculate the scale length, where we find $h_r = 2.29 \pm 0.08$ kpc, with a small dependence of h_r from the Galactic azimuth. The lowest value of h_r that we found is 1.88 ± 0.12 kpc for $\phi \approx \pm -30°$ and the highest value is 2.78 ± 0.13 kpc for the Sun-anticentre direction and 2.29 ± 0.21 $\phi \approx \pm 30°$.

From our maps, we calculated the average elevation of the plane and fitted it with different warp models. We fitted the northern and southern warp separately with a simple sinusoidal model, and we found a small asymmetry: the northern warp reaches an amplitude 0.317 kpc for the azimuth $60° < \phi < 90°$ and the southern warp reaches -0.287 kpc for the azimuth $240° < \phi < 270°$, both at $R = [19.5, 20.0]$ kpc. Then we fitted the warp with a model combining two sinusoids to detect the asymmetry without assuming its existence, and we found values of amplitude ~ 0.5 for the northern and ~ -0.4 for the southern warp both at $R = [19.5, 20.0]$ kpc, revealing the asymmetry found with the previous approach. The azimuths of the warp maximum and minimum for this model are $52° < \phi < 56°$ and $312° < \phi < 324°$, respectively. In terms of Galactocentric radius, we find that warp starts to manifest itself from about 12 kpc and extends at least up to 20 kpc. We repeated this analysis on the young population, where we find that it follows the result for the whole population, but reaches a higher amplitude of warp and similar values of scale height. The comparison of our amplitude of the warp with other works showed that we obtain a significantly lower amplitude than an analysis carried out with very young stars such as Cepheids. This supports the formation of the warp through accretion onto the disc (López-Corredoira et al. 2002b).

A future analysis of the next *Gaia* data release combined with the deconvolution method based on Lucy's method of inversion, as described in Sect. 4.1, will allow us to explore distances larger than 20 kpc. The future data release will provide a much deeper magnitude limit and much lower parallax errors, which will allow us to extend the range of Galactocentric distances and study the morphology of the disc and of the stellar halo at very large distances.

Acknowledgements. We thank the anonymous referee for helpful comments, which improved this paper, and Astrid Peter (language editor of A&A) for proof-reading of the text. ZC and MLC were supported by the Grant

PGC-2018-102249-B-100 of the Spanish Ministry of Economy and Competitiveness (MINECO). RN was supported by the Scientific Grant Agency VEGA No. 1/0911/17. This work made use of the IAC Supercomputing facility HTCondor (http://research.cs.wisc.edu/htcondor/), partly financed by the Ministry of Economy and Competitiveness with FEDER funds, code IACA13-3E-2493. This work has made use of data from the European Space Agency (ESA) mission *Gaia* (https://www.cosmos.esa.int/gaia), processed by the *Gaia* Data Processing and Analysis Consortium (DPAC, https://www.cosmos.esa.int/web/gaia/dpac/consortium). Funding for the DPAC has been provided by national institutions, in particular the institutions participating in the *Gaia* Multilateral Agreement. The reduced catalogue of *Gaia* with $m_G < 19$ was produced by Pedro Alonso Palicio.

References

Amôres, E. B., Robin, A. C., & Reylé, C. 2017, A&A, 602, A67
Anders, F., Khalatyan, A., Chiappini, C., et al. 2019, A&A, 628, A94
Arenou, F., Luri, X., Babusiaux, C., et al. 2018, A&A, 616, A17
Bahcall, J. N. 1986, ARA&A, 24, 577
Bahcall, J. N., & Soneira, R. M. 1980, ApJS, 44, 73
Balázs, L. G. 1995, Inverse Prob., 11, 731
Battaner, E., Florido, E., & Sanchez-Saavedra, M. L. 1990, A&A, 236, 1
Bovy, J., Rix, H.-W., Liu, C., et al. 2012, ApJ, 753, 148
Bovy, J., Rix, H.-W., Green, G. M., Schlafly, E. F., & Finkbeiner, D. P. 2016, ApJ, 818, 130
Brand, J., & Wouterloot, J. G. A. 2007, A&A, 464, 909
Carney, B. W., & Seitzer, P. 1993, AJ, 105, 2127
Carraro, G. 2014, in Setting the Scene for Gaia and LAMOST, eds. S. Feltzing, G. Zhao, N. A. Walton, & P. Whitelock, IAU Symp., 298, 7
Chandrasekhar, S., & Münch, G. 1951, ApJ, 113, 150
Chang, C.-K., Ko, C.-M., & Peng, T.-H. 2011, ApJ, 740, 34
Chen, B., Stoughton, C., Smith, J. A., et al. 2001, ApJ, 553, 184
Chen, X., Wang, S., Deng, L., et al. 2019, Nat. Astron., 3, 320
Craig, I. J. D., & Brown, J. C. 1986, Inverse Problems in Astronomy. A Guide to Inversion Strategies for Remotely Sensed Data (Bristol, UK: Adam Hilger)
Debattista, V. P., & Sellwood, J. A. 1999, ApJ, 513, L107
Dehnen, W. 1998, AJ, 115, 2384
Drimmel, R., Cabrera-Lavers, A., & López-Corredoira, M. 2003, A&A, 409, 205
Eaton, N., Adams, D. J., & Giles, A. B. 1984, MNRAS, 208, 241
Gaia Collaboration (Prusti, T., et al.) 2016, A&A, 595, A1
Gaia Collaboration (Brown, A.G.A., et al.) 2018, A&A, 616, A1
Green, G. M., Schlafly, E. F., Finkbeiner, D. P., et al. 2015, ApJ, 810, 25
Green, G. M., Schlafly, E. F., Finkbeiner, D., et al. 2018, MNRAS, 478, 651
Hendy, Y. H. M. 2018, NRIAG J. Astron. Geophys., 7, 180
Jurić, M., Ivezić, Ž., Brooks, A., et al. 2008, ApJ, 673, 864
Karim, M. T., & Mamajek, E. E. 2017, MNRAS, 465, 472
Kerr, F. J. 1957, AJ, 62, 93
Kim, J. H., Peirani, S., Kim, S., et al. 2014, ApJ, 789, 90
Levine, E. S., Blitz, L., & Heiles, C. 2006, ApJ, 643, 881
Li, C., Zhao, G., Jia, Y., et al. 2019, ApJ, 871, 208
Lindegren, L., Hernández, J., Bombrun, A., et al. 2018, A&A, 616, A2
Liu, C., Xu, Y., Wan, J.-C., et al. 2017, Res. Astron. Astrophys., 17, 096
López-Corredoira, M., & Molgó, J. 2014, A&A, 567, A106
López-Corredoira, M., & Sylos-Labini, F. 2019, A&A, 621, A48
López-Corredoira, M., Hammersley, P. L., Garzón, F., Simonneau, E., & Mahoney, T. J. 2000, MNRAS, 313, 392
López-Corredoira, M., Cabrera-Lavers, A., Garzón, F., & Hammersley, P. L. 2002a, A&A, 394, 883
López-Corredoira, M., Betancort-Rijo, J., & Beckman, J. E. 2002b, A&A, 386, 169
López-Corredoira, M., Cabrera-Lavers, A., Gerhard, O. E., & Garzón, F. 2004, A&A, 421, 953
López-Corredoira, M., Abedi, H., Garzón, F., & Figueras, F. 2014, A&A, 572, A101
López-Corredoira, M., Garzon, F., Wang, H. F., et al. 2020, A&A, 634, A66
Lucy, L. B. 1974, ApJ, 79, 745
Lucy, L.B. 1994, A&A, 289, 983
Luri, X., Brown, A. G. A., Sarro, L. M., et al. 2018, A&A, 616, A9
Majewski, S. R. 1993, ARA&A, 31, 575
Marshall, D. J., Robin, A. C., Reylé, C., Schultheis, M., & Picaud, S. 2006, A&A, 453, 635
Minniti, D., Saito, R. K., Alonso-García, J., Lucas, P. W., & Hempel, M. 2011, ApJ, 733, L43
Momany, Y., Zaggia, S., Gilmore, G., et al. 2006, A&A, 451, 515
Oort, J. H., Kerr, F. J., & Westerhout, G. 1958, MNRAS, 118, 379
Paul, E. R. 1993, The Milky Way Galaxy and Statistical Cosmology, 1890
Poggio, E., Drimmel, R., Lattanzi, M. G., et al. 2018, MNRAS, 481, L21
Queiroz, A. B. A., Anders, F., Santiago, B. X., et al. 2018, MNRAS, 476, 2556
Reylé, C., Marshall, D. J., Robin, A. C., & Schultheis, M. 2009, A&A, 495, 819
Riess, A. G., Casertano, S., Yuan, W., et al. 2018, ApJ, 861, 126
Robin, A. C., Creze, M., & Mohan, V. 1992, ApJ, 400, L25
Robin, A. C., Reylé, C., Derrière, S., & Picaud, S. 2003, A&A, 409, 523
Robin, A. C., Marshall, D. J., Schultheis, M., & Reylé, C. 2012, A&A, 538, A106
Rybizki, J., Demleitner,, M., Fouesneau, M., et al. 2018, PASP, 130,
Sale, S. E., Drew, J. E., Knigge, C., et al. 2010, MNRAS, 402, 713
Schlegel, D. J., Finkbeiner, D. P., & Davis, M. 1998, ApJ, 500, 525
Schönrich, R., & Dehnen, W. 2018, MNRAS, 478, 3809
Skowron, D. M., Skowron, J., Mróz, P., et al. 2019a, Science, 365, 478
Skowron, D. M., Skowron, J., Mróz, P., et al. 2019b, Acta Astron., 69, 305
Stassun, K. G., & Torres, G. 2018, ApJ, 862, 61
Turchin, V. F., Kozlov, V. P., & Malkevich, M. S. 1971, Sov. Phys. Usp., 13, 681
Voskes, T., & Butler Burton, W. 2006, ArXiv e-prints [arXiv:astro-ph/0601653]
Vozoff, K., & Jupp, D. L. B. 1975, Geophys. J. R. Astron. Soc., 42, 977
Wainscoat, R. J., Cohen, M., Volk, K., Walker, H. J., & Schwartz, D. E. 1992, ApJS, 83, 111
Yusifov, I. 2004, in The Magnetized Interstellar Medium, eds. B. Uyaniker, W. Reich, & R. Wielebinski, 165
Zinn, J. C., Pinsonneault, M. H., Huber, D., & Stello, D. 2019, ApJ, 878, 136

Appendix A: Lucy's method for the inversion of Fredholm integral equations of the first kind

The inversion of Fredholm integral equations of the first kind such as Eq. (2) is ill-conditioned. Typical analytical methods for solving these equations (Balázs 1995) cannot achieve a good solution because the kernel is sensitive to the noise of the star counts (Craig & Brown 1986, chapter 5). Because the functions in these equations have a stochastic rather than analytical interpretation, it is to be expected that statistical inversion algorithms are more robust (Turchin et al. 1971; Vozoff & Jupp 1975; Balázs 1995). These statistical methods include the iterative method of Lucy's algorithm (Lucy 1974; Turchin et al. 1971; Balázs 1995; López-Corredoira et al. 2000), which is appropriate here. Its key feature is the interpretation of the kernel as a conditioned probability and the application of Bayes' theorem.

In Eq. (2), $N(\pi)$ is the unknown function, and the kernel is $G(x)$, whose difference x is conditioned to the parallax π'. The inversion is carried out as

$$N(\pi) = \lim_{n\to\infty} N_n(\pi), \tag{A.1}$$

$$N_{n+1}(\pi) = N_n(\pi)\frac{\int_0^\infty \frac{\overline{N}(\pi')}{\overline{N_n}(\pi')} G_{\pi'}(\pi-\pi')\mathrm{d}\pi'}{\int_0^\infty G_{\pi'}(\pi-\pi')\mathrm{d}\pi'}, \tag{A.2}$$

$$\overline{N_n}(\pi) = \int_0^\infty N_n(\pi')G_{\pi'}(\pi-\pi')\mathrm{d}\pi'. \tag{A.3}$$

The iteration converges when $= \overline{N_n}(\pi) \approx \overline{N}(\pi)\ \forall\pi$, that is, when $N_n(\pi) \approx N(\pi)\ \forall\pi$. The first iterations produce a result that is close to the final answer, with the subsequent iterations giving only small corrections. In our calculation, we set as initial function of the iteration $N_0(\pi) = \overline{N}(\pi)$, and we carry out a number of iterations until the Pearson χ^2 test

$$\frac{1}{N_p-2}\sum_{j=2}^{N_c-1}\frac{[\overline{N_n}(\pi_j)-\overline{N}(\pi_j)]^2}{\overline{N_n}(\pi_j)}, \tag{A.4}$$

reaches the minimum value. Further iterations would enter within the noise.

This algorithm has a number of beneficial properties (Lucy 1974, 1994): all the functions are defined as being positive, the likelihood increases with the number of iterations, the method is insensitive to high-frequency noise in $\overline{N}(\pi)$, and so on. We note, however, that precisely because this method only works when N are positive functions, it does not work with negative ones.

3

Gaia DR2 extended kinematic maps. Part III: Rotation curves analysis, dark matter and MOND tests

In the previous chapter, we showed how we can obtain the density distribution in the outer disc by using numerical methods. In this chapter, the same method is applied to kinematics. Our work is based on the extended kinematic maps of Gaia DR2 data produced by López-Corredoira & Sylos Labini (2019), who applied the Lucy's deconvolution method, described in detail in Chapter 2, to obtain a map of all the velocity components and their dispersions in cylindrical coordinates. We continue their work, by analysing rotational velocities in the outer disc.

We determine the rotation curve using the Jeans equation in cylindrical coordinates, which is a traditional, widely-used approach. As expected, we find a flat rotation curve, with a very small positive gradient, that might be attributed to fluctuations. Interestingly, we observe that the rotation curve has very little dependence on Galactic height.

As the next step, we fit the rotation curve with models that include either a dark matter halo or Modified Newtonian dynamics (MOND). We find that both approaches can fit the observed curves well and the parameters obtained by the models are in good agreement with previous studies.

The Jeans equation, which is an essential tool for this work, assumes that the system is axisymmetric and in equilibrium. However, as we discuss in Section

1.3.3, observations suggest that our Galaxy deviates from both axisymmetry and equilibrium. We therefore investigated how this influences the application of the Jeans equation and whether its use is valid in the outer disc. To this end, we made N-body simulations of mock galaxies not in equilibrium and we studied their rotation curve. We used two methods of calculating the circular velocities, one from the Jeans equation, as applied also to real data, and the other by deriving the velocity from the gravitational force. Comparing the rotation curves calculated from these two different approaches reveals that they are in good agreement, as long as the radial velocity is smaller than 10% of the azimuthal one. When the radial velocity exceeds this value, the Jeans equation significantly overestimates the circular velocity and hence the Galactic mass. In the Milky Way this critical ratio of radial-to-azimuthal velocity is exceeded at galactocentric distance $\sim$20 kpc. Since with the current data we are unable to reach distances greater than that, we cannot say with certainty how significant the correction to the Jeans equation would be at larger distances. It is clear, however, that applying the Jeans equation in the outer disc can lead to important biases and this result has to be explored further with more precise data.

This work was published in the following article:
Astronomy and Astrophysics (2020), 'Gaia-DR2 extended kinematical maps. Part III: Rotation curves analysis, dark matter and MOND tests', **642**, A95.
The article is attached in the following pages. This work was carried during a visit at the Instituto Dei Sistemi Complessi in Rome under the supervision by Dr. Francesco Sylos Labini, where we developed the N-body simulations and analysis of the Jeans equation.

A&A 642, A95 (2020)
https://doi.org/10.1051/0004-6361/202038736

Astronomy & Astrophysics

Gaia-DR2 extended kinematical maps

III. Rotation curves analysis, dark matter, and MOND tests

Ž. Chrobáková[1,2], M. López-Corredoira[1,2], F. Sylos Labini[3,4,5], H.-F. Wang[6,7,⋆], and R. Nagy[8]

[1] Instituto de Astrofísica de Canarias, 38205 La Laguna, Tenerife, Spain
e-mail: zofiachrobakova@gmail.com
[2] Departamento de Astrofísica, Universidad de La Laguna, 38206 La Laguna, Tenerife, Spain
[3] Centro Ricerche Enrico Fermi, Via Panisperna 89A, 00184 Rome, Italy
[4] Istituto dei Sistemi Complessi, Consiglio Nazionale delle Ricerche, 00185 Roma, Italia
[5] Istituto Nazionale Fisica Nucleare, Unità Roma 1, 00185 Roma, Italia
[6] South-Western Institute for Astronomy Research, Yunnan University, Kunming 650500, PR China
[7] Department of Astronomy, China West Normal University, Nanchong 637009, PR China
[8] Faculty of Mathematics, Physics, and Informatics, Comenius University, Mlynská dolina, 842 48 Bratislava, Slovakia

Received 24 June 2020 / Accepted 21 July 2020

ABSTRACT

Context. Recent statistical deconvolution methods have produced extended kinematical maps in a range of heliocentric distances that are a factor of two to three larger than those analysed in Gaia Collaboration (2018, A&A, 616, A11) based on the same data.
Aims. In this paper, we use such maps to derive the rotation curve both in the Galactic plane and in off-plane regions and to analyse the density distribution.
Methods. By assuming stationary equilibrium and axisymmetry, we used the Jeans equation to derive the rotation curve. Then we fit it with density models that include both dark matter and predictions of the MOND (Modified Newtonian dynamics) theory. Since the Milky Way exhibits deviations from axisymmetry and equilibrium, we also considered corrections to the Jeans equation. To compute such corrections, we ran N-body experiments of mock disk galaxies where the departure from equilibrium becomes larger as a function of the distance from the centre.
Results. The rotation curve in the outer disk of the Milky Way that is constructed with the Jeans equation exhibits very low dependence on R and z and it is well-fitted both by dark matter halo and MOND models. The application of the Jeans equation for deriving the rotation curve, in the case of the systems that deviate from equilibrium and axisymmetry, introduces systematic errors that grow as a function of the amplitude of the average radial velocity. In the case of the Milky Way, we can observe that the amplitude of the radial velocity reaches ∼10% that of the azimuthal one at $R \approx 20$ kpc. Based on this condition, using the rotation curve obtained from the Jeans equation to calculate the mass may overestimate its measurement.

Key words. Galaxy: disk – Galaxy: kinematics and dynamics

1. Introduction

Substantial progress has been made in the study of the Milky Way rotation curve thanks to the application of a novel range of methods. Inside the solar circle, the tangent-point method has been applied by measuring spectral profiles of the HI and CO line emissions (Burton & Gordon 1978). Another approach considers the radial velocity of an object, which requires that its distance be measured independently, for example, by trigonometric or spectroscopic determinations. For this purpose, there is a variety of objects that can be adopted, such as OB stars and their associated molecular clouds (Blitz et al. 1982), the thickness of the HI layer (Merrifield 1992), the red giant branch and red clump (Bovy et al. 2012; Huang et al. 2016), classical Cepheids (Pont et al. 1997; Mróz et al. 2019), and a number of others. Rotation velocities can also be determined by measuring proper motions: when these are provided by Very Long Baseline Interferometry (VLBI) techniques, the rotation curve can be determined with high accuracy (Honma et al. 2019). The combination of proper motions from USNO-B1 observations with the Two Micron All Sky Survey (2MASS) photometric data has also been used to determine the rotation curve (López-Corredoira 2014). A powerful tool for measuring the rotation curve of the Milky Way is the VLBI Experiment for Radio Astrometry (VERA), which uses trigonometric determinations of three-dimensional positions and velocities of individual maser sources (Reid et al. 2009; Honma et al. 2015).

An significant study was carried by Bhattacharjee et al. (2014) to construct the rotation curve of the Milky Way from ∼0.2 kpc to ∼200 kpc by using a variety of disk and non-disk tracers. In analysing the velocity anisotropy parameter, they also estimated a lower limit for the Milky Way mass. Their work was continued by Bajkova & Bobylev (2017), who combined circular velocities of masers at low distances with the rotation curve of Bhattacharjee et al. (2014) and fit the result using a number of models, varying, in particular, the dark matter halo, where they refine parameters for six different models. A comparison of some of our fit parameters with the results of Bajkova & Bobylev (2017) is given in Sect. 5. An excellent review of the current status of the study of the rotation curve of the Milky Way is given in Sofue (2020).

⋆ LAMOST fellow.

A&A 642, A95 (2020)

Today, the *Gaia* mission of the European Space Agency (Gaia Collaboration 2016) provides a new possibility for studying the Milky Way with unprecedented accuracy thanks to data that offers the most accurate information about our Galaxy to date. Indeed, the *Gaia* data offer very precise determinations of position, proper motions, radial velocity measurements, and distance for millions of stars, although the errors of distance measurements increase with the distance from the observer.

In this paper, we present a systematical analysis of the Milky Way rotation curves derived by means of different methods and by using the Second Data Release (DR2) of the *Gaia* mission (Gaia Collaboration 2018a). To calculate the rotation curve, we use the Jeans equation that relates the circular velocity to observational quantities, such as the Galactocentric radial and tangential velocities, along with their respective dispersions. To do so, we must assume that the gravitational potential of Milky Way is axisymmetric and that the Galaxy is in a steady state configuration. In addition, by using numerical N-body experiments of simple disk models, we try to quantify the effect of the deviations from the equilibrium configuration on the determination of the rotation curve through the Jeans equation.

This paper is organized as follows: in Sect. 2, we describe the selection of the data used in this paper and in Sect. 3, we illustrate the method used to measure the Milky Way's rotation curve and present our determinations. In Sect. 4, we explain the method for calculating the density distribution from the Poisson equation by using the measured rotation curve. In Sect. 5, we fit different density models to our determination of the rotation curve using standard dark matter approaches, that is, by assuming that the Galaxy is embedded in a quasi-spherical halo whose mass can be then derived on the basis of such an hypothesis. In Sect. 6, we present our density models based on the Modified Newtonian Dynamics (MOND) theory. We study in Sect. 7 the deviations from the Jeans equation in out-of-equilibrium systems. Finally, in Sect. 8, we present our conclusions.

2. Data selection

López-Corredoira & Sylos-Labini (2019, hereafter LS19) have produced extended kinematic maps of the Milky Way by using data from the second *Gaia* data release DR2 (Gaia Collaboration 2018a) and considering stars with measured radial heliocentric velocities and with parallax error less than 100%. Their total sample contains 7 103 123 sources. Such objects were observed by the Radial Velocity Spectrometer (RVS, Cropper et al. 2018), which collects medium-resolution spectra (spectral resolution $\frac{\lambda}{\Delta\lambda} \approx 11\,700$) over the wavelength range of 845–872 nm, centred on the Calcium triplet region. Radial velocities are averaged over a 22-month observational time span. Most sources have a magnitude brighter than 13 in the G filter.

As the parallax error grows with the distance from the observer, LS19 applied a statistical deconvolution of the parallax errors based on the Lucy's inversion method (Lucy 1974) to statistically estimate the distance. In this way, they derived the extended kinematical maps in the range of Galactocentric distances up to 20 kpc. We chose this method due to its advantage over other Bayesian methods (e.g. Astraatmadja & Bailer-Jones 2016; Bailer-Jones et al. 2018) as it does not assume any priors about the Milky Way density distribution. Any other method, such as the Lutz-Kelker method (Lutz & Kelker 1973), is not appropriate here since it would assume a uniform stellar volume density and a constant ratio σ_π/π, where π is the observed parallax and σ_π its standard deviation. For more details on this topic, see Luri et al. (2018), which gives an extensive analysis of different methods if inferring distance from the parallax, along with their respective advantages and disadvantages.

In further detail, the effective temperatures for the sources with radial velocities that LS19 considered are in the range of 3550 to 6900 K. The uncertainties of the radial velocities are: 0.3 km s^{-1} at $G_{\rm RVS} < 8$, 0.6 km s^{-1} at $G_{\rm RVS} = 10$, and 1.8 km s^{-1} at $G_{\rm RVS} = 11.75$; along with systematic radial velocity errors of <0.1 km s^{-1} at $G_{\rm RVS} < 9$ and 0.5 km s^{-1} at $G_{\rm RVS} = 11.75$. The uncertainties of the parallax are: 0.02–0.04 mas at $G < 15$, 0.1 mas at $G = 17$, 0.7 mas at $G = 20$ and 2 mas at $G = 21$. The uncertainties of the proper motion are: 0.07 mas yr^{-1} at $G < 15$, 0.2 mas yr^{-1} at $G = 17$, 1.2 mas yr^{-1} at $G = 20$ and 3 mas yr^{-1} at $G = 21$. For details on radial velocity data processing and the properties and validation of the resulting radial velocity catalogue, see Sartoretti et al. (2018) and Katz et al. (2019). The set of standard stars that was used to define the zero-point of the RVS radial velocities is described in Soubiran et al. (2018). LS19 consider the zero-point bias in the parallaxes of *Gaia* DR2, as found by Lindegren et al. (2018), Arenou et al. (2018), Stassun & Torres (2018), Zinn et al. (2019); however, they find that the effect of the systematic error in the parallaxes is negligible, so the maps that we use from their study (LS19, Figs. 8–12) do not consider the zero-point correction. We describe the way we use these maps in Sect. 3 to construct the rotation curves (Fig. 1), however, in Fig. 2, we include the zero-point correction to demonstrate that the difference is negligible.

3. Rotation curves

From the *Gaia* DR2 catalogue, we estimate, for each object, the parallax π, the Galactic coordinates (l, b), the radial velocity v_r, and two proper motions in equatorial coordinates $\mu_\alpha \cos\delta$ and μ_δ. For our analysis, we need to know the Galactocentric position of stars in cylindrical coordinates (R, z, Φ), and the Galactocentric velocity in cylindrical coordinates (v_R, v_Φ, v_z). The transformation from these two coordinates systems can be found in LS19.

We limit the range of vertical distance to $|z| < 2.2$ kpc as we find that far off-plane data are affected by larger errors in their parallax determinations. We investigate the disk beyond the solar Galactocentric radius, that is, for 8.4 kpc< $R < 21.2$ kpc.

To determine the rotation curve, we consider the one component of Jeans equations in cylindrical coordinates (Binney & Tremaine 1987, Ch. 4.2, 4–29a):

$$\frac{\partial(\nu\overline{v_{\rm R}})}{\partial t} + \nu\left(\frac{\overline{v_{\rm R}^2} - \overline{v_\Phi^2}}{R} + \frac{\partial\Phi}{\partial R}\right) + \frac{\partial(\nu\overline{v_{\rm R}^2})}{\partial R} + \frac{\partial(\nu\overline{v_{\rm R}v_z})}{\partial z} = 0\,, \quad (1)$$

where R is the Galactocentric radius, $v_{\rm R}$ is the radial velocity, v_z is the vertical velocity, v_Φ is the azimuthal velocity, and ν is the volume density. The quantity $\overline{v^2}$ is the average square velocity for each component that can be written as $\overline{v^2} = \sigma^2 + \bar{v}^2$, where σ is the velocity dispersion. For a detailed calculation of the velocities and their respective dispersion, see LS19.

The rotational velocity is defined as (Binney & Tremaine 1987)

$$v_c^2(R, z) = R\frac{\partial\Phi}{\partial R}\,. \quad (2)$$

We use the standard assumption that the volume density can be written as

$$\nu(R, z) = \rho_0 e^{-\frac{R}{h_R}} e^{-\frac{|z|}{h_z}}\,, \quad (3)$$

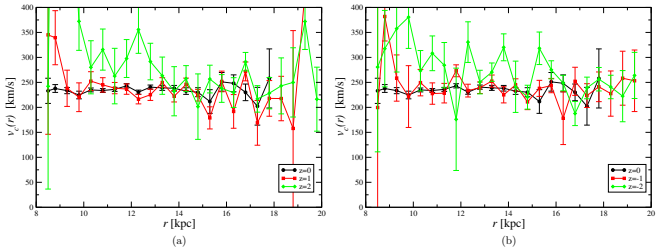

Fig. 1. *Panel a*: rotation curves at different heights for positive values of z. *Panel b*: rotation curves at different heights for negative values of z. The error bars represent the standard deviation.

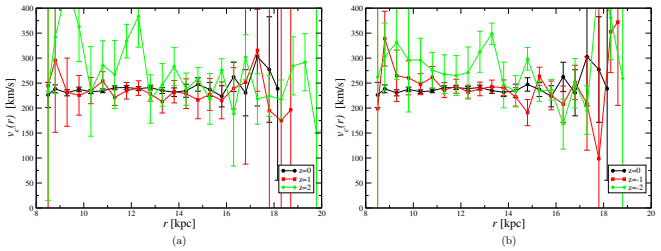

Fig. 2. Rotation curves for different values of z including the zero point correction in parallax. *Panel a*: rotation curves at different heights for positive values of z. *Panel b*: rotation curves at different heights for negative values of z. The error bars represent the standard deviation.

where h_R is the scale length and h_z is the scale height. From Eqs. (1)–(3) we obtain the rotational velocity as function of R, z, that is, the rotation curves,

$$v_c^2 = \overline{v_\Phi}^2 + \sigma_\Phi^2 + \left(\overline{v_R}^2 + \sigma_R^2\right)\frac{R-h_R}{h_R} - 2R\overline{v_R}\frac{\partial \overline{v_R}}{\partial R} - R\frac{\partial \sigma_R^2}{\partial R} + \frac{R}{h_z}\frac{z}{|z|}\overline{v_R v_z} - R\frac{\partial(\overline{v_R v_z})}{\partial z}. \quad (4)$$

We determined the rotation curves for different values of z, in the direction of the anti-center, in bins of size $\Delta R = 0.5$ kpc and $\Delta z = 0.2$ kpc. For what concerns the scale parameters in Eq. (3), we chose values of $h_R = 2.5$ kpc and $h_z = 0.3$ kpc (Jurić et al. 2008). Figure 1 shows the results of our fit.

Figure 2 shows the rotation curves, including the zero-point correction in parallax. The difference from the rotation curves in Fig. 1 is negligible and we do not consider this correction for the rest of the analysis. The results for different scale parameters are almost identical, as we show in Fig. 3. We observe a flat rotation curve, although it does exhibit some fluctuations. Our rotation curve in the plane of the Galaxy has a small positive gradient of 0.54 ± 0.7(stat.) ± 0.5(syst.) km s^{-1} kpc^{-1}. Recent results have shown an opposite trend: Eilers et al. (2019) measured rotation curve for Galactocentric distances 5 kpc $\lesssim R \lesssim$ 25 kpc by combining spectral data from the Apache Point Observatory Galactic Evolution Experiment (APOGEE, Majewski et al. 2017) and photometric information from Wide-field Infrared Survey Explorer (WISE, Wright et al. 2010), 2MASS (Skrutskie et al. 2006), and *Gaia* DR2, finding a rotation curve with a declining slope of -1.7 ± 0.1 km s^{-1} kpc^{-1}, with a systematic uncertainty of 0.46 km s^{-1} kpc^{-1}. A similar result was obtained by Mróz et al. (2019), who used classical Cepheids to obtain the rotation curve of the Milky Way for Galactocentric distances 4 kpc $\lesssim R \lesssim$ 20 kpc, finding a rotation curve with a small negative slope of -1.34 ± 0.21 km s^{-1} kpc^{-1}. Bhattacharjee et al. (2014) have also used the Jeans equation, but only for large distances ($R >$ 20 kpc), which we do not consider in our analysis. For the disk tracers, they use the tangent point method for small distances and for higher distances they assume that the tracers follow nearly circular orbit. The advantage is that their method is independent from any density model, although it strongly depends on values of Galactic constants (Sun's distance from,

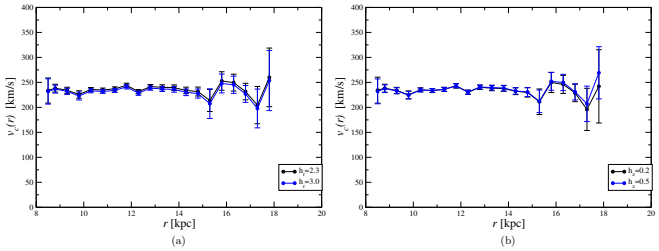

Fig. 3. Rotation curves for different values of the scale parameters. *Panel a*: rotation curves for different values of h_R, for $z = 0$. *Panel b*: rotation curves for different values of h_z, for $z = 0$. The error bars represent the standard deviation.

and circular rotation speed around, the Galactic centre). Nevertheless, their results for rotation curve for various values of Galactic constants are consistent with our findings. We discuss these results more in detail in what follows.

4. Density distribution from the Poisson equation

Based on the results obtained for the rotation curve, we proceed to determine the density distribution in the Milky Way by considering different approaches. The first one is based on the Poisson equation in cylindrical coordinates and it assumes the dependence of the rotation speed with the azimuth to be negligible:

$$\frac{1}{R}\frac{\partial}{\partial R}\left(R\frac{\partial\Phi}{\partial R}\right)+\frac{\partial^2\Phi}{\partial z^2}=4\pi G\rho(R,z). \tag{5}$$

The first term on left side can be easily obtained by using Eq. (2). The second term, on the left side, can be obtained with the same relation and switching derivatives

$$\frac{\partial^2}{\partial z^2}\left(\frac{\partial\Phi}{\partial R}\right)=\frac{1}{R}\frac{\partial^2 v_c^2}{\partial z^2},$$
$$\frac{\partial}{\partial R}\left(\frac{\partial^2\Phi}{\partial z^2}\right)=\frac{1}{R}\frac{\partial^2 v_c^2}{\partial z^2}.$$

By integrating the latter relation we find

$$\frac{\partial^2\Phi}{\partial z^2}=-\int_R^{R_{\rm max}}\frac{1}{R}\frac{\partial^2 v_c^2}{\partial z^2}\mathrm{d}R+\Phi(R_{\rm max},z=0). \tag{6}$$

To determine derivatives of v_c with respect to R, z, we assume that v_c^2 has a linear behaviour of the type

$$v_c^2=a(z)(R-14)+b(z), \tag{7}$$

where clearly $a(z)$ and $b(z)$ must be determined from the data. We find that $a(z)$ and $b(z)$ can be nicely fitted by parabolas and therefore, we can write

$$v_c^2(z)=\left[(\alpha+\beta z^2)+(\gamma+\delta z^2)(R-14)\right], \tag{8}$$

where the numerical values of $\alpha, \beta, \gamma, \delta$ are estimated from the data and the values are given below. We use Eqs. (2) and (7) to express the first term of Eq. (5) as

$$\frac{1}{R}\frac{\partial}{\partial R}\left(R\frac{\partial\Phi}{\partial R}\right)=\frac{1}{R}\frac{\partial}{\partial R}\left(a(z)(R-14)+b(z)\right)$$
$$=\frac{a(z)}{R} \tag{9}$$

By making the derivative of the fit of the rotational velocity (Eq. (8)) with respect to z, we express Eq. (6) as

$$\frac{\partial^2\Phi}{\partial z^2}=2\beta\ln\left(\frac{R}{R_{\rm max}}\right)+2\delta(R-R_{\rm max})$$
$$-28\delta\ln\left(\frac{R}{R_{\rm max}}\right)+\Phi(R_{\rm max},z=0). \tag{10}$$

We find that the best fit values for $a(z)$ and $b(z)$ are (see Fig. 4):

$a(z) = (-2200 \pm 400)z^2 + (1000 \pm 1000)$

$b(z) = (11\,400 \pm 1000)z^2 + (53\,000 \pm 1500)$.

In the Galactic plane, the value of $a(z)$ is positive, which means that in the plane the velocity gradient is positive too: this must be compensated by density increase. That is clearly non-physical as we know that in our Galaxy, the density decreases exponentially in the outwards direction. Therefore, we conclude that we cannot use the Poisson equation to determine the density analytically. This problem may be related to large fluctuations present in the data, as well as by the fact that the system is not in equilibrium, so it does not satisfy the assumptions of the Jeans equation. We analyse the effect of the deviations from equilibrium in greater detail in Sect. 7.

5. Density fit with the dark matter model

Another method to fit the rotation curve data can be done by making use of known density models. By assuming that the system is in equilibrium and made by different mass components, both the density and the rotational velocity can be expressed as

$$\rho=\rho_{\rm bulge}+\rho_{\rm disk}+\rho_{\rm halo}, \tag{11}$$
$$v_c^2=v_{c,\rm bulge}^2+v_{c,\rm disk}^2+v_{c,\rm halo}^2, \tag{12}$$

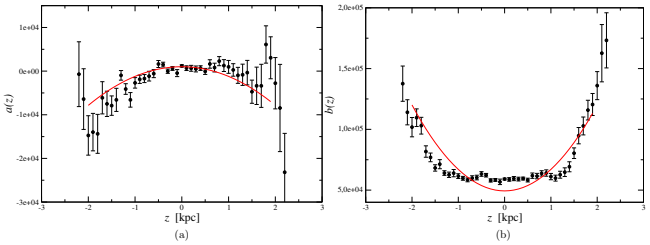

Fig. 4. *Panel a*: fit of $a(z)$. *Panel b*: fit of $h(z)$ (see Eq. (8)). The error bars represent the standard deviation.

that is, we have decomposed the density and the circular velocity as the sum of three terms: the bulge, the disk, and the halo. Here, we examine each of these terms in more detail.

We do not fit the bulge, as we are interested mainly in outer parts of disk, where contribution of the bulge is negligible: we use

$$v^2_{c,\mathrm{bulge}} = \frac{GM_{\mathrm{bulge}}}{R}\,, \tag{13}$$

where $M_{\mathrm{bulge}} = 2\times10^{10}\,M_\odot$ (Valenti et al. 2016).

For the disk, by assuming the balance between the gravitational and centrifugal forces at a generic point (r,ϕ,h) (for a detailed derivation see Appendix A) we derive:

$$\int_{-H/2}^{H/2}\int_{R_{\mathrm{min}}}^{R_{\mathrm{max}}} \frac{2}{r}\left[\frac{(\hat{r}+r)(\hat{r}-r)+\Delta h^2}{[(\hat{r}-r)^2+\Delta h^2]\sqrt{(\hat{r}+r)^2+\Delta h^2}}E(k) - \frac{1}{\sqrt{(\hat{r}+r)^2+\Delta h^2}}K(k)\right]\nu(\hat{r},\hat{h})\mathrm{d}\hat{r}\mathrm{d}\hat{h} + A\frac{v_{c,\mathrm{disk}}(r,h)^2}{r} = 0\,, \tag{14}$$

where $K(k), E(k)$ are complete elliptic integrals of the first and second kind respectively, and

$$k^2 = \frac{4\hat{r}r}{(\hat{r}+r)^2+\Delta h^2}\,, \tag{15}$$

where $\Delta h^2 = (\hat{h}-h)^2$. For the sake of simplicity, we consider only a thin disk and we approximate $\Delta h \approx h$. For the density in Eq. (14) we used the relation:

$$\nu(\hat{r},\hat{z}) = \rho_{0\mathrm{d}}e^{-\hat{r}/h_{\mathrm{Rd}}}e^{-|\hat{h}|/h_z}\,. \tag{16}$$

In Eq. (14) the constant A is the Galactic rotation number defined as

$$A = \frac{R_{g,\mathrm{max}}V_0^2}{GM_{d,\mathrm{max}}}\,, \tag{17}$$

where $M_{d,\mathrm{max}}$ is mass of the disk, for which we use the value $M_{d,\mathrm{max}} = 6.5\times10^{10}\,M_\odot$ (Sofue et al. 2013). $R_{g,\mathrm{max}}$ is the radius of the disk, which we fix at 25 kpc, V_0 is the maximum velocity corresponding to the flat part of the rotation curve in the dataset: 257 km s^{-1} in our case and G is the gravitational constant: 4.302×10^{-6} kpc $M_\odot^{-1}$ (km s)$^{-2}$. We calculate the fit in the Galactic plane, where $\Delta h \to 0$ and Eq. (14) becomes

$$\int_{R_{\mathrm{min}}}^{R_{\mathrm{max}}}\left[\frac{E(k)}{\hat{r}-r} - \frac{K(k)}{\hat{r}+r}\right]\rho_{0\mathrm{d}}e^{-\hat{r}/h_{\mathrm{Rd}}}\hat{r}\mathrm{d}\hat{r} + A\frac{v_{c,\mathrm{disk}}(r)^2}{2|h|} = 0, \tag{18}$$

where

$$k^2 = \frac{4r\hat{r}}{(\hat{r}+r)^2}\,. \tag{19}$$

To fit the dark matter halo, we assume this is well approximated by the so-called Navarro, Frenk, and White density profile (Navarro et al. 1997)

$$\rho_{\mathrm{halo}} = \frac{\rho_{0h}}{\frac{R}{R_s}\left(1+\frac{R}{R_s}\right)^2}\,, \tag{20}$$

$$v^2_{c,\mathrm{halo}}(R) = \frac{4\pi G\rho_{0h}R_s^3}{R}\left[\log\left(\frac{R_s+R}{R_s}\right) - \frac{R}{R_s+R}\right]. \tag{21}$$

We use the least-squares method to find the best values of the free parameters. As this method requires a long computational time, we fix some well-known parameters and only fit those that are not so well determined. First, we fit only data in the Galactic plane, where we fix $h_{\mathrm{Rd}} = 2.5$ kpc and $R_s = 14.8$ kpc, which are the values found by Eilers et al. (2019). For the free parameters, we obtain the values $\rho_{0h} = 2\times10^7\,M_\odot$ kpc^{-3} and $\rho_0 = 3.83\times10^8\,M_\odot$ kpc^{-3}, with the value of the minimal $\chi^2 = 15.424$ for 107 points. We plot this result in Fig. 5a. We see that our rotation curves are well explained by a dominant dark matter halo, with a minimal contribution from the disc. From these values, we calculate the mass of the dark matter halo up to 25 kpc to be $M_h = 3.52\times10^{11}\,M_\odot$, which is smaller than $7.25\times10^{11}\,M_\odot$ found by Eilers et al. (2019), but higher than $2.9\times10^{11}\,M_\odot$ found by Bajkova & Bobylev (2017). For the disk, we find $M_d = 1.41\times10^{10}\,M_\odot$, which is lower than values found in the literature, for example, $6.5\times10^{10}\,M_\odot$ as found by Sofue et al. (2009), $0.95\times10^{11}\,M_\odot$ as found by Kafle et al. (2014), or $6.51\times10^{10}\,M_\odot$ as found by Bajkova & Bobylev (2017).

For the off-plane data, we fit rotation curves for different values of z at the same time, using relation (14), which adds one more free parameter h_z to the fit. Again, to save computational time, we restricted the number of free parameters and

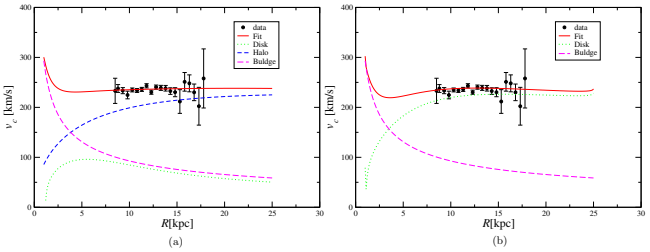

Fig. 5. Fit of the rotation curve for only $z = 0$ using dark matter (*left*) and the MOND theory (*right*). The data are binned with bins of size $\Delta R = 0.5$ kpc and $\Delta z = 0.1$ kpc. (a) Dark matter, (b) MOND.

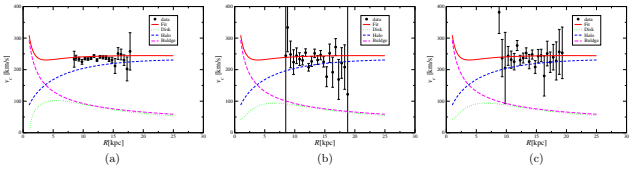

Fig. 6. Fit of the rotation curve for various values of z using dark matter model. The data is binned with bins of size $\Delta R = 0.5$ kpc and $\Delta z = 0.1$ kpc. (a) $z = 0$ kpc, (b) $z = 1.0$ kpc, (c) $z = -1.0$ kpc.

fixed $h_R = 2.5$ kpc and $R_\epsilon = 14.8$ kpc. We find $h_z = 0.3$ kpc, $\rho_0 = 4.1 \times 10^9\, M_\odot\,\mathrm{kpc}^{-3}$ and $\rho_{0b} = 2.389 \times 10^7\, M_\odot\,\mathrm{kpc}^{-3}$, with the value of minimal $\chi^2 = 2510.37$ for 4653 points. In Fig. 6, we plot the fit for various values of z. We see that in all cases, the dark matter halo is strongly dominant and the contribution from the disk is less important, which is as expected from rotational velocity that does not change with vertical distance.

This result is in agreement with result of Eilers et al. (2019), who also fitted their rotation curve with a similar model. They also find a dominant dark matter halo, with free parameter $\rho_{0b} = 1.06 \times 10^7\, M_\odot\,\mathrm{kpc}^{-3}$. However, we disagree with result from Jałocha et al. (2010), who found that the gross mass distribution in our Galaxy is disk-like, without the need for a halo. Jałocha et al. (2010) obtained their result based on modelling vertical gradient of azimuthal velocity, assuming the quasi-circular orbit approximation, and relating v_c to v_ϕ directly from the balance condition of the radial component of gravitational and inertial force. We guess that the difference between our results comes from the fact that Jałocha et al. (2010) did not take the Jeans equations into account when deriving rotational velocity. Indeed, in this latter work, assuming quasi-circular orbits v_ϕ was directly related to v_c to obtain $v_\phi = \frac{z}{R} v_c$.

6. Density fit with the MOND model

We tried to fit our results using the MOND theory, without invoking the presence of a heavy dark matter halo. To this purpose we have recalculated the expressions for the disk and the bulge, using relations from MOND (Milgrom 1983):

$$a_M = \frac{a_N}{\mu(\frac{a_M}{a_0})}\,, \tag{22}$$

where

$$\mu\left(\frac{a_M}{a_0}\right) = \sqrt{\frac{1}{1+\left(\frac{a_0}{a_M}\right)^2}}\,, \tag{23}$$

with the value of $a_0 = 1.2 \times 10^{-10}\,\mathrm{ms}^{-2}$ (Scarpa et al. 2006). Solving Eq. (22) analytically yields

$$a_M = \sqrt{\frac{1}{2}a_N^2 + \sqrt{\frac{1}{4}a_N^4 + a_N^2 a_0^2}}\,. \tag{24}$$

Equation (22) is indeed an approximation, which does not exactly stray from a spherical symmetric mass distribution. The exact solution may be analysed in the context for Bekenstein-Milgrom MOND theory derived from the modification of classical Newtonian dynamics (Brada & Milgrom 1995). However, the difference between the approximation of Eq. (22) and the exact solution is small, so we neglect it here.

For the fit, we only used the disk and the bulge components. In Fig. 5b, we plot the result of the fit for the Galactic plane, nicely matching the observed value. For the free parameters, we found $\rho_0 = 7.49 \times 10^6\, M_\odot\,\mathrm{kpc}^{-3}$ and $h_R = 4.8$ kpc. The values of minimal χ^2 is $\chi^2 = 15.776$ for 107 points, which is similar to the

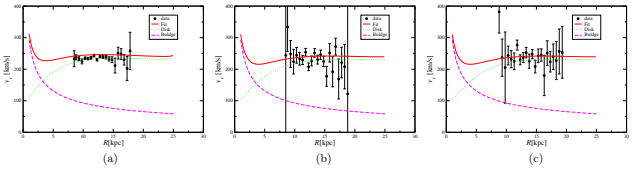

Fig. 7. Fit of the rotation curve for various values of z using the MOND theory. The data are binned with bins of size $\Delta R = 0.5$ kpc and $\Delta z = 0.1$ kpc. (a) $z = 0$ kpc, (b) $z = 1.0$ kpc, (c) $z = -1.0$ kpc.

value for Newtonian fit. The mass of the disk up to 25 kpc found with these parameters is $M_d = 2.77 \times 10^{10}\, M_\odot$ which is almost two times higher than that obtained with the dark matter model.

We tried to fit the off-plane rotation curve with the same approach. Again, we fit data for all z with models for all z at the same time. Thus, we find: $\rho_0 = 9.15 \times 10^9\, M_\odot\,\mathrm{kpc}^{-3}$ and $h_R = 5.0$ kpc. We fixed the value of scale-height to $h_z = 0.3$ kpc. The obtained value of minimal $\chi^2 = 2677.58$ for 4653 points, which is comparable with the Newtonian case. In Fig. 7, we plot the results of the fit with MOND for different values of z. We see that off-plane, the fit is satisfying and there is no preference for the dark matter model over the MOND model. However, our result contradicts that of Lisanti et al. (2019), who also used Milky Way observables to compare the differences between dark matter and MOND theories. They performed a Bayesian likelihood analysis to compare the predictions of the model with the observed quantities. They find that the dark matter model is preferred, as MOND-like theories struggle to simultaneously explain both the rotational velocity and vertical motion of nearby stars in the Milky Way.

7. Corrections to the Jeans equation

So far, we used the Jeans equation to determine the rotation curve of the Milky Way and its density profile. We recall that the basic assumptions of the Jeans equation are that the system is collisionless, axisymmetric, and in equilibrium. While the first condition represents a reasonable working hypothesis since collisional effects take place on much longer time scales than those that astrophysically relevant, the recent *Gaia* data have shown that the Milky Way is not in a stationary situation as there are large-scale gradients in all components of the velocity field and there are clear deviations from axisymmetry (Gaia Collaboration 2018b; Wang et al. 2018; López-Corredoira & Sylos-Labini 2019; Wang et al. 2020). The dynamical origin of such features represents an open problem that has been explored by several authors (Antoja et al. 2018; Binney & Schönrich 2018). For instance, it has been concluded that the Galactic disk is still dynamically young and was last perturbed less than 1 Gyr ago, therefore modelling it as axisymmetric and in equilibrium is incorrect (Antoja et al. 2018). The problem of reliability with regard to the Jeans equation was also studied by Haines et al. (2019), who analysed an N-body simulation of a stellar disk which had been perturbed by the recent passage of a dwarf galaxy and studied the surface density of the system based on the Jeans equation. They found that the Jeans equation gives reasonable results in over-dense regions, but fails in under-dense regions. Thus, the development of non-equilibrium methods for estimating the dynamical matter density locally and in the outer disk is necessary.

In order to test the effects of the deviations from a stationary configuration and axisymmetry on the Jeans equation, we consider N-body simulations of mock galactic systems that are not completely in an equilibrium configuration. The evolution of these systems was discussed in details in Benhaiem et al. (2017, 2019); Sylos Labini et al. (in prep.). We consider, hereafter, one of these systems, consisting of a thin, rotating, self-gravitating disk embedded in an ellipsoidal dark matter halo with an isotropic velocity dispersion. The inner regions of this system are very close to a stationary configuration, while the outer regions are progressively out-of-equilibrium. The signature of such a situation is represented by the behaviour of the radial velocity averaged in shells: at small distances from the centre this is close to zero, while at large enough distances, it becomes positive: the amplitude grows with the distance from the centre.

The circular velocity from the Jeans equation is

$$v_{c,J}^2 = \overline{v_\Phi}^2 - \overline{v_R}^2 \left(1 + \frac{\partial \ln \nu}{\partial \ln R} + \frac{\partial \ln \overline{v_R}^2}{\partial \ln R}\right), \tag{25}$$

where we neglect the cross-term $\overline{v_R v_\phi}$, as it's contribution to the final result is negligible (∼1%) (Eilers et al. 2019). By definition, the circular velocity can be computed from the gravitational force:

$$v_{c,F}^2 = R F_R = \left|\overline{\boldsymbol{F}} \cdot \boldsymbol{R}\right|, \tag{26}$$

where $\overline{\boldsymbol{F}}$ is the gravitational force acting of the particles contained in the two-dimensional corona at a distance, R, and thickness, ΔR (where R is the cylindrical coordinate). Thus, we compute the gravitational force acting of the ith particle as

$$\boldsymbol{F}_i = G \sum_{j=1}^{N} m_j m_i \frac{(\boldsymbol{r}_i - \boldsymbol{r}_j)}{|\boldsymbol{r}_i - \boldsymbol{r}_j|^3}, \tag{27}$$

where m_i is the mass of the ith particle and we compute its average in a corona. If axisymmetry and stationary equilibrium are established, then $v_{c,F} = v_{c,J}$: the difference between these two quantities thus depends on the deviations from the assumptions underlying the Jeans equation. In the Fig. 8, we plot the ratio:

$$\Theta = \frac{v_{c,J}}{v_{c,F}} \tag{28}$$

as a function of

$$\zeta = \frac{|v_R|}{|v_\phi|}. \tag{29}$$

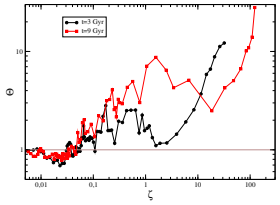

Fig. 8. Ratio of the circular velocity from the Jeans equation and from the force (i.e. Eq. (28)) as a function of the ratio between the average radial velocity and the azimuthal velocity (see Eq. (29)). Black and red circles correspond to the system evolved up to 3/9 Gyr, respectively.

When the radial velocity is small, that is, $\zeta \ll 1$, then $\Theta \approx 1$, whereas when the radial velocity becomes larger than 10% of the azimuthal one, then Θ becomes larger than one. In the Milky Way, $\zeta \approx 0.1$ at $R \approx 20$ kpc, as found by LS19. We note that in Fig. 8, we have reported the behaviour for two different times, that is, 3 and 9 Gyr; indeed, as the external regions are out-of-equilibrium they continue to evolve over time, while the inner regions are quasi stationary.

We conclude that the Jeans equation is reliable when the radial velocity is smaller than 10% of the azimuthal one, otherwise corrections to the Jeans equation become necessary. In particular, we find that the estimation of the circular velocity though the Jeans equation gives an overestimation with respect to the estimation of the circular velocity through the force. This implies that by using $v_{c,J}$ to compute the mass through the relation,

$$M_J(r) = \frac{v_{c,J}^2 \times r}{G}, \tag{30}$$

the real mass is overestimated by a factor that is proportional to Θ^2.

8. Conclusions

In this paper, we study the rotation curve of the Milky Way from the extended kinematic maps of *Gaia*-DR2. We calculated the rotation curve in plane and in off-plane regions, using the Jeans equation. Our results show that the rotation curve in the outer disk has very little dependence on R and z.

We fitted the rotation curve using models with dark matter halo or MOND, using the least-squares method. We find that a model based on dark matter fits the data very well, and the results are in good agreement with other works. For the dark matter model, we obtain the minimal $\chi^2 = 15.424$ for 107 points in the plane and $\chi^2 = 2510.37$ for 4653 points off plane. The MOND model in the plane gives $\chi^2 = 15.776$ for 107 points, which is comparable with the dark matter model. Off-plane the results are similar as well, with $\chi^2 = 2677.58$ for 4653 points, which fits the data similarly to the dark matter model.

We also considered the corrections to the Jeans equation in non-equilibrium and non-axisymmetric systems. Indeed, the Jeans equation assumes that the system is axisymmetric and in equilibrium, which is not the case of the Milky Way. For this reason, we consider N-body simulations of galaxies and calculated the rotational velocity by using the Jeans equation $v_{c,J}$ and by computing the gradient of the gravitational potential $v_{c,F}$. We find that the two ways of calculating the rotational velocity are in good agreement as long as the ratio, ζ, between the modulus of the radial velocity and of the azimuthal velocity is smaller than $\sim$ 10%. When ζ becomes larger than this value, then $v_{c,J} > v_{c,F}$ and, thus, we overestimate the Galactic mass if we use the rotational velocity computed through the Jeans equation. For the case of the Milky Way, it was found in LS19 that $\zeta \approx 0.1$ at $R \approx 20$ kpc: this implies that at a larger galactocentric distance, using the Jeans equation leads to an overestimation the mass of the Milky Way. The *Gaia* DR3 will clarify whether in the range of distances $20 < R < 30$ kpc, such corrections may become large enough to change our view of the Galaxy as a quasi-equilibrium system, thus altering its estimated mass.

Acknowledgements. We thank the anonymous referee for helpful comments, which improved this paper and Agnes Monod-Gayraud (language editor of A&A) for proof-reading of the text. ZC and MLC were supported by the grant PGC-2018-102249-B-100 of the Spanish Ministry of Economy and Competitiveness (MINECO). HFW is supported by the LAMOST Fellow project, National Key Basic R&D Program of China via 2019YFA0405500 and funded by China Postdoctoral Science Foundation via grant 2019M653504, Yunnan province postdoctoral Directed culture Foundation and the Cultivation Project for LAMOST Scientific Payoff and Research Achievement of CAMS-CAS. RN was supported by the Scientific Grant Agency VEGA No. 1/0911/17. This work has made use of data from the European Space Agency (ESA) mission *Gaia* (https://www.cosmos.esa.int/gaia), processed by the *Gaia* Data Processing and Analysis Consortium (DPAC, https://www.cosmos.esa.int/web/gaia/dpac/consortium). Funding for the DPAC has been provided by national institutions, in particular the institutions participating in the *Gaia* Multilateral Agreement.

References

Antoja, T., Helmi, A., Romero-Gómez, M., et al. 2018, Nature, 561, 360
Arenou, F., Luri, X., Babusiaux, C., et al. 2018, A&A, 616, A7
Astraatmadja, T. L., & Bailer-Jones, C. A. L. 2016, ApJ, 832, 137
Bailer-Jones, C. A. L., Rybizki, J., Fouesneau, M., Mantelet, G., & Andrae, R. 2018, AJ, 156, 58
Bajkova, A., & Bobylev, V. 2017, Open Astron., 26, 72
Benhaiem, D., Joyce, M., & Sylos Labini, F. 2017, ApJ, 851, 19
Benhaiem, D., Sylos Labini, F., & Joyce, M. 2019, Phys. Rev. E, 99, 022125
Bhattacharjee, P., Chaudhury, S., & Kundu, S. 2014, ApJ, 785, 63
Binney, J., & Schönrich, R. 2018, MNRAS, 481, 1501
Binney, J., & Tremaine, S. 1987, Galactic Dynamics (Princeton: Princeton University Press)
Blitz, L., Fich, M., & Stark, A. A. 1982, ApJs, 49, 183
Bovy, J., Allende Prieto, C., Beers, T. C., et al. 2012, ApJ, 759, 131
Brada, R., & Milgrom, M. 1995, MNRAS, 276, 453
Burton, W. B., & Gordon, M. A. 1978, A&A, 63, 7
Cropper, M., Katz, D., Sartoretti, P., et al. 2018, A&A, 616, A5
Eilers, A.-C., Hogg, D. W., Rix, H.-W., & Ness, M. K. 2019, ApJ, 871, 120
Gaia Collaboration (Prusti, T., et al.) 2016, A&A, 595, A1
Gaia Collaboration (Brown, A. G. A., et al.) 2018a, A&A, 616, A1
Gaia Collaboration (Katz, D., et al.) 2018b, A&A, 616, A11
Gradshteyn, I. S., Ryzhik, I. M., Jeffrey, A., & Zwillinger, D. 2007, Table of Integrals, Series and Products
Haines, T., D'Onghia, E., Famaey, B., Laporte, C., & Hernquist, L. 2019, ApJ, 879, L15
Honma, M., Nagayama, T., Ando, K., et al. PASJ, 64, 136
Honma, M., Nagayama, T., & Sakai, N. 2015, PASJ, 67, 70
Huang, Y., Liu, X. W., Yuan, H. B., et al. 2016, MNRAS, 463, 2623
Jalocha, J., Bratek, Ł., Kutschera, M., & Skindzier, P. 2010, MNRAS, 407, 1689
Jurić, M., Ivezić, V., & Brooks, A. 2008, ApJ, 673, 864
Kafle, P. R., Sharma, S., Lewis, G. F., & Bland-Hawthorn, J. 2014, ApJ, 794, 59
Katz, D., Sartoretti, P., Cropper, M., et al. 2019, A&A, 622, A205
Lindegren, L., Hernández, J., Bombrun, A., et al. 2018, A&A, 616, A2
Lisanti, M., Moschella, M., Outmezguine, N. J., & Slone, O. 2019, Phys. Rev. D, 100, 083009
López-Corredoira, M. 2014, A&A, 563, A128
López-Corredoira, M., & Sylos-Labini, F. 2019, A&A, 621, A48

Lucy, L. B. 1974, ApJ, 79, 745
Luri, X., Brown, A. G. A., Sarro, L. M., et al. 2018, A&A, 616, A9
Lutz, T. E., & Kelker, D. H. 1973, PASP, 85, 573
Majewski, S. R., Schiavon, R. P., Frinchaboy, P. M., et al. 2017, ApJ, 154, 94
Merrifield, M. R. 1992, AJ, 103, 1552
Milgrom, M. 1983, ApJ, 270, 365
Mróz, P., Udalski, A., Skowron, D. M., et al. 2019, ApJ, 870, L10
Navarro, J. F., Frenk, C. S., & White, S. D. M. 1997, ApJ, 462, 563
Pont, F., Queloz, D., Bratschi, P., & Mayor, M. 1997, A&A, 318, 416
Reid, M. J., Menten, K. M., Zheng, X. W., et al. 2009, ApJ, 700, 137
Sartoretti, P., Katz, D., Cropper, M., et al. 2018, A&A, 616, A6
Scarpa, R. 2006, in First Crisis in Cosmology Conference, eds. E. J. Lerner, & J. B. Almeida, Am. Inst. Phys. Conf. Ser., 822, 253
Skrutskie, M. F., Cutri, R. M., Stiening, R., et al. 2006, ApJ, 131, 1163
Sofue, Y. 2013, Mass Distribution and Rotation Curve in the Galaxy, eds. T. D. Oswalt, & G. Gilmore, 5, 985
Sofue, Y. 2020, Galaxies, 8, 37
Sofue, Y., Honma, M., & Omodaka, T. 2009, PASJ, 61, 227
Soubiran, C., Jasniewicz, G., Chemin, L., et al. 2018, A&A, 616, A7
Stassun, K. G., & Torres, G. 2018, ApJ, 862, 61
Valenti, E., Zoccali, M. A., Gonzalez, O. A., et al. 2016, A&A, 587, L6
Wang, H., López-Corredoira, M., Carlin, J. L., & Deng, L. 2018, MNRAS, 477, 2858
Wang, H. F., López-Corredoira, M., Huang, Y., et al. 2020, MNRAS, 491, 2104
Wright, E. L., Eisenhardt, P. R. M., Mainzer, A. K., et al. 2010, ApJ, 140, 1868
Zinn, J. C., Pinsonneault, M. H., Huber, D., & Stello, D. 2019, ApJ, 878, 136

Appendix A: Derivation of the integral of the thin disk

To derive the rotation curve of a disk in 3D, we derive the equation for balance between the gravitational and the centrifugal force. We consider two points with the coordinates $P(r,\theta,z)$ and $Q(\hat{r},\hat{\theta},\hat{z})$. The distance between these two points can be expressed as $(\hat{r}^2-r^2-2r\hat{r}\cos\hat{\theta}+\Delta h^2)^{1/2}$ and the vector projection as $(\hat{r}\cos\hat{\theta}-r)$, where Δh is the difference in heights $\Delta h=(\hat{h}-h)$. The Newtonian gravitational force on the point P from a body consisting of points Q distributed with a mass density $\hat{\rho}(\hat{r},\hat{h})$ can be expressed as an integral over these points:

$$F_X = \frac{GM_g}{R_g^2}\int_{-H/2}^{H/2}\int_0^{2\pi}\int_0^1 \frac{\hat{r}\cos\hat{\theta}-r}{(\hat{r}^2+r^2-2\hat{r}r\cos\hat{\theta}+\Delta h^2)^{3/2}} \cdot\hat{\rho}(\hat{r},\hat{h})\hat{r}\mathrm{d}\hat{r}\mathrm{d}\hat{\theta}\mathrm{d}\hat{h}\,. \quad (A.1)$$

The centrifugal force can be written simply as

$$F_c = \frac{V^2}{R} = \frac{V_0^2}{R_g}\frac{v(r,h)^2}{r}. \quad (A.2)$$

Here, we made all the variables dimensionless by measuring the distances in units of the outermost galactic radius R_g, mass density $\hat{\rho}$ in units of M_g/R_g^3, where M_g is the total galactic mass and velocities in units of the characteristic velocity V_0. So the balance between the gravitational and centrifugal force yields

$$\int_{-H/2}^{H/2}\int_0^{2\pi}\int_0^1 \frac{\hat{r}\cos\hat{\theta}-r}{(\hat{r}^2-r^2-2r\hat{r}\cos\hat{\theta}+\Delta h^2)^{3/2}}\hat{\rho}(\hat{r},\hat{h})\hat{r}\mathrm{d}\hat{r}\mathrm{d}\hat{\theta}\mathrm{d}\hat{h} + A\frac{v(r,h)^2}{r} = 0\,, \quad (A.3)$$

where A is the galactic rotation number

$$A = \frac{R_g V_0^2}{GM_g}. \quad (A.4)$$

We get rid of $\hat{\theta}$ dependency by simplifying the integral

$$I(r,\hat{r},\Delta h) = \int_0^{2\pi}\frac{\hat{r}\cos\hat{\theta}-r}{(\hat{r}^2-r^2-2r\hat{r}\cos\hat{\theta}+\Delta h^2)^{3/2}}\mathrm{d}\hat{\theta} \quad (A.5)$$

using complete elliptic integrals of first and second kind. Gradshteyn et al. (2007, pages 179 & 182) give the solution to these integrals

$$I_1 = \int\frac{\mathrm{d}x}{(a-b\cos x)^{1/2}} = \frac{2}{\sqrt{a+b}}F(\delta,k)\,; \quad (A.6)$$

$$I_3 = \int\frac{\mathrm{d}x}{(a-b\cos x)^{3/2}} = \frac{2}{(a-b)\sqrt{a+b}}E(\delta,k)\,, \quad (A.7)$$

where

$$x\in[0,\pi];\sin\delta = \sqrt{\frac{(a+b)(1-\cos\Phi)}{2(a-b\cos\Phi)}}; \quad (A.8)$$

$$k = \sqrt{\frac{2b}{a+b}}; a>b>0; \Phi\in[0,\pi]\,. \quad (A.9)$$

$F(\delta,k)$ and $E(\delta,k)$ are the incomplete elliptic integrals of the first and second kind

$$F(\delta,k) = \int_0^\delta\frac{\mathrm{d}\phi}{\sqrt{1-k^2\sin^2\phi}};$$
$$E(\delta,k) = \int_0^\delta\sqrt{1-k^2\sin^2\phi}\,\mathrm{d}\phi\,. \quad (A.10)$$

For the angle $\delta=\pi/2$, we obtain complete elliptic integrals that we can rewrite by substituting $t=\sin\phi$ as

$$K(k)\equiv F\left(\frac{\pi}{2},k\right) = \int_0^1\frac{\mathrm{d}t}{\sqrt{(1-t^2)(1-k^2t^2)}};$$
$$E(k)\equiv E\left(\frac{\pi}{2},k\right) = \int_0^1\sqrt{\frac{1-k^2t^2}{1-t^2}}\mathrm{d}t. \quad (A.11)$$

When we plug our values:

$$a = r^2+\hat{r}^2+\Delta h^2; b = 2r\hat{r} \quad (A.12)$$

to the Eq. (A.3), we get Eq. (14):

$$\int_{-H/2}^{H/2}\int_{R_{\min}}^{R_{\max}}\frac{2}{r}\left[\frac{(\hat{r}+r)(\hat{r}-r)+\Delta h^2}{[(\hat{r}-r)^2+\Delta h^2]\sqrt{(\hat{r}+r)^2+\Delta h^2}}E(k) - \frac{1}{\sqrt{(\hat{r}+r)^2+\Delta h^2}}K(k)\right]\rho_0 e^{-\hat{r}/h_R}e^{-|h|/h_z}\hat{r}\,\mathrm{d}\hat{r}\mathrm{d}h + A\frac{v_{c,\mathrm{disk}}(r,h)^2}{r} = 0\,.$$

4

Detection of Galactic warp precession

In this chapter, we further analyse the Galactic warp, in particular its precession. It is a well-known fact that rigid bodies can precess; the Earth's rotational axis, for example, precesses with a period of around 26 000 years. The same effect is expected to occur for the warp of the Milky Way: it was predicted that its line of nodes should change its orientation over time. However, the amount of precession predicted by various models is quite low and practically undetectable. This view was challenged recently when warp precession was measured for the first time by Poggio et al. (2020), who observed a value corresponding to about one-third of the angular rotation velocity at the Sun's position in the Galaxy, which is larger than earlier predictions by an order of magnitude, thus defying our current understanding of the warp.

We take a closer look at this intriguing new discovery and confront it with our findings. We have already shown in Chapter 2 that the warp amplitude is strongly dependent on the age of a given population. This plays an important role when calculating the warp precession.

The model that Poggio et al. (2020) consider was derived using Cepheids, which is a peculiar stellar population that does not represent the average population of the disc. Moreover, this population is very young (tens of Myr); therefore, its warp amplitude is significantly larger than that of the whole stellar population. On the other hand, our warp model presented in Chapter 2 is based on star counts from Gaia DR2 and thus represents the whole stellar population, and its amplitude is much smaller than previously thought. When we calculate the warp precession by applying our model, we find an interesting

result: there is no need for high precession, the observed velocities can also be explained by a non-precessing model. However, our work does not completely exclude the results of Poggio et al. (2020) either. As our precession estimate has very high error bars, it is impossible for us to differentiate between a precessing and a non-precessing model. This occurs because we calculate the distance from parallax, which has certain initial errors that propagate in subsequent calculations. As Poggio et al. (2020) used Cepheids for their model, they do not struggle with the same issue, since the distances of Cepheids are calculated with a different and more precise method. We therefore conclude that, with the current data precision, it is impossible to distinguish between a precessing and a non-precessing model, and we can neither exclude nor support any theory of warp formation based on this result.

This work was published in the following article:
The Astrophysical Journal (2021), 'A case against a significant detection of precession in the Galactic warp', **912**, 130.
A copy of the article is attached in the following pages.

The Astrophysical Journal, 912:130 (9pp), 2021 May 10 https://doi.org/10.3847/1538-4357/abf356

A Case against a Significant Detection of Precession in the Galactic Warp

Ž. Chrobáková[1,2] and M. López-Corredoira[1,2]
[1] Instituto de Astrofísica de Canarias, E-38205 La Laguna, Tenerife, Spain
[2] Departamento de Astrofísica, Universidad de La Laguna, E-38206 La Laguna, Tenerife, Spain
Received 2020 December 15; revised 2021 March 24; accepted 2021 March 25; published 2021 May 13

Abstract

Recent studies of warp kinematics using Gaia DR2 data have produced detections of warp precession for the first time, which greatly exceeds theoretical predictions of models. However, this detection assumes a warp model derived for a young population (few tens of megayears) to fit velocities of an average older stellar population of the thin disk (several gigayears) in Gaia-DR2 observations, which may lead to unaccounted systematic errors. Here, we recalculate the warp precession with the same approach and Gaia DR2 kinematic data, but using different warp parameters based on the fit of star counts of the Gaia DR2 sample, which has a much lower warp amplitude than the young population. When we take into account this variation of the warp amplitude with the age of the population, we find that there is no need for precession. We find the value of warp precession $\beta = 4^{+6}_{-4}$ km s^{-1} kpc^{-1}, which does not exclude nonprecessing warp.

Unified Astronomy Thesaurus concepts: Milky Way disk (1050); Milky Way Galaxy (1054)

1. Introduction

Although the warp was discovered over 60 yr ago (Kerr 1957; Oort et al. 1958) and extensively studied in the past decades (Carney & Seitzer 1993; López-Corredoira et al. 2002b; Amôres et al. 2017; Chen et al. 2019, and others), the mechanism causing the warp is still unknown. Theories include accretion of intergalactic matter onto the disk (López-Corredoira et al. 2002a), interaction with other satellites (Kim et al. 2014), the intergalactic magnetic field (Battaner et al. 1990), a misaligned rotating halo (Debattista & Sellwood 1999), and others.

Kinematic studies are necessary in order to reveal the origin of the warp, as different models give different predictions. Warp precession is estimated by various mechanisms of warp formation, such as torque of the dark halo on the disk (Dubinski & Chakrabarty 2009), torque on the disk due to misalignment of the halo and the disk (Jiang & Binney 1999), or accretion of intergalactic matter onto the disk (López-Corredoira et al. 2002a; Jeon et al. 2009).

Recently, studies of warp kinematics and time evolution were made in order to understand the origin of the warp (Poggio et al. 2018, 2020; Wang et al. 2020). In particular, the result of Poggio et al. (2020, hereafter P20) is of great interest as they measured the precession of the Galactic warp for the first time. Using the second Gaia data release DR2 (Gaia Collaboration et al. 2016, 2018) combined with Two Micron All-Sky Survey (Skrutskie et al. 2006, 2MASS) photometry, they find the warp precession to be $\beta = 10.86 \pm 0.03$(stat.) ± 3.20(syst.) km s^{-1} kpc^{-1}. Their result was supported by another recent work of Cheng et al. (2020), who measured a similar value of precession $\beta = 13.57^{+0.20}_{-0.18}$ km s^{-1} kpc^{-1} by fitting vertical velocities using data from Gaia DR2 and Apache Point Observatory Galactic Evolution Experiment 2 (Majewski et al. 2017, APOGEE-2), as contained in Sloan Digital Sky Survey (SDSS) Data Release 16 (Ahumada et al. 2020, DR16). These results greatly exceed predictions of warp precession estimated considering various mechanisms of warp formation, such as torque of the dark halo on the disk (Dubinski & Chakrabarty 2009), torque on the disk due to misalignment of the halo and the disk (Jiang & Binney 1999), or accretion of intergalactic matter onto the disk (López-Corredoira et al. 2002a; Jeon et al. 2009). All these works predict a small value of precession, between 0.1 and 1.5 km s^{-1} kpc^{-1}. The result of P20 contradicts conclusions of dynamical models of warp formation and suggests that warp is a transient response of the disk to an outside interaction rather than a slowly evolving structure. We know that most spiral galaxies have warps (Reshetnikov & Combes 1998; Sánchez-Saavedra et al. 2003), so it seems unlikely that the warp is caused by a transient phenomenon in all of them unless they all have a substructure that triggers warp formation very often.

Kinematics studies also discovered significant substructures in the disk velocities (Wang et al. 2018; López-Corredoira et al. 2020; Xu et al. 2020). In López-Corredoira et al. (2020) it is shown that the features in vertical motions can be partially explained by the warp; however, the main observed features can only be explained in terms of out-of-equilibrium models. Nevertheless, our purpose in this paper is not to explain all the features of the observed velocities, but just to verify that a simple warp model without precession is able to fit the data, against the claims of P20. Therefore, we will consider the substructures as random fluctuations and focus only on the large structural effect of the warp.

In this work, we challenge the result of P20, as we think they did not consider the variation of the amplitude of the warp with the age of the population, and present our own calculation of the warp precession rate. P20 derived the warp precession under an assumption that the amplitude of the warp corresponding to specific stellar populations (Classical Cepheids, Pulsars) is representative of the whole population. This is not consistent with data, as the stellar population traced by the Gaia survey is significantly older on average (∼5–6 Gyr) and it presents a much lower amplitude of the warp than the young population one (Chrobáková et al. 2020; Wang et al. 2020). For simplicity, we will refer to this population as an "old population" and to Cepheids as a "young population." We show that when applying the warp model for an old population we cannot detect the precession of the warp; therefore, we cannot favor any model of warp formation.

2. Data Selection

We use the data of López-Corredoira & Sylos-Labini (2019, hereafter LS19), who have produced extended kinematic maps of the Milky Way by using Gaia DR2, by considering stars with measured radial heliocentric velocities and with parallax errors less than 100%; the total sample contains 7,103,123 sources. Such objects were observed by the Radial Velocity Spectrometer (RVS; Cropper et al. 2018) that collects medium-resolution spectra (spectral resolution $\frac{\lambda}{\Delta\lambda} \approx 11700$) over the wavelength range 845–872 nm, centered on the Calcium triplet region. Radial velocities are averaged over a 22 month time span of observations. Most sources have a magnitude brighter than 13 in the G filter.

In more detail, the effective temperatures for the sources with radial velocities that LS19 have considered are in the range of 3550 to 6900 K. The uncertainties of the radial velocities are 0.3 km s^{-1} at $G_{\rm RVS} < 8$, 0.6 km s^{-1} at $G_{\rm RVS} = 10$, and 1.8 km s^{-1} at $G_{\rm RVS} = 11.75$; plus systematic radial velocity errors of <0.1 km s^{-1} at $G_{\rm RVS} < 9$ and 0.5 km s^{-1} at $G_{\rm RVS} = 11.75$. The uncertainties of the parallax are 0.02–0.04 mas at $G < 15$, 0.1 mas at $G = 17$, 0.7 mas at $G = 20$, and 2 mas at $G = 21$. The uncertainties of the proper motion are 0.07 mas yr^{-1} at $G < 15$, 0.2 mas yr^{-1} at $G = 17$, 1.2 mas yr^{-1} at $G = 20$, and 3 mas yr^{-1} at $G = 21$. For details on radial velocity data processing and the properties and validation of the resulting radial velocity catalog, see Sartoretti et al. (2018) and Katz et al. (2019). The set of standard stars that was used to define the zero-point of the RVS radial velocities is described in Soubiran et al. (2018). LS19 consider the zero-point bias in the parallaxes of Gaia DR2, as found by Lindegren et al. (2018), Arenou et al. (2018), Stassun & Torres (2018), and Zinn et al. (2019); however, they find that the effect of the systematic error in the parallaxes is negligible.

As the parallax error grows as the distance from us grows, LS19 applied a statistical deconvolution of the parallax errors based on Lucy's inversion method (Lucy 1974) to statistically estimate the distance. In this way they have derived the extended kinematical maps in the range of Galactocentric distances up to 20 kpc.

From this sample, we only choose stars with the Galactic latitude $|b| < 10°$, Galactocentric distance $R > 12$ kpc, and heliocentric distance $r < 8$ kpc, so we obtain a data set with Galactocentric radius $12 < R < 16$ kpc, maximum vertical distance $z \approx 1.4$ kpc, and within $|\phi| < 40°$, as seen from the Galactic center. We bin the data in Galactocentric Cartesian coordinates with size $\Delta X = 1.0$ kpc and $\Delta Y = 1.0$ kpc. For $R < 12$ kpc, the amplitude of the warp is too small to be considered and the relative error of the warp model is higher. For $r > 8$ kpc, the errors of vertical velocities are very large.

3. Methods

We model the warp in Galactocentric cylindrical coordinates (R, ϕ, z) using the warp model of Chrobáková et al. (2020, Equation (11)) for which the average height over the plane of the Galactic disk stars z_w is calculated as

$$z_w = [C_w R(pc)^{\epsilon_w} \sin(\phi - \phi_w) + 17]\ \text{pc}. \quad (1)$$

The model describes the warp as a series of tilted rings, where the amount of tilt is the Galactocentric distance raised to a power of ϵ_w. C_w is the warp amplitude, and ϕ_w is the Galactocentric angle defining the warp's line of nodes. C_w, ϵ_w, and ϕ_w are free parameters of the model, which were fitted in Chrobáková et al. (2020). The 17 pc term compensates for the elevation of the Sun above the plane (Karim & Mamajek 2017). We consider time evolution of the warp amplitude and warp precession

$$C_w(t) = C_{w,\max} \sin(\omega t + \alpha), \quad (2)$$

$$\phi_w(t) = \phi_{w0} + \beta t. \quad (3)$$

The values of model parameters given by Chrobáková et al. (2020) are

$$\begin{aligned} C_w &= 1.17 \cdot 10^{-8}\ \text{pc} \pm 1.34 \cdot 10^{-9}\ \text{pc(stat.)} \\ &\quad \times {}^{+0\text{pc}}_{-2.9\cdot10^{-10}\ \text{pc}}\text{(syst.)}, \\ \epsilon_w &= 2.42 \pm 0.76\text{(stat.)}^{\pm 0.129}_{-0}\text{(syst.)}, \\ \phi_w &= -9.31° \pm 7.37°\text{(stat.)}^{\pm 4.48°}_{0°}\text{(syst.)}. \end{aligned} \quad (4)$$

We follow the approach of P20, taking the zeroth moment of the collisionless Boltzmann equation to derive the expression for vertical velocity.

$$\begin{aligned} v_z(R, \phi) &= C_{w,0} K R^{\epsilon_w} \sin(\phi - \phi_{w,0}) \\ &\quad - C_{w,0} R^{\epsilon_w} \beta \cos(\phi - \phi_{w,0}) \\ &\quad + C_{w,0} R^{\epsilon_w - 1} \cos(\phi - \phi_{w,0}) v_\phi, \end{aligned} \quad (5)$$

where $C_{w,0}$ and $\phi_{w,0}$ are Equations (2) and (3) at present time t and

$$K = \omega \cdot \text{cotan}(\alpha). \quad (6)$$

We use the least-squares method, to fit the data, minimizing χ^2:

$$\chi^2 = \sum_i \frac{(v_{Z,i}^{\rm obs} - v_{Z,i}^{\rm model})^2}{\sigma_i^2}. \quad (7)$$

López-Corredoira & Sylos-Labini (2019) give their data in coordinates (X,Y) binned with size $\Delta X = 0.2$ kpc and $\Delta Y = 0.2$ kpc. To avoid confusion, we will refer to those bins as pixels. Each bin with average velocity $v_{Z,i}^{\rm obs}$ is generated by grouping different pixels (X,Y) into squares of 1 kpc × 1 kpc with the same number of pixels for all bins, where σ_i^2 is the error of velocity in each bin:

$$\sigma_i^2 = \frac{\sum_{j\in i} w_j \sigma_{Z,j}^2}{\sum_{j\in i} w_j}, \quad (8)$$

where $\sigma_{Z,j}$ is the error of velocity in the pixel j, and w_j is its weight (number of stars in our case).

Errors in the bin can be calculated differently, depending on whether the statistical or systematic error dominates. We tried to calculate the error using different approaches, but we find that the results are similar in all cases. More about error estimation can be found in Section 4.3.

4. Results

4.1. Old Population Warp Does Not Give Precession

We fit the vertical velocities with a warp model considering both the evolution in time of the warp amplitude and the warp precession. As a first case, we only take data with azimuth $|\phi| < 10°$ (near the anticenter), where the dependence of amplitude on time is negligible, as can be seen from Equation (5), when we set the value of the angle of the line of nodes. Therefore we only have one free parameter β that represents precession of the warp

The Astrophysical Journal, 912:130 (9pp), 2021 May 10

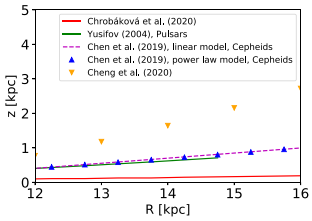

Figure 1. Comparison of maximum amplitudes of various warp models, used to calculate the precession. It is evident that the model of Chrobáková et al. (2020), derived for the whole stellar population, reaches a significantly lower amplitude than other works.

azimuth of the line of nodes (see Equation (3)). We carry out the fit for the model of Chrobáková et al. (2020) and the model of P20 using the warp parameters of the linear model of Chen et al. (2019). Differences in maximum amplitude for these warp models can be seen in Figure 1. In Figure 2(a) we show the best fit and the nonprecessing warp for the model of P20. It is clear that, with the high amplitude, the nonprecessing model gives much higher velocity than what is observed, so a high precession is necessary to compensate for that. That is precisely the result of P20. In contrast, the warp model representative of the old stellar population of Gaia DR2 (Chrobáková et al. 2020) reaches about 3–4 times lower amplitude than the one used by P20 (see Figure 1); therefore, it does not need a high precession.

As shown in Figure 2(b), with a nonprecessing warp the amplitude of the velocity is already of the order of the data and the precession gives only a small correction. The value of precession we obtain with the model used by P20 is $\beta = 13 \pm 1$ km s^{-1} kpc^{-1}, which is similar, although a bit higher than the value obtained by P20 ($\beta = 10.86 \pm 0.03$ (stat.) $\pm$ 3.20(syst.) km s^{-1} kpc^{-1}), probably due to difference in data sets. The value of precession using the old stellar population of Gaia DR2 is $\beta = -1 \pm 9$ km s^{-1} kpc^{-1}, which is consistent with the nonprecessing warp model, as well as with the result of P20, since we have large error bars. P20 already pointed out that a warp model with a small amplitude like ours would fit the data without the need for precession; however, they do not carry out the analysis with such a model and do not provide a result of such fit; therefore, we cannot compare our result with theirs directly.

Next, we do the fit for all the azimuths, with the complete model (Equation (5)), including precession and time variation of the warp amplitude. Variation of the warp amplitude may in fact be more relevant than the precession term (López-Corredoira et al. 2014, 2020). For warp parameters of Chrobáková et al. (2020), we find the best fit to be for $K = 16^{+12}_{-8}$ km s^{-1} kpc^{-1} and $\beta = 4^{+6}_{-4}$ km s^{-1} kpc^{-1}. For comparison, we did the same fit using the warp parameters of the linear model of Chen et al. (2019) that P20 used. This yields best-fit parameters $K = 1.0^{+1.4}_{-2.2}$ km s^{-1} kpc^{-1} and $\beta = 14.0 \pm 1.4$ km s^{-1} kpc^{-1}. Similar numbers are obtained with other warp models used by P20 or by calculating errors in a different way (see Table 1). The results of this fit can be seen in Figures 3 and 4, where we find the same trend as in the anticenter. With the warp parameters of Chen et al. (2019) there is the need for a high precession to fit the data, whereas when we use the warp model of Chrobáková et al. (2020), the nonprecessing steady warp is of the order of magnitude of the data. For the data, there is some substructure in velocity, but as we mention in Section 1, we are not attempting here to explain all the velocity substructures, but to analyze the overall effect of the warp.

The difference between the warp model of Chen et al. (2019) and the model of Chrobáková et al. (2020) is that the first one was derived for a very young stellar population of Classical Cepheids, whereas the second one was calculated for the whole population traced by Gaia DR2, which is much older on average. Our results using the model of young population warp used by P20 with our data set are in agreement with their findings. However, when we apply warp parameters of the whole population, we cannot detect the precession. Since we have a large value of precession error, we cannot refute the result of P20, but we cannot reject the nonprecessing warp either. Since the error of the precession comes mostly from the propagation of the warp parameters (see Section 4.3), we believe that the effect of error propagation is stronger than the error of the fits of velocities and we would need more precise data to be able to detect precession.

4.2. Different Warp Models

P20 also use other warp parameters such as from Yusifov (2004) and López-Corredoira et al. (2002b). However, these models are not representative of the whole Gaia DR2 population either. The warp parameters of Yusifov (2004) were derived for pulsars only; therefore, they should not be applied to the whole population. Plus their parameters were derived only for Galactocentric distances $R \approx 15$ kpc. Although P20 argue that Momany et al. (2006) found that the Yusifov (2004) model describes the red-giant branch stars, a population similar to that of P20, well, we do not think that that makes it applicable in the case of P20 for the following reason. Momany et al. (2006) do not have a 3D distribution of data, but a 2D projection at a fixed distance. Their data get well fitted by the Yusifov (2004) model because Yusifov (2004) measures a high value of the warp line of nodes, which describes the data projection of Momany et al. (2006) well, but that does not imply that it describes the real 3D distribution of data as well. Chrobáková et al. (2020) applied the Yusifov (2004) warp parameters on the whole Gaia DR2 data set and we found that it leads to high warp amplitude, which is not in agreement with the warp amplitude of the whole population.

The parameters of López-Corredoira et al. (2002b) were derived for the red-clump stars, but these parameters were derived only for Galactocentric distances up to $R \approx 13$ kpc; therefore, extrapolating them at higher distances is unreliable and leads to unrealistic warp amplitude.

In Figure 1, we show that the maximum amplitude of models used by P20 is quite similar, whereas the warp amplitude derived by Chrobáková et al. (2020) is lower by a factor of $\approx$3–4. The result of fits with other models can be seen in Table 1.

4.3. Calculation of Error Bars

Determining the error of v_Z is not an easy task, as in the data, the systematic and statistical error are entangled and we cannot

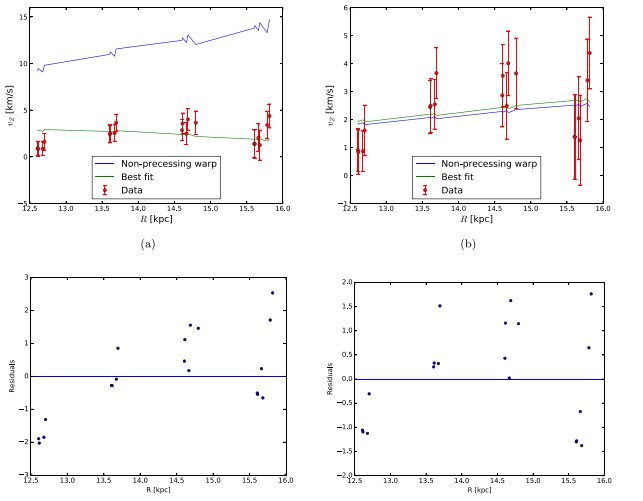

Figure 2. Result of the fit with warp models, using only data near the anticenter. The blue curve is for the nonprecessing model of the warp ($\beta = 0$ km s^{-1} kpc^{-1}), the green curve is the best fit of the data. (a) Model of P20, with the warp parameters of Chen et al. (2019). For the best fit, we find $\beta = 13 \pm 1$ km s^{-1} kpc^{-1}. (b) Model of Chrobáková et al. (2020). For the best fit, we find $\beta = 1 \pm 9$ km s^{-1} kpc^{-1}. (c) Residuals corresponding to the model of P20, with warp parameters of Chen et al. (2019). (d) Residuals corresponding to the model of Chrobáková et al. (2020).

differentiate between them. Therefore, we tried several approaches to calculate the error. In each case, we normalize the error bars in order to obtain $\chi^2_\nu = 1.0$ for the case of nonprecessing warp in the line of nodes, using warp parameters of Chrobáková et al. (2020). The factor f in Table 1 is precisely introduced for this normalization, and it should be approximately $f = 1/\sqrt{N}$ for the case of statistical errors and $f = 1$ for the case of purely systematical errors. From the error of velocity, we can then calculate the error of fit parameters.

Another contribution to the error comes from the propagation of error of warp parameters. To determinate the error bars of β and K we made Monte Carlo simulations. The systematic and statistical error of the warp parameters (Equation (4)) was summed linearly. It is important to notice that for the warp model of Chrobáková et al. (2020) this contribution to the error is the dominant one and causes the error bars to be significant. For illustration purposes, we show corner plots of Monte Carlo simulations for the linear model of Chen et al. (2019) and Chrobáková et al. (2020) in Figure 5, using only data near the anticenter. We use the maximum spread of the values of β to determine the error bars of the precession. It is clear that for the model of Chrobáková et al. (2020) the spread of values of precession is very large, which impedes determining the precession more accurately, whereas for the model of Chen et al. (2019), the spread is far smaller.

Finally we summed quadratically the error of the fit and error produced by the uncertainties of warp parameters to determine the final error of the fit parameters β and K. The values are given in Table 1, where each model is given for a different determination of velocity error bar. These various approaches give similar results.

4.4. Non-Gaussian Residuals of Least-squares Fit

In Figures 2, 3, and 4, we can see that the residuals of the least-squares fitting are not completely Gaussian, especially for the case of the warp model of Chrobáková et al. (2020) the residuals are skewed. To account for this effect, we performed one of the fits using Python's method curve fit from the Scipy package. This fitting method has implemented several loss functions that we can apply to perform a more robust fit with

Table 1
Results of Fit with Various Warp Models and Error Calculations

Model of Error	Conditions of the Fit	Chrobáková et al. (2020) (km s^{-1} kpc^{-1})	Chen et al. (2019), Linear Model (km s^{-1} kpc^{-1})	Chen et al. (2019), Power Model (km s^{-1} kpc^{-1})	Yusifov (2004) (km s^{-1} kpc^{-1})
	$-10° < \phi < 10°$, $\beta = 0$	$\chi^2_\nu = 1.03$	$\chi^2_\nu = 81.54$	$\chi^2_\nu = 78.57$	$\chi^2_\nu = 62.51$
	$-10° < \phi < 10°$, β free	$\beta = -1 \pm 9$, $\chi^2_\nu = 1.00$	$\beta = 13 \pm 1$, $\chi^2_\nu = 1.8$	$\beta = 13 \pm 1$, $\chi^2_\nu = 1.77$	$\beta = 13 \pm 1$, $\chi^2_\nu = 1.83$
Model 1	$\forall\phi$, $K = 0$, $\beta = 0$	$\chi^2_\nu = 1.94$	$\chi^2_\nu = 76.33$	$\chi^2_\nu = 73.55$	$\chi^2_\nu = 61.45$
	$\forall\phi$, $K = 0$, β free	$\beta = 2^{+5}_{-4}$, $\chi^2_\nu = 1.86$	$\beta = 14 \pm 1$, $\chi^2_\nu = 2.82$	$\beta = 14 \pm 1$, $\chi^2_\nu = 2.86$	$\beta = 14 \pm 1$, $\chi^2_\nu = 2.88$
	$\forall\phi$, $\beta = 0$, K free	$K = 11^{+12}_{-7}$, $\chi^2_\nu = 1.75$	$K = 22 \pm 1$, $\chi^2_\nu = 43.79$	$K = 22 \pm 1$, $\chi^2_\nu = 41.98$	$K = 21 \pm 1$, $\chi^2_\nu = 40.87$
	$\forall\phi$, K free, β free	$\beta = 4^{+6}_{-4}$, $K = 16^{+21}_{-8}$, $\chi^2_\nu = 1.56$	$\beta = 14 \pm 1$, $K = 1.0^{+1.5}_{-1.0}$, $\chi^2_\nu = 2.83$	$\beta = 13 \pm 1$, $K = 2.0 \pm 1.4$, $\chi^2_\nu = 2.81$	$\beta = 13 \pm 1$, $K = 2 \pm 1$, $\chi^2_\nu = 2.85$
	$-10° < \phi < 10°$, $\beta = 0$	$\chi^2_\nu = 1.05$	$\chi^2_\nu = 84.70$	$\chi^2_\nu = 81.79$	$\chi^2_\nu = 64.74$
	$-10° < \phi < 10°$, β free	$\beta = -1^{+7}_{+9}$, $\chi^2_\nu = 1.00$	$\beta = 13 \pm 1$, $\chi^2_\nu = 1.71$	$\beta = 13 \pm 1$, $\chi^2_\nu = 1.68$	$\beta = 13 \pm 1$, $\chi^2_\nu = 1.71$
Model 2	$\forall\phi$, $K = 0$, $\beta = 0$	$\chi^2_\nu = 2.30$	$\chi^2_\nu = 90.32$	$\chi^2_\nu = 87.23$	$\chi^2_\nu = 73.74$
	$\forall\phi$, $K = 0$, β free	$\beta = 3^{+5}_{-4}$, $\chi^2_\nu = 2.09$	$\beta = 14 \pm 1$, $\chi^2_\nu = 3.31$	$\beta = 14 \pm 1$, $\chi^2_\nu = 3.34$	$\beta = 14 \pm 1$, $\chi^2_\nu = 3.40$
	$\forall\phi$, $\beta = 0$, K free	$K = 8^{+14}_{-4}$, $\chi^2_\nu = 2.18$	$K = 21 \pm 1$, $\chi^2_\nu = 54.77$	$K = 21 \pm 1$, $\chi^2_\nu = 52.62$	$K = 20 \pm 1$, $\chi^2_\nu = 51.19$
	$\forall\phi$, K free, β free	$\beta = 6^{+8}_{-6}$, $K = 15^{+31}_{-7}$, $\chi^2_\nu = 1.79$	$\beta = 14 \pm 1$, $K = 1.0 \pm 1.4$, $\chi^2_\nu = 3.23$	$\beta = 14 \pm 1$, $K = 1.0 \pm 1.4$, $\chi^2_\nu = 3.21$	$\beta = 14 \pm 1$, $K = 2^{+3}_{-2}$, $\chi^2_\nu = 3.26$
	$-10° < \phi < 10°$, $\beta = 0$	$\chi^2_\nu = 1.93$	$\chi^2_\nu = 81.83$	$\chi^2_\nu = 78.99$	$\chi^2_\nu = 61.57$
	$-10° < \phi < 10°$, β free	$\beta = -2^{+10}_{+8}$, $\chi^2_\nu = 1.00$	$\beta = 13 \pm 1$, $\chi^2_\nu = 1.54$	$\beta = 13 \pm 1$, $\chi^2_\nu = 1.53$	$\beta = 13 \pm 1$, $\chi^2_\nu = 1.63$
Model 3	$\forall\phi$, $K = 0$, $\beta = 0$	$\chi^2_\nu = 2.05$	$\chi^2_\nu = 77.50$	$\chi^2_\nu = 74.69$	$\chi^2_\nu = 61.72$
	$\forall\phi$, $K = 0$, β free	$\beta = 1^{+10}_{-10}$, $\chi^2_\nu = 1.99$	$\beta = 14 \pm 1$, $\chi^2_\nu = 2.91$	$\beta = 14 \pm 1$, $\chi^2_\nu = 2.96$	$\beta = 14 \pm 1$, $\chi^2_\nu = 3.01$
	$\forall\phi$, $\beta = 0$, K free	$K = 12 \pm 13$, $\chi^2_\nu = 1.80$	$K = 21 \pm 1$, $\chi^2_\nu = 45.22$	$K = 21 \pm 1$, $\chi^2_\nu = 43.34$	$K = 21 \pm 1$, $\chi^2_\nu = 41.65$
	$\forall\phi$, K free, β free	$\beta = 4^{+6}_{-4}$, $K = 17^{+7}_{-4}$, $\chi^2_\nu = 1.63$	$\beta = 13 \pm 1$, $K = 2.0 \pm 1.4$, $\chi^2_\nu = 2.83$	$\beta = 13 \pm 1$, $K = 2.0 \pm 1.4$, $\chi^2_\nu = 2.80$	$\beta = 13 \pm 1$, $K = 2 \pm 1$, $\chi^2_\nu = 2.85$

Note. Model 1: error calculated as $\sigma_i^2 = f \cdot \frac{\sum_i w_i \sigma_{\beta,i}^2}{\sum_i w_i}$, quadratically combined with the error propagated from warp parameters. Model 2: error calculated as $\sigma_i^2 = f \cdot \frac{\sum_i w_i (\sigma_{\beta,i} - \overline{\sigma_{\beta,i}})^2}{\sum_i w_i}$, quadratically combined with the error propagated from warp parameters. Model 3: error calculated as $\sigma_i^2 = f \cdot \frac{1}{\sqrt{\sum_i \frac{1}{\sigma_{\beta,i}^2}}}$, $\chi^2_\nu = \sum_i \frac{(\sigma_{\beta,i} - \overline{\sigma_{\beta,i}})^2}{\sigma_{\beta,i}^2}$, quadratically combined with the error propagated from warp parameters. For the warp model of Chrobáková et al. (2020), the propagation of warp parameters is the dominant component of the error. In all cases, f is such that $\chi^2_\nu(-10° < \phi < 10°;$ Chrobáková et al. (2020)$) = 1.00$ for the best fit.

The Astronomical Journal, 912:130 (9pp), 2021 May 10

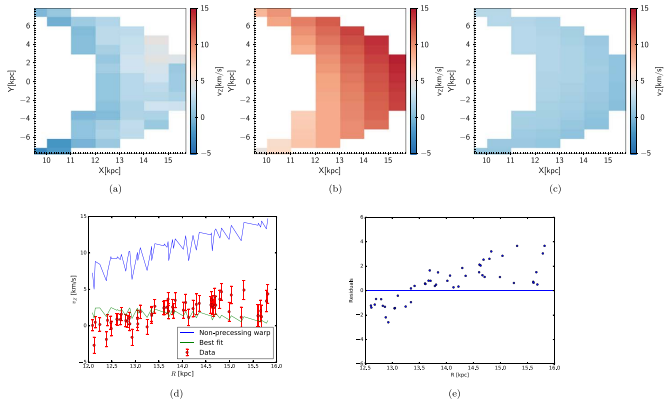

Figure 3. Result of fit using Equation (5) with parameters of Chen et al. (2019), fitting all data. (a) Data. (b) Nonprecessing steady warp ($\beta = 0$ km s^{-1} kpc^{-1} and $K = 0$ km s^{-1} kpc^{-1}). (c) Best fit with K and β as free parameters. For the best fit, we find $K = 1.0^{+1.4}_{-1.5}$ km s^{-1} kpc^{-1} and $\beta = 14.0 \pm 1.4$ km s^{-1} kpc^{-1}. (d) Two-dimensional representation of the fit. The blue curve is for the nonprecessing steady model of the warp, the green curve is for the best fit of the data. (e) Residuals corresponding to the best fit.

less sensitivity to outliers. In Figure 6 we show the comparison of the fit using a linear loss function that corresponds to the standard least-squares fit with more robust loss functions such as Huber's loss function and a smooth approximation of l1, which uses the sum of absolute deviations instead of squared ones (see Scipy documentation for more details). Change in the loss function influences the value of precession and the corresponding error, but compared to the error from the propagation of the warp parameters, this difference is insignificant; therefore, in all the cases we apply traditional least-squares as described in Section 3.

4.5. Comparison with Cheng et al. (2020)

The claims of P20 are supported in a recent paper of Cheng et al. (2020, hereafter C20), who used Gaia DR2 and APOGEE-2 DR16 to fit the warp from the kinematics. They use distances derived through Bayesian inference using the StarHorse code (Queiroz et al. 2018), which enables them to reach a high Galactocentric distance of $R = 18$ kpc . They observe a significant decrease in vertical velocity, which they attribute to the warp. They adopt a model including the precession of warp and leave all the warp parameters free, except the line of nodes. They find a high amplitude of warp and a high value of warp precession of $\beta = 13.57^{+0.20}_{-0.18}$ km s^{-1} kpc^{-1}, similar to the value of P20. This is in disagreement with our results, due to the drop in the vertical velocity, beginning at about $R \approx 13$ kpc. We do not observe this in our data. As can be seen in Figure 7, our data show a decrease in vertical velocity, starting at about $R \approx 17$ kpc. We are aware that our statistical method to calculate the distance can give rise to errors; however, from the horizontal error bars in Figure 7 we can see that up to $R \approx 16$ kpc the data is robust and the error of the distance determination starts to be significant at higher distances. Therefore even taking into account the error bars, the drop in velocity would manifest itself at higher distances than given by C20.

As a further attempt to find the origin of the discrepancy in the data, we repeated the analysis carried out by C20 with similar data. C20 use two different data sets. One is a combination of Gaia DR2 with StarHorse distances. We are not aware that C20 put any constraints on these data, except filtering out stars that have a problematic Gaia photometric or astrometric solution or a troublesome StarHorse data reduction and removing stars from the Large Magellanic Cloud (LMC) and Small Magellanic Cloud (SMC). Therefore we have to assume they include all ranges of Galactic latitudes in this sample, thus not avoiding contamination by thick disk and halo stars. The second data set of C20 combines Gaia DR2 with chemical and radial velocity information from APOGEE-2 DR16 and with StarHorse distances. C20 apply a constraint to this data set in [Fe/H] and [Mg/Fe] in order to choose only thin disk stars (see their Figure 1). For both data sets, C20 observe a drop in velocities, although for the second sample the drop is less prominent. The first sample of C20 should be similar to what we are using, except we only chose stars with $|b| < 10°$, which would explain the discrepancy. To reproduce the second sample, we used a publicly available data set of Queiroz et al. (2020) who combined spectroscopic data from

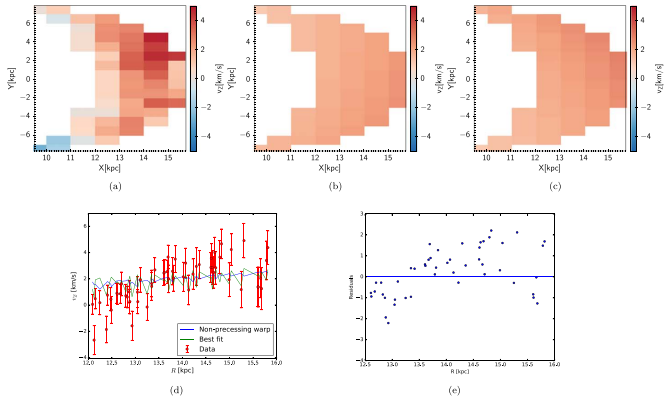

Figure 4. Result of fit using Equation (5) with parameters of Chrobáková et al. (2020), fitting all data. (a) Data. (b) Nonprecessing steady warp ($\beta = 0$ km s^{-1} kpc^{-1} and $K = 0$ km s^{-1} kpc^{-1}). (c) Best fit with K and β as free parameters. For the best fit, we find $K = 16^{+2}_{-2}$ km s^{-1} kpc^{-1} and $\beta = 4^{+2}_{-2}$ km s^{-1} kpc^{-1}. (d) Two-dimensional representation of the fit. The blue curve is for the nonprecessing steady model of the warp, the green curve is the best fit of the data. (e) Residuals corresponding to the best fit.

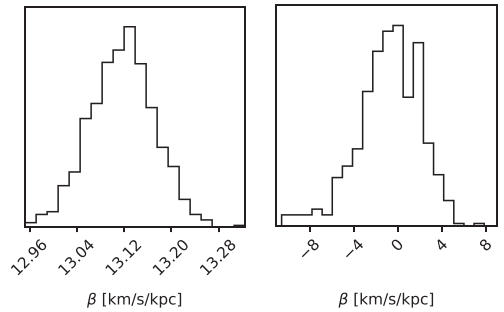

Figure 5. Corner plot of the Monte Carlo simulation using only data near the anticenter. Left: model of P20, with warp parameters of Chen et al. (2019). Right: model of Chrobáková et al. (2020).

APOGEE-2 DR16 with photometric data and parallaxes from Gaia DR2 and distances derived using Starhorse. We applied the same selection criteria as C20—we removed sources within 5° from the center of LMC and SMC, we restricted the effective temperature between 3700 K and 5500 K, and we applied the same constraint in [Fe/H] and [Mg/Fe]. Our data set is not exactly the same as the one of C20, but they should be in good agreement. However, upon applying the same

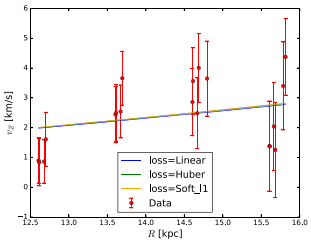

Figure 6. Comparison of the least-squares fit using different loss functions to treat outliers. We fit only data near the anticenter and we apply the warp model of Chrobáková et al. (2020). The linear loss function corresponds to the ordinary least-squares fit, where we obtain the value of precession $\beta = -1 \pm 1.8$ km s^{-1} kpc^{-1}. With a smooth approximation of l1 we obtain $\beta = -1.35 \pm 2.21$ km s^{-1} kpc^{-1} and with Huber's function we obtain $\beta = -1.07 \pm 1.81$ km s^{-1} kpc^{-1}. Note that in this case we only report the error of precession coming from the fit, not combined with the propagation of error of warp parameters, which is why the error is lower than in previous sections.

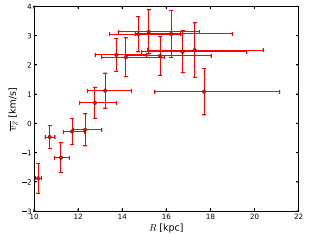

Figure 7. Average vertical velocity from Gaia DR2 including the complete range of azimuths. We do not observe a significant drop in velocity until $R \approx 17$ kpc. Due to large error bars, we constrain our analysis to $R < 16$ kpc.

conditions as C20, we do not observe a drop in velocities as C20 obtained. In fact, the velocity that we obtain is consistent with the velocity obtained when we applied our condition on the data, that is $|b| < 10°$ (see Figure 8). Therefore we do not know what the reason is behind the drop in vertical velocity found by C20, but we suspect there might be contamination by the thick disk and the halo stars. In order to fit the warp, C20 used the Gaia sample that was not constrained and C20 state they assume this sample is not contaminated because the velocity has similar behavior to that of the thin disk in the Gaia-APOGEE sample. Although in principle this method of constraining the thin disk should be correct, we doubt that a full Gaia DR2 sample chosen within $|b| = 90°$ has the same behavior of velocity as a strictly

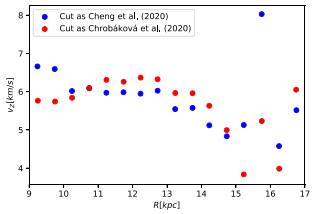

Figure 8. Average vertical velocity from Gaia DR2. For the blue curve we applied the same constraints as C20, most importantly a cut in [Fe/H] and [Mg/Fe] to choose only thin disk stars. For the red curve, we applied the same constraint as in our data, that is $|b| < 10°$. Contrary to C20, we do not observe a significant drop in velocity for either approach.

constrained thin disk sample of APOGEE. The fact that we cannot reproduce the drop in velocity at $R \approx 13$ kpc in either sample confirms this doubt, although we do not know with certainty what the reason is for this discrepancy.

C20 explain the drop in velocities solely in terms of warp and use only the vertical velocity to fit the warp parameters. We plot their warp amplitude in Figure 1, where we can see that their model yields far higher values than other works. We do not know if this result would be sustained by their stellar density, as C20 did not analyze the density distribution. However, Chrobáková et al. (2020) calculated warp parameters by fitting the stellar density and reaching a significantly lower warp amplitude.

Our argument is supported by other results in the literature as well, since most authors obtain far lower warp amplitude, between roughly 0.4–1 kpc at $R = 15$ kpc, depending on the stellar population and warp model (Yusifov 2004; Reylé et al. 2009; Chen et al. 2019; Li et al. 2019; Skowron et al. 2019). The only work that supports the result of Cheng et al. (2020) is the one of Amôres et al. (2017), who produced star counts using a population synthesis model (Besançon Galaxy Model); therefore, we think their results should be interpreted with care since they are model-dependent.

5. Conclusions

We studied the precession of the Galactic warp based on the model of P20 and present our own calculation. We are using vertical velocities of Gaia DR2 that represent the average kinematics of an old stellar population (~5–6 Gyr) and we apply a new warp model (Chrobáková et al. 2020), based on Gaia DR2. Our warp model has a significantly smaller amplitude than models used by P20, which are either derived for a young stellar population (~Myr) or an invalid extrapolation of an old stellar population warp. When we consider variation of the amplitude of the warp with the age of the population, we obtain a best fit that is compatible with no precession, taking into account the uncertainties in a warp model independently derived from an old stellar density distribution with the same Gaia data. Therefore we do not find evidence to support or exclude any model of warp formation. Future studies are necessary to understand kinematics of warp and thus its formation mechanism. The next Gaia data release DR3

could provide sufficiently precise data, to study the warp in greater detail and possibly detect the precession.

We thank E. Puha, H.-F. Wang, and R. Nagy for helpful comments. Ž.C. and M.L.C. were supported by the grant PGC-2018-102249-B-100 of the Spanish Ministry of Economy and Competitiveness (MINECO). This work has made use of data from the European Space Agency (ESA) mission Gaia (https://www.cosmos.esa.int/gaia), processed by the Gaia Data Processing and Analysis Consortium (DPAC, https://www.cosmos.esa.int/web/gaia/dpac/consortium). Funding for the DPAC has been provided by national institutions, in particular the institutions participating in the Gaia Multilateral Agreement. Funding for the Sloan Digital Sky Survey IV has been provided by the Alfred P. Sloan Foundation, the U.S. Department of Energy Office of Science, and the Participating Institutions.

SDSS-IV acknowledges support and resources from the Center for High Performance Computing at the University of Utah. The SDSS website is www.sdss.org.

SDSS-IV is managed by the Astrophysical Research Consortium for the Participating Institutions of the SDSS Collaboration including the Brazilian Participation Group, the Carnegie Institution for Science, Carnegie Mellon University, Center for Astrophysics | Harvard & Smithsonian, the Chilean Participation Group, the French Participation Group, Instituto de Astrofísica de Canarias, The Johns Hopkins University, Kavli Institute for the Physics and Mathematics of the Universe (IPMU)/University of Tokyo, the Korean Participation Group, Lawrence Berkeley National Laboratory, Leibniz Institut für Astrophysik Potsdam (AIP), Max-Planck-Institut für Astronomie (MPIA Heidelberg), Max-Planck-Institut für Astrophysik (MPA Garching), Max-Planck-Institut für Extraterrestrische Physik (MPE), National Astronomical Observatories of China, New Mexico State University, New York University, University of Notre Dame, Observatário Nacional/MCTI, The Ohio State University, Pennsylvania State University, Shanghai Astronomical Observatory, United Kingdom Participation Group, Universidad Nacional Autónoma de México, University of Arizona, University of Colorado Boulder, University of Oxford, University of Portsmouth, University of Utah, University of Virginia, University of Washington, University of Wisconsin, Vanderbilt University, and Yale University.

ORCID iDs

Ž. Chrobáková https://orcid.org/0000-0002-9895-6638
M. López-Corredoira https://orcid.org/0000-0001-6128-6274

References

Ahumada, R., Allende Prieto, C., Almeida, A., et al. 2020, ApJS, 249, 3
Amôres, E. B., Robin, A. C., & Reylé, C. 2017, A&A, 602, A67
Arenou, F., Luri, X., Babusiaux, C., et al. 2018, A&A, 616, A7
Battaner, E., Florido, E., & Sanchez-Saavedra, M. L. 1990, A&A, 236, 1
Carney, B. W., & Seitzer, P. 1993, AJ, 105, 2127
Chen, X., Wang, S., Deng, L., et al. 2019, NatAs, 3, 320
Cheng, X., Anguiano, B., Majewski, S. R., et al. 2020, ApJ, 905, 49
Chrobáková, Ž., Nagy, R., & López-Corredoira, M. 2020, A&A, 637, A96
Cropper, M., Katz, D., Sartoretti, P., et al. 2018, A&A, 616, A5
Debattista, V. P., & Sellwood, J. A. 1999, ApJ, 513, L107
Dubinski, J., & Chakrabarty, D. 2009, ApJ, 703, 2068
Gaia Collaboration, Brown, A. G. A., Vallenari, A., et al. 2018, A&A, 616, A1
Gaia Collaboration, Prusti, T., de Bruijne, J. H. J., et al. 2016, A&A, 595, A1
Jeon, M., Kim, S. S., & Ann, H. B. 2009, ApJ, 696, 1899
Jiang, I.-G., & Binney, J. 1999, MNRAS, 303, L7
Karim, M. T., & Mamajek, E. E. 2017, MNRAS, 465, 472
Katz, D., Sartoretti, P., Cropper, M., et al. 2019, A&A, 622, A205
Kerr, F. J. 1957, AJ, 62, 93
Kim, J. H., Peirani, S., Kim, S., et al. 2014, ApJ, 789, 90
Li, C., Zhao, G., Jia, Y., et al. 2019, ApJ, 871, 208
Lindegren, L., Hernández, J., Bombrun, A., et al. 2018, A&A, 616, A2
López-Corredoira, M., Abedi, H., Garzón, F., & Figueras, F. 2014, A&A, 572, A101
López-Corredoira, M., Betancort-Rijo, J., & Beckman, J. E. 2002a, A&A, 386, 169
López-Corredoira, M., Cabrera-Lavers, A., Garzón, F., & Hammersley, P. L. 2002b, A&A, 394, 883
López-Corredoira, M., Garzón, F., Wang, H. F., et al. 2020, A&A, 634, A66
López-Corredoira, M., & Sylos-Labini, F. 2019, A&A, 621, A48
Lacy, L. B. 1974, AJ, 79, 745
Majewski, S. R., Schiavon, R. P., Frinchaboy, P. M., et al. 2017, AJ, 154, 94
Momany, Y., Zaggia, S., Gilmore, G., et al. 2006, A&A, 451, 515
Oort, J. H., Kerr, F. J., & Westerhout, G. 1958, MNRAS, 118, 379
Poggio, E., Drimmel, R., Andrae, R., et al. 2020, NatAs, 4, 590
Poggio, E., Drimmel, R., Lattanzi, M. G., et al. 2018, MNRAS, 481, L21
Queiroz, A. B. A., Anders, F., Chiappini, C., et al. 2020, A&A, 638, A76
Queiroz, A. B. A., Anders, F., Santiago, B. X., et al. 2018, MNRAS, 476, 2556
Reshetnikov, V., & Combes, F. 1998, A&A, 337, 9
Reylé, C., Marshall, D. J., Robin, A. C., & Schultheis, M. 2009, A&A, 495, 819
Sánchez-Saavedra, M. L., Battaner, E., Guijarro, A., López-Corredoira, M., & Castro-Rodríguez, N. 2003, A&A, 399, 457
Sartoretti, P., Katz, D., Cropper, M., et al. 2018, A&A, 616, A6
Skowron, D. M., Skowron, J., Mróz, P., et al. 2019, Sci, 365, 478
Skrutskie, M. F., Cutri, R. M., Stiening, R., et al. 2006, AJ, 131, 1163
Soubiran, C., Jasniewicz, G., Chemin, L., et al. 2018, A&A, 616, A7
Stassun, K. G., & Torres, G. 2018, ApJ, 862, 61
Wang, H., López-Corredoira, M., Carlin, J. L., & Deng, L. 2018, MNRAS, 477, 2858
Wang, H. F., López-Corredoira, M., Huang, Y., et al. 2020, ApJ, 897, 119
Xu, Y., Liu, C., Tian, H., et al. 2020, ApJ, 905, 6
Yusifov, I. 2004, in The Magnetized Interstellar Medium, ed. B. Uyaniker, W. Reich, & R. Wielebinski (Katlenburg-Lindau: Copernicus), 165
Zinn, J. C., Pinsonneault, M. H., Huber, D., & Stello, D. 2019, ApJ, 878, 136

5

Conclusions and future perspectives

Throughout this thesis, we have shown the importance of studying the outer Galactic disc and have contributed several results to this topic. In this chapter, we summarize our main conclusions and suggest future lines of work.

This thesis as a whole presents an extensive analysis of the outer Galactic disc from various perspectives. We take advantage of the *Gaia* data and study this unknown part of the Galaxy with unprecedented detail. For the first time, we can probe the disc up to galactocentric distances of 20 kpc, thus discovering new exciting properties of the Galaxy in these underexplored areas. We look at the outer Galactic disc from various points of view—we explore the density distribution, as well as kinematics and dynamical effects. Therefore, the thesis brings a comprehensive picture of these external parts of the disc and contributes an important piece to our understanding of the structure and evolution of the Galaxy.

In particular, the main conclusions of this thesis are:

- **Density distribution of the outer disc**

  We have made use of Gaia DR2 data combined with Lucy's method to derive the density distribution of the outer disc out to a galactocentric distance of ∼20 kpc. By analysing the density maps we detect an asymmetric warp with a northern amplitude greater by ∼25% compared to the southern part. The northern warp amplitude reaches only ∼0.5 kpc at a distance of ∼20 kpc, which is notably smaller than previously thought. When we compare this result with the warp amplitude of Cepheids, we

find that our warp amplitude is 2–3 times lower, suggesting that the warp amplitude is greatly dependent on the age of the population. To confirm this, we analysed very luminous stars ($M_G < -2$ mag) separately, which represents a younger population on average. This population has a 20–30% larger warp amplitude than the population as a whole, which is 5–6 Gyr old on average. However, it is still considerably lower than the Cepheid warp, which is a significantly younger population (a hundred Myr old at most). This result suggests that the warp is a long-lived feature induced by a non-gravitational mechanism.

- **Rotation curve of the outer disc**

  Another line of research pursued has been the analysis of rotation curves using the Jeans equation. We find a typical flat rotation curve out to 20 kpc, with little dependence on Galactic height. We fit the curves with models including either a Navarro-Frenk-White dark matter halo or Modified Newtonian dynamics and find that the observed curves are well-fitted by both approaches. As observational evidence suggests that the Galactic disc is asymmetric and not in a state of equilibrium, we also studied the validity of the Jeans equation in the outer disc. We developed N-body simulations of a mock galactic system in a configuration close to equilibrium. We compared the rotational velocity of such systems calculated by the Jeans equation and from the gravitational force. We found that both approaches coincide as long as the radial velocity is up to 10% of the azimuthal one. When the radial velocity exceeds this threshold, the Jeans equation overestimates the rotational velocity so that the mass inferred from rotation curve is also overestimated. In the Milky Way, this threshold occurs at ∼20 kpc, implying that, at higher distances, the Jeans equation may produce biased results.

- **Precession of the Galactic warp**

  In the last chapter, we calculated the warp precession. We based our work on previous calculations, which inferred warp precession from a model using Cepheids and found that a complete rotation of the line of nodes takes about 600 Myr, which is significantly shorter than periods predicted by all other models. We applied our warp model, which was representative of the entire stellar population, and found that a high warp precession rate is not necessary, as the data can be explained by a slow precession with period of a few Gyr, as well as by a non-precessing warp. However, we do not have data with high enough precision to discriminate between a

high and low rate of precession, so we can neither support nor exclude any model of warp formation.

5.1 Future perspectives

A natural continuation of our work would be to repeat our analysis with future *Gaia* data releases. By combining *Gaia*'s improved astrometric measurements with Lucy's method, we could significantly extend the region to be studied. The upcoming Gaia DR3, which is scheduled for next year, might already be precise enough to reach distances of 25 kpc or more. We could then explore the outskirts of the Galactic disc and possibly solve the question of the validity of the Jeans equation in non-equilibrium areas as well as measure the warp precession with higher accuracy.

Apart from repeating our analysis over an expanded region, there are other lines of research that can be combined with this work. One is the study of other phenomena, such as the Galactic flare, in the outer disc. The density distribution that we obtained in Chapter 2 can be used to probe the scale-height and analyse its dependence on both radius and azimuth. Our preliminary results reveal flaring in both disc components, the thick disc flare being strongly pronounced. However, in both cases we detect only a small dependence on azimuth.

Another interesting possibility is to make use of cross-matched catalogues of *Gaia* with other surveys containing information about stellar chemistry and ages, which would enable us to study different stellar populations separately. We have already started exploring the recent Gaia EDR3, where we isolated the population of supergiants, based on their magnitude. Preliminary results confirm that this dataset has almost twice as high a warp amplitude than the average population.

An additional line of research is to study the virial theorem in the Milky Way by calculating the potential from the density distribution obtained in Chapter 3 and exploring how is it influenced by non-equilibrium.

A

Additional results

In this appendix we present additional work that was done during the course of the thesis as a part of wider collaborations.

A.1 Analysis of kinematic features of the flare

In Chapter 3 we used extended the kinematic maps of López-Corredoira & Sylos Labini (2019) to explore the rotational curve. However, these maps revealed a number of interesting features in all the velocity components that could be caused by various mechanisms. Therefore the kinematic signatures of known components and phenomena of the Galactic disc were studied and compared with the observed velocities. An analysis was made using the Galactic bar and bulge, overdensities corresponding to spiral arms, interaction with satellites, warp, and flare.

This work was published in the following article:
López-Corredoira, M., Garzón, F., Wang, H. -F., Sylos Labini, F., Nagy, R., Chrobáková, Ž., Chang, J. & Villarroel, B., 'Gaia-DR2 extended kinematical maps. II. Dynamics in the Galactic disk explaining radial and vertical velocities', *Astronomy and Astrophysics*, **634**, A66.

My contribution to this work was a method analysing the flare effect in the distribution of vertical velocities. The result was published in Section 8.2 of the paper, as follows:

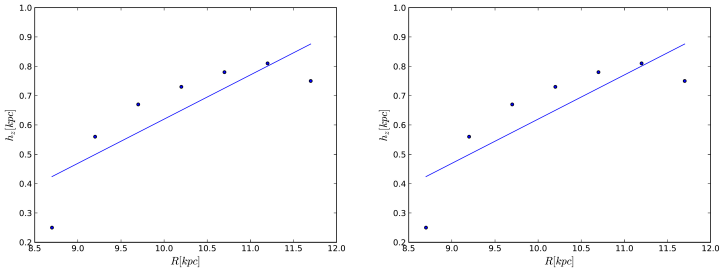

(a) (b)

FIGURE A.1— (a): Fit of h_z as a function of galactocentric radius derived with Eq. (A.1). (b): Same as (a), but after correction with a flare as given in Eq. (A.3). (López-Corredoira et al. 2020).

Fit of h_z with the Moni-Bidin et al. method

We can make a different use of the Jeans equations to find a fit value for the scaleheight h_z. We adopted the approach from Moni Bidin et al. (2012), who use two components of the Jeans equations to express surface density from the Poisson equation in cylindrical coordinates. After making a few assumptions, they obtained the following expression for the surface density:

$$\Sigma(z) = \int_{-z}^{z} \rho \mathrm{d}z = \frac{1}{2\pi G}\left[k_1 \cdot \int_0^Z \sigma^2_{v_R}\mathrm{d}z + k_2 \cdot \int_0^Z \sigma^2_{v_\phi}\mathrm{d}z \cdot + k_3 \cdot \overline{v_R v_z} + \frac{\sigma^2_{v_z}}{h_z} - \frac{\partial \sigma^2_{v_z}}{\partial z}\right], \quad \text{(A.1)}$$

where k_1, k_2, and k_3 are constants defined as

$$\begin{aligned} k_1 &= \frac{3}{R_\odot \cdot h_R} - \frac{2}{h_R^2}, \\ k_2 &= -\frac{1}{R_\odot \cdot h_R}, \text{ and} \\ k_3 &= \frac{3}{h_R} - \frac{2}{R_\odot}. \end{aligned} \tag{A.2}$$

We calculated $\Sigma(z)$ for every R, choosing an initial value of $h_z = 0.3$ kpc. We then proceeded to find the best value of h_z for each R, using an iterative method as follows. We did a least squares fit of the theoretical expression $\Sigma = 2\rho(R, z = 0) \cdot h_z(R) \cdot [1 - e^{-z/h_z(R)}]$ with every value of h_z from the interval $h_z \in [0, 2]$ in steps of $\Delta h_z = 0.01$. For each value of R, we chose a new value of h_z, which corresponds to the smallest χ^2. We used this new value of h_z to calculate Σ again and we then performed a new fit with the theoretical expression for Σ, which again yielded new values of h_z with minimal χ^2. We repeated this procedure until h_z converged. We divided R into bins of size 0.5 kpc and found the best value of h_z for each bin, which gave the dependence $h_z(R)$ that we show in the Figure A.1 (a). We fitted $h_z(R)$ with the linear function, which gave values $h_z(R) = [(0.370 \pm 0.093) + (0.151 \pm 0.044)(R(\text{kpc}) - R_\odot)]$ kpc, $R_\odot = 8.34$ kpc. We calculated h_z only up to $R = 12.0$ kpc since, for higher values, the fit was imprecise and gave untrustworthy results. We did not use a weighted fit, as the error of $\Sigma(z)$ is very large, which leads to an incorrect fit.

In deriving Eq. (A.1), it was assumed that $\partial h_z/\partial R = 0$. But, since we are interested in the effect of the flare, we needed to include terms that had not been included so far. This includes the dependence of $h_z(R)$ on the Jeans equations, and we recalculated the expression for Σ. Equation (A.1) then changed as follows:

$$\begin{aligned} \Sigma(z) = \frac{1}{2\pi G} \Bigg[& k_1 \cdot \int_0^Z \sigma_{v_R}^2 \mathrm{d}z + k_2 \cdot \int_0^Z \sigma_{v_\phi}^2 \mathrm{d}z + k_3 \cdot \overline{v_R v_z} \\ & + \frac{\sigma_{v_z}^2}{h_z} - \frac{\partial \sigma_{v_z}^2}{\partial z} + |z| \overline{v_R v_z} \frac{\partial}{\partial R} \left(\frac{1}{h_z} \right) \\ & + \int_0^Z |z| \frac{\sigma_R^2}{R} \frac{\partial}{\partial R} \left(\frac{1}{h_z} \right) + \int_0^Z |z| \sigma_R^2 \frac{\partial^2}{\partial R^2} \left(\frac{1}{h_z} \right) \Bigg]. \end{aligned} \tag{A.3}$$

We repeated the iterative method for new values of Σ and found a new dependence of $h_z(R)$. To determine the derivatives of $1/h_z$ in Eq. (A.3), we

used the first result for h_z, $h_z(R) = [0.370 + 0.151(R(\mathrm{kpc}) - R_\odot)]$ kpc, derived it, and plugged it into Equation (A.3). The resulting relation for $h_z(R)$ is plotted in Figure A.1 (b). We fitted the new expression for $h_z(R)$ with the linear function $h_z(R) = [(0.533 \pm 0.049) + (0.103 \pm 0.023)(R(\mathrm{kpc}) - R_\odot)]$ kpc.

We saw that the effect of the flare caused an increase in h_z at the solar radius and decreased the slope of the fit of $h_z(R)$. Moreover, it was clear that the scaleheight increased with distance, which is in agreement with results of other authors (Momany et al. 2006; Reylé et al. 2009; López-Corredoira & Molgó 2014; Wang et al. 2018a,b). The effect of the flare is most dominant at high galactocentric distances ($R > 15$ kpc), where our method unfortunately gives imprecise results, so we could not compare these findings. We must bear in mind, however, that this kinematic method gives us information about the mass density (including dark matter) in all components, and not just the stellar density in the disc.

A.2 Analysis of warp kinematics

In Chapter 2, we analysed the warp parameters based on the density distribution. However, the warp also has a kinematic signature that should be explored if we want to understand warp formation.

Wang et al. (2020) studied the distribution of vertical velocities to reveal the warp's presence with a kinematic method. For this purpose, we used the red clump, a well known population of red giants commonly used as standard candles, chosen from LAMOST DR4. The data were cross-matched with Gaia DR2, to obtain astrometric parameters. The advantage of this sample was that we had information about the age for each star, so we could effectively separate stars of different ages and study their warps individually. However, using LAMOST data, we could only reach galactocentric distances of $\sim$13 kpc, therefore we were not exploring the full range of warp.

Wang et al. (2020) fitted the vertical velocities of stars of different age with a simple warp model, including the variation of warp amplitude with time. We observed that the time derivative of warp amplitude had an increasing trend with age, suggesting that the warp always exists, but is not stationary. The line of nodes, however, is almost static, showing only a very small variation (in agreement with results of Chapter 4). The most interesting discovery was that the warp amplitude depended strongly on the age of the stars, the younger stars having a significantly higher warp amplitude. We therefore confirmed the conclusions of Chapter 2 with the kinematic method. These results favour the scenario that the warp is a long-lived, non-steady feature, induced by non-gravitational interaction.

This work was published in the following article:
Wang, H. -F., López-Corredoira, M., Huang, Y., Chang, J., Zhang, H. -W., Carlin, J. L., Chen, X. -D., Chrobáková, Ž. & Chen, B. -Q., 'Mapping the Galactic Disk with the LAMOST and Gaia Red Clump Sample. VI. Evidence for the Long-lived Nonsteady Warp of Nongravitational Scenarios', *The Astrophysical Journal*, **897**, 119.

My contribution to this work was participation in the discussion and interpretation of the results with the the other members of the Chinese and Spanish teams.

Bibliography

López-Corredoira, M., Garzón, F., Wang, H. F., et al. 2020, A&A, 634, A66

López-Corredoira, M. & Molgó, J. 2014, A&A, 567, A106

López-Corredoira, M. & Sylos Labini, F. 2019, A&A, 621, A48

Momany, Y., Zaggia, S., Gilmore, G., et al. 2006, A&A, 451, 515

Moni Bidin, C., Carraro, G., Méndez, R. A., & Smith, R. 2012, ApJ, 751, 30

Reylé, C., Marshall, D. J., Robin, A. C., & Schultheis, M. 2009, A&A, 495, 819

Wang, H. F., Liu, C., Xu, Y., Wan, J.-C., & Deng, L. 2018a, MNRAS, 478, 3367

Wang, H. F., Liu, C., & Deng, L. 2018b, in Rediscovering Our Galaxy, ed. C. Chiappini, I. Minchev, E. Starkenburg, & M. Valentini, Vol. 334, 378–380

Wang, H. F., López-Corredoira, M., Huang, Y., et al. 2020, ApJ, 897, 119

B

Publications

Papers published during the course of this thesis.

1. *Structure of the outer Galactic disc with Gaia DR2*
   Chrobáková, Ž., Nagy, R., and López-Corredoira, M.
   Astronomy & Astrophysics, May 2020, 637, A96.
   2020A&A...637A..96C

2. *Gaia-DR2 extended kinematical maps. III. Rotation curves analysis, dark matter, and MOND tests*
   Chrobáková, Ž., López-Corredoira, M., Sylos Labini, F., Wang, H. F., and Nagy, R.
   Astronomy & Astrophysics, October 2020, 642, A95.
   2020A&A...642A..95C

3. *A Case against a Significant Detection of Precession in the Galactic Warp*
   Chrobáková, Ž., and López-Corredoira, M.
   The Astrophysical Journal, May 2021, 912, 130.
   2021ApJ...912..130C

4. *Gaia-DR2 extended kinematical maps. II. Dynamics in the Galactic disk explaining radial and vertical velocities*
   López-Corredoira, M., Garzón, F., Wang, H. -F., Sylos Labini, F., Nagy, R., **Chrobáková, Ž.**, Chang, J., and Villarroel, B.
   Astronomy & Astrophysics, February 2020, 634, A66.
   2020A&A...634A..66L

5. *Mapping the Galactic Disk with the LAMOST and Gaia Red Clump Sample. VI. Evidence for the Long-lived Nonsteady Warp of Nongravitational Scenarios*
Wang, H. -F., López-Corredoira, M., Huang, Y., Chang, J., Zhang, H. -W., Carlin, J. L., Chen, X. -D., **Chrobáková, Ž.**, and Chen, B. -Q.
The Astrophysical Journal, July 2020, 897, 119.
2020ApJ...897..119W